Development and Use of Optical Sensors in Modern Analytical Chemistry

Aron Hakonen

UNIVERSITY OF GOTHENBURG

Thesis for the degree of doctor of philosophy in Chemistry, Analytical Chemistry

The thesis will be presented in English

Friday, April 23 at 14:00 in KA, Kemigården 4, Göteborg

Faculty opponent is Professor Colette McDonagh

Dublin City University, Ireland

Department of Chemistry

University of Gothenburg

2010

Abstract

A successful long-term high resolution imaging experiment in marine sediments was performed (17 days within the sample; Paper I). The time correlated calibration procedure was evolved to include parametric sigmoidal and logarithmic functions to provide three of the best performing (optical) pH sensors available up to date (Papers II, III and IV), precision of these sensors were in the 0.0029 – 0.0057 pH units range. New pH sensors have been developed using three different immobilization techniques (Papers II, III and IV). The first experiments using a pH optode to image cellular responses were demonstrated (Paper III). A long (over 3 pH units) linear dynamic range (for an optode) with high performance was shown (Paper IV). Possibly a simple linear normalization method for salinity within the sample matrix was realized (Paper IV). Photoacidity and its change due to immobilization was recognized and utilized as an important feature for optical pH measurements (Paper II). A plasmon enhancement/quenching based fluorescent technique using functionalized gold nanoparticles was developed and implemented on a co-extraction based ammonium sensor (Paper V). This technique demonstrated a limit of detection three orders of magnitude better than previous ammonium sensors (LOD = 1.7 nM vs. ~ 1 μM), and can directly be implemented on more than 25 other cationic species.

KEYWORDS: Optical sensors, Optodes, Imaging sensors, Fluorescence, pH, Ammonium, Sensing, Nanoparticle enhancement, Plasmonics

Printed by Chalmers Reproservice, Göteborg

ISBN: 978-91-628-8095-8

Populärvetenskaplig sammanfattning på svenska

I dagens samhälle med klimatförändringar, försurning av oceanerna, övergödning av såväl mark som vatten samt okontrollerade utsläpp av diverse kemikalier, har vi ökade behov av både regler som begränsar utsläpp och användning, samt av mätmetoder som på ett korrekt sätt kan kontrollera att reglerna efterföljs. Lämpligen skall man använda sensorer som kan mäta på plats direkt i naturen, stadsmiljön eller vid fabriken för att få så riktiga och aktuella mätvärden som möjligt.

Optiska sensorer (optoder) är ett mätverktyg som kan mäta koncentrationer av kemikalier samt diverse fysikaliska parametrar som tryck och temperatur. De består i princip av en sensorfilm som belyses med ljus och beroende på den aktuella mätparametern så ändras ljuset som kommer från filmen vilket mäts med en detektor. Fördelar med optoder inkluderar att det är en in-situ (på plats) mätmetod samt att man mäter på provet utan att förstöra det.

Den snabba utvecklingen av digitalkameror har medfört att optiska sensorer med hög precision kan mäta avbildande med upp till miljontals mätpunkter i varje bild. Den avbildande egenskapen hos optoden medför stora fördelar jämfört med traditionella mätmetoder, t.ex. elektroder, om man vill titta på ett prov över tiden med fler än enstaka mätpunker

Trots många fördelar med optoderna så är det en relativt ny teknik (utvecklingen tog fart i mitten på 80-talet), och den lider alltjämt av ”barnsjukdomar”. Exempelvis är optoder vanligtvis associerade med drift och långtidsinstabilitet, till stor del beroende på blekning av sensorfilmen eller läckage av de ämnen i filmen som är känsliga för mätparametern och används vid analysen.

I denna avhandlig har nya kalibrertekniker och högpresterande sensorer utvecklats och analytiskt verifierats. Exempel på utveckling inkluderar högpresterande optoder för pH och ammonium. Genom att inkorporera guldnanopartiklar i en tidigare utvecklad ammoniumsensor förbättrades känsligheten 1000 gånger, varvid det var möjligt att detektera koncentrationer på 30 nanogram (miljarddels gram) per liter.

Table of Contents

Publications

Research papers included in this thesis (referred to by roman numerals).

I.

Hakonen, A. ;Hulth, S.; Dufour, S., Analytical performance during ratiometric long-term imaging of pH in bioturbated sediments.

Talanta **2010**, *DOI information: 10.1016/j.talanta.2010.02.041*

II.

Hakonen, A.; Hulth, S., A high-precision ratiometric fluorosensor for pH: Implementing time-dependent non-linear calibration protocols for drift compensation.

Analytica Chimica Acta **2008,** 606, (1), 63-71.

III.

Stromberg , N.; Mattson, E.; Hakonen, A., An imaging pH-optode for cell studies based on covalent attachment of 8-hydroxypyrene-1,3,6-trisulfonate to amino cellulose acetate films.

Analytica Chimica Acta **2009**, 636, (1), 89-94.

IV.

Hakonen, A.; Hulth, S., A high-performance fluorosensor for pH measurements between 6 and 9.

Talanta **2010**, 80, (5), 1964-1969.

V.

Hakonen, A., Plasmon enhancement and surface wave quenching for phase ratiometry in coextraction based fluorosensors.

Analytical Chemistry **2009**, 81, (11), 4555-4559.

List of abbreviations

CCD	Charge Coupled Device
DHPDS	6,8-Dihyroxypyrene-1,3-Disulphonate
Em	Emission wavelength (often followed by the wavelength)
Ex	Excitation wavelength (often followed by the wavelength)
GNP(s)	Gold nanoparticle(s)
HPTS	8-Hydroxypyrene-1,3,6-trisulphonate
LED	Light Emitting Diode
LOD	Limit of Detection
LSW(s)	Lossy Surface Wave(s)
MEF	Metal Enhanced Fluorescence
MIP(s)	Molecularly Imprinted Polymer(s)
NP(s)	Nanoparticle(s)
PMT	Photo Multiplier Tube
P.S.D.	Pooled Standard Deviation
S.D.	Standard Deviation
SP(s)	Surface Plasmon(s)
λ	Wavelength of light

1. Introduction

In today's society with frequent reports of climat change, ocean acidification, euthrophication and uncontrolled use and release of various hazardous chemicals, there is an increased demand of regulations as well as accurate and reliable measurement techniques for the enforcement of these rules. Preferably these measurements could be performed directly in the nature, the city environment or at the factory to provide as correct and up to date values as possible. Therefore, there is especially an increasing demand for in-situ methods to provide accurate monitoring of important parameters such as pH (paper I-IV) and macronutrients (e.g. ammonium and nitrate; paper V). Consequences and feedbacks from changes in these parameters may have local, regional or global importance. For example, seawater pH has received particular attention in current characterizations of the oceanic response to anthropogenic emissions of CO_2, in part due to the recently demonstrated acidification of the world´s oceans [1]. Further, molecular imaging on macro- (Paper I) as well as on the microscopic level (paper III) has gained significant interest recently, and has been used within research fields such as clinical diagnostics and cancer research [2-6]. Other current topics within modern analytical chemistry involves nanoparticles and plasmonics for signal enhancement and ultra sensitive measurements (Paper V) [3, 7-14].

The main objectives of this work were to develop high-performance optical sensors and analytical protocols for robust long-term measurements, and to do careful assessment of these to ensure analytical performance.

2. Background

2.1. Luminescence

Luminescence is the emission of light from any substance and occurs from electronically excited states. Luminescence is divided into two formal subgroups Fluorescence and Phosphorescence [15].

In fluorescence, a fluorescent molecule absorbs light according to principles decribed by the Lambert-Beers Law. The excited electron remains spin-paired (opposite direction of spins) with the ground state electron in S_0 throughout the relaxation process (Fig. 2.1.1). Energy relaxation proceeds within the system (S_1, S_2 …., S_n) to the lowest vibrational level of S_1 where the electron either relaxes non-radiatively (rate constant: k_{nr}) by energy transfer to surrounding molecules or by emitting a photon (Fluorescence with radiative rate constant: k_r). Two important relationships can be derived from these rate constants.

The quantum yield (photons emitted / photons absorbed):

$$\Phi = \frac{k_r}{k_r + k_{nr}} \qquad \textit{(Eq. 2.1)}$$

Fluorescence lifetime (time from excitation to emission; typically within nanosecond regime):

$$\tau = \frac{1}{k_r + k_{nr}} \qquad \textit{(Eq. 2.2)}$$

If there are additional pathways for energy transfer, such as in the case of plasmonic intermetal enhanced fluorescence (paper V), these need to be accounted for in eq. 2.1 and 2.2.

In phosphorescence absorption of energy occurs as described for fluorescence, however, the excited electron converts into a triplet state (T_1 ; Fig. 2.1.1) which has a parallel spin with the ground state electron. Transitions to and from triplet states are spin-forbidden, due to the unmatched spins, and are

highly unlikely. Hence, phosphorescence has a considerably lower quantum yield and longer life-time compared to fluorescence. The phosphorescence life-times can be up to several minutes (e.g. in glow-in-the-dark toys) but are typically milliseconds to seconds.

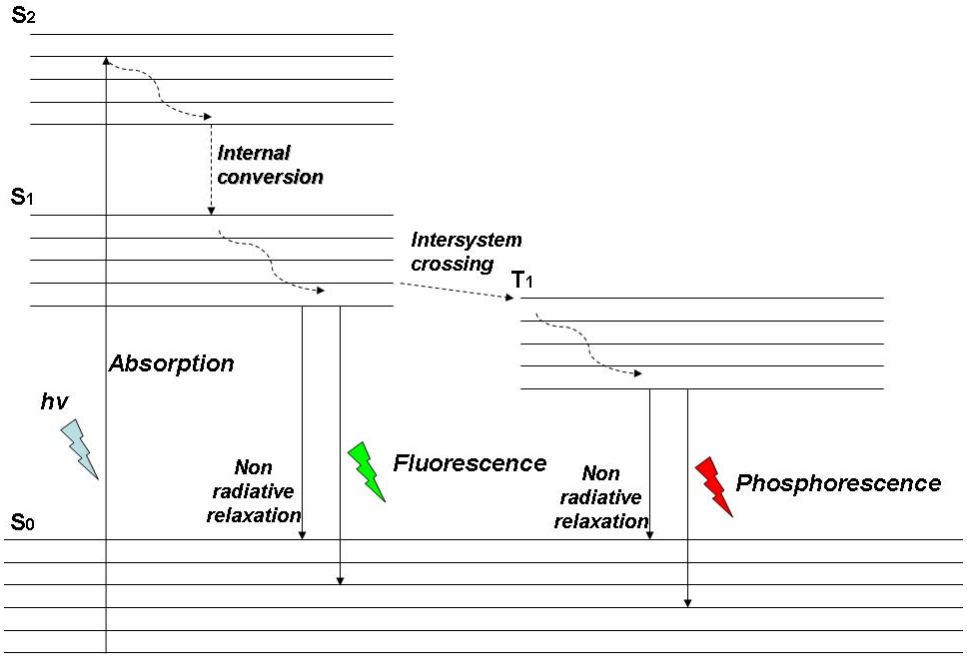

Figure 2.1.1. Principles of fluorescence and phosphorescence illustrated in a Jabłoński diagram. The energy shift between absorption and fluorescence/phosphorescence is often referred to as the Stokes' shift.

Under high intensity illumination conditions, the irreversible destruction or photobleaching of the excited fluorophore becomes a limiting factor for detection and quantification. Some pathways include reactions between adjacent dye molecules making the process highly complex in optical sensing membranes. Photobleaching normally originates from the generation of the triplet excited state without light emitting relaxation (T_1; Fig. 2.1.1) [16].

2.2. Lifetime measurements

Time-resolved measurements are widely used in fluorescence spectroscopy. Lifetime-based sensing schemes often demonstrate a significantly reduced susceptibility for intensity and wavelength dependent

interferences [17, 18]. Another important feature of lifetime measurements is that the signal often contains more information than intensity measurements. For example, information about protein conformation and interactions can be obtained [15].

An excitation pulse of light yields in an initial population of excited fluorophores (n_0), which decays with the rate k_r+k_{nr} according to:

$$\frac{dn(t)}{dt} = -(k_r + k_{nr})n(t) \qquad \textit{(Eq. 2.3)}$$

where $n(t)$ is the number of excited molecules at time t. Each excited fluorophore has the same probability of emitting in a given period of time. Hence there is an exponential decay of the excited state population:

$$n(t) = n_0 \exp(-t/\tau) \qquad \textit{(Eq. 2.4)}$$

The fluorescence intensity at time t can be derived by integrating Eq. 2.3:

$$I(t) = I_0 \exp(-t/\tau) \qquad \textit{(Eq. 2.5)}$$

where I_0 is the fluorescence intensity at time zero. This is the usual expression for a single exponential decay. Commonly, time domain fluorescence lifetime is determined from the slope of a plot of log$I(t)$ versus t. Lifetime can also be determined within the frequency domain (phase modulation), by using a pulsed excitation light source and a modulated detector. The phase angle (φ) and the modulation (m) can be used to calculate the phase and modulation lifetime from the following relations [15]:

$$\tau_\varphi = \omega^{-1} \tan\varphi \qquad \textit{(Eq. 2.6)}$$

$$\tau_m = \omega^{-1}\left[\frac{1}{m^2} - 1\right]^{1/2} \qquad \textit{(Eq. 2.7)}$$

2.3. Fluorescence quenching

Fluorescence intensity can be decreased by a number of mechanisms that are termed quenching processes. Collisional quenching occurs when the excited-state molecule is deactivated upon contact with another molecule (the quencher). For collisional quenching, the decline in fluorescence intensity is described by the Stern-Volmer equation:

$$\frac{F_0}{F} = 1 + K[Q] = 1 + k_q \tau_0 [Q] \qquad \textit{(Eq. 2.8)}$$

K is the Stern-Volmer quenching constant, k_q is the bimolecular quenching constant *[Q]* is quencher concentration and τ_0 is the unquenched lifetime. Examples of molecules that can act as dynamic quenchers are oxygen, halogens, amines and electron deficient molecules like acrylamide [15]. The mechanism of dynamic quenching can vary. For example quenching by halogens and heavy atoms occurs due to spin-orbit coupling and intersystem crossing to the triplet state (Fig. 2.1.1) [15]. Another process is called static quenching and occurs when the fluorophore forms nonfluorescent complexes with quenchers. Static quenching occurs in ground state and does not rely on diffusion and collisions. Quenching can also occur by nonmolecular processes such as attenuation of the incident light by the fluorophore or other absorbing species, i.e. inner filter effects.

Quenching is a frequently used sensing method, and current optical measurements of oxygen concentration mainly proceed by principles of fluorescence quenching. The first oxygen sensor based on quenching was demonstrated in 1968 [19]. Optical oxygen sensors are usually rely on phosphorescent metal complexes, often ruthenium, and lately lifetime based sensing of oxygen has become the dominating detection method [20-23]. In paper V (also described in section 3.5), a combined plasmon-enhanced and quenching-based sensor was presented for quantification of solutes using coextraction.

2.4. Ratiometric measurements

In some cases, for example Ca^{2+} indicators fura-2 and indo-1 and pH indicators 8-Hydroxypyrene-1, 3,6-trisulphonate (HPTS) and 6,8-Dihydroxypyrene-1,3-disulphonate (DHPDS), the free and ion-bound form of the indicator displays different excitation and/or emission properties (e.g. Fig. 2.5.1). With this type of indicators, the ratio of the fluorescence signal can be used to measure the association/dissociation equilibrium and to calculate ion concentrations [24, 25]. Ratiometric normalization schemes provide an alternative technique to time and frequency-domain fluorescence lifetime measurements. The ratiometric normalization procedure is normally assumed to remove artifacts that induce a sensor response not related to changes in analyte concentrations, e.g. variations in ambient and excitation light intensities, uneven dye concentration, photobleaching and wash-out of the indicator dye [25]. The ratiometric approach has even been shown to be as effective as lifetime measurements to reduce artifacts [26].

Reversible ratiometric probes have up to recently been in diminutive supply, but lately ratiometric probes have been developed for several ions e.g. Zn^{2+}, Mg^{2+}, F^-, PO_4^{3-} and molecular oxygen [27-31]. Until the study by Kurihara et al.[32], ratiometric analytical schemes were only applied on solute specific probes with intrinsic ratiometric properties. However, implementing ionophores as analyte carriers in conjunction with solvent (or polarity) sensitive fluorescent dyes that exhibit a spectral shift upon change of environment, have realized ratiometric sensing schemes for a progressively increasing number of solutes. Examples for which ionophores and principles of coextraction have been utilized for ratiometric solute detection include Na^+ and NH_4^+ [32, 33].

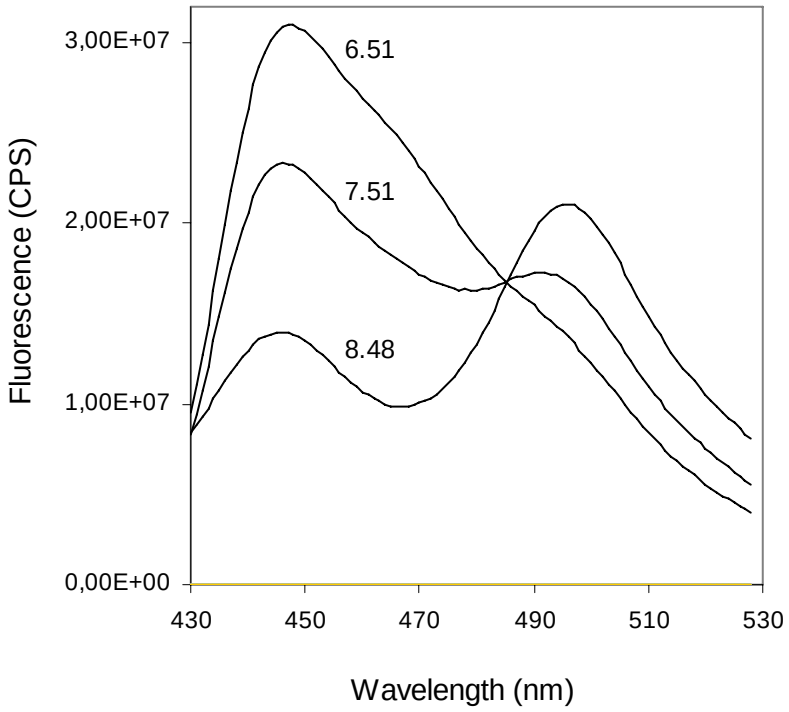

Fig. 2.4.1. Emission spectra, with excitation at 420 nm, of DHPDS at different pH values, demonstrating ratiometric properties. The ratio of the emissions at 450 and 500 nm can be used to normalize for artifacts.

2.5. Analyte specific fluorescent dyes

Truly solute specific dyes, that directly and reversible interacts with the analyte are not as common as might be expected. A selection of solutes that has commercially available specific dyes (reversible) is listed in table 2.5.1.

Table 2.5.1. A number of solutes with commercially available specific dyes.

Cations	Anions	Molecules
H^+, Ca^{2+}, Na^+, Mg^{2+}, K^+, Zn^{2+}, Hg^{2+}	Cl^-	O_2

An ion that has attracted much attention the past few decades is Ca^{2+}. Several fluorescent indicators have been developed, mainly for intracellular calcium. Two examples are the ratiometric dyes indo-1 and fura-2 [34, 35]. Most Ca^{2+} dyes are based on fluorescent chelators that alter fluorescence characteristics upon complexing with the calcium ion. The majority of dyes for other cationic metals are based on the same principle, and many are just modifications of Ca^{2+} indicators. Typically these chelating indicators have affinity toward several ions, thus interferences are always an important issue to be considered [16].

The probably most common type of solute specific fluorophore is the pH sensitive dye. This is not surprising since basically all conjugated molecules with proton accepting or donating groups are highly selective and reversible pH indicators. Obvious concerns during optical pH measurements are to match the pK_a of the fluorophore with the sample pH. Structurally, pH sensitivity is a consequence to reconfiguration of the fluorophores π-electron system upon protonation. Examples of fluorophores for pH measurements include HPTS (paper I-III) [24, 36, 37], and DHPDS (paper IV) [38, 39]. General patterns of HPTS fluorescence are governed by the protonation/deprotonation equilibrium of the hydroxyl hydrogen [40]. HPTS is usually considered highly photo-acidic, i.e. the fluorophore is more acidic in the electronically excited state than in the ground state [41]. The pK_a of excited photo-acidic compounds is usually 6-7 pH units lower than in the ground state. For example, pK_a of HPTS in low ionic strength solution is ~ 7.3 while in excited state it can be 1.0 [15]. Photo-acidic properties therefore induce the dual excitation (~ 405 and 450 nm) single emission (~520 nm) ratiometric sensing scheme observed for HPTS in solution. However, a severely reduced photo-acidity of the immobilized fluorophore can be utilized in the sensing scheme to gain sensitivity (paper II). In contrast to the wide range of pH studies that include HPTS, there are only few studies that have utilized the di-hydroxylated analogue DHPDS [38, 39, 42]. DHPDS shares most of the advantageous properties of HPTS, such as high quantum yield, excellent water solubility, ratiometric properties and lack of toxicity. As the structure of DHPDS includes two hydroxyl groups with overlapping (within 2 pH units) pK_a-values

(7.33 and 8.53; [36]), we hypothesized that the two acidic protons provide the basis for a significantly improved sensor dynamic range compared to, for example, HPTS-based sensors. In paper V DHPDS was used and a linear correlation (R^2=0.9936) between log($R_{F1/F2}$) and pH was demonstrated within the pH interval 6 to 9. We also showed in solution that the linearity can be extended up to five pH units.

3. Optical sensors (optodes)

3.1. Overview

Typically, optodes are made from a translucent thin polymer film or a sol-gel in which a solute sensitive fluorescent dye is immobilized, e.g. [14, 40, 43-47]. An example of an optode set-up is shown in Fig. 3.1.1. After equilibration with the sample matrix, the indicator film is illuminated and the light emitted from the sensor is collected with a photomultiplier tube (PMT), photodiode or a CCD chip. Optodes are normally not sensitive to electrical interferences and are comparably easy to miniaturize for e.g. in vivo measurements [48-50]. Further, optodes are also suitable for high-resolution imaging of solute distributions in complex environments such as aquatic sediments [20, 44, 51-55], and there are possibilities for multi-parameter and multi-analyte sensing [56-58]. Drawbacks of most optical sensors include an inherent sensitivity to changes in ionic strength of the sample matrix [59]. They are also influenced by variations in excitation light intensity, and often have a limited long-term stability due to leaching and photobleaching of the indicator dye [15, 25, 35, 60]. In fact, optical sensors are commonly susceptible to a drift in sensor response, a phenomenon only rarely fully compensated for by appropriate analytical protocols [60-62].

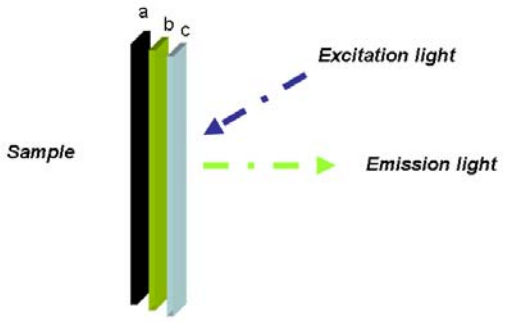

Fig. 3.1.1 A schematic of an optode set-up with the sample within an aquaria and the optics on the outside. Separating sample and optics are: a) Black optical isolation and mechanical protection. b) Polymeric film with immobilized indicator dye. c) Aquarium wall.

3.2. Immobilization techniques

In most reagent-based optical sensors (as those in this thesis), the reagent (e.g. a solute specific dye) is immobilized in a solid matrix usually in the form of a monolith or a thin film. The matrix serves to encapsulate the reagent such that it is accessible to the analyte while being impervious to leaching effects [14]. Immobilization can either involve chemical interactions or actual physical entrapment of the signal transducer.

The sol-gel process provides a commonly used support matrix for the immobilization of analyte-sensitive reagents and dyes [47, 63-66]. This process involves the hydrolysis and polycondensation of the appropriate metal alkoxide solution to produce a porous glass matrix in which the indicator is encapsulated in a nanometer-scale cage-like structure and into which the analyte can diffuse [14]. The versatility of the process facilitates tailoring of the physicochemical properties of the material in order to optimize sensor performance, key sol-gel process parameters such as sol pH, precursor type and

concentration, water content, and curing temperature can be adjusted to produce materials of desired porosity and polarity [65].

In polymeric films the flourophore can be immobilized by both physical entrapment and different chemical interactions. The chemical interactions (used in all papers in this thesis) that can be utilized are basically in a falling order of chemical stability: covalent bond, ionic interaction, hydrophobic interaction, hydrogen bond and weaker interactions such as dispersion forces. Also combinations of forces are present.

The sensing film (cellulose acetate on polyester) used in paper I and IV was immersed over night in a high ionic strength (NaCl 1.0 M) solution with the fluorophore (HPTS in paper I and DHPDS in paper IV). The high ionic strength is intended to provide thin double layers, which allows short range fluorophore-foil interactions. These close interactions are the basis for the immobilization, by e.g. hydrogen bonds, ion-dipole, Van der Waals forces and hydrophobic interactions. The cellulose acetate provides a convenient platform for DHPDS association by these interactions as the ζ -potential is close to zero for ionic strengths above 3 mM [67].

Ionic immobilization has been an often used principle to attach the dye molecule within the sensing foil, e.g. [24, 40, 47, 68]. In paper II this immobilization approach was utilized. HPTS was Ion-paired with hydrophobic cation Tetraoctylammonium and embedded within an ethylcellulose polymer matrix.

Covalent attachment of the dye to the sensing film is often assumed to be a superior immobilization technique. The sensor in paper III is based on the covalent attachment of HPTS to a film forming cellulose acetate material through a sulfonamide linkage. Indeed the covalent attachment provided the best performing optode (a precision defined as IUPAC Pooled S.D. of 0.0029 pH units) and it performed very well even without the time-dependent calibrations. However, although the ratiometric signal was constant with no visible drift, a significant drift was observed for the individual

wavelengths (worse than could be observed for the other two immobilization techniques). This can be due to a higher phototoxicity of the dye in the more restricted environment in the covalent form. Other drawbacks of the covalent method are: time consuming, complex synthesis is required and long-term continuous use is likely restricted due to the heavy photobleaching.

In summary it seems as covalent attachment of the dye is warranted for short term high performance measurements without time-correlation, while for time-correlated measurements the other two immobilization techniques are sufficient. For long-term measurements the methods used in papers I, II and IV may even be preferred.

3.3. Normalization of sensor response

As mentioned above (section 3.1) optical sensors and also, in principle, all types of sensors are susceptible for signal drift over time. There are, however, several spectroscopic techniques and analytical calibration protocols designed to normalize for signal drift and a sensor response not associated with changes in analyte activity. Such procedures include time and frequency-domain fluorescence lifetime measurements. Lifetime-based sensing schemes often demonstrate a significantly reduced susceptibility for intensity and wavelength dependent interferences [17, 18]. However, fluorescence lifetime measurements are usually associated with complex and costly instrumentation.

Previously piece-wise linear time correlated functions with table look up have been demonstrated by Strömberg and Hulth [61, 62], and was used in paper I. Within this thesis we have evolved the time correlated calibrations to include continuous functions. This provides two explicit improvements: Outliers in the calibration will not have as much impact and the speed of calculations will increase significantly. Additionally, it is more likely that the signal increase or decrease should follow a continuous function.

In paper II a time-dependent non-linear calibration protocol for optical sensors was implemented on HPTS immobilized in ethyl-cellulose. The calibration protocol individually compensated for the progressive drift of calibration parameters, whereby sensor precision and accuracy, as well as applicable lifetime are improved. The calibration made before the samples were linked in time to the calibration that followed the samples, thus supporting a sigmoidal time dependent calibration function:

$$\mathrm{R}_{\mathrm{F1,F2}}(pH,t) = \alpha_1(t) + \frac{\alpha_2(t) - \alpha_1(t)}{1 + 10^{(pH - pK_a(t))\alpha_4(t)}} \qquad \textit{(Eq. 3.1)}$$

Where each of the time dependent variables varies according to:

$$\alpha_i(t) = \alpha_{i,Cal1} + \frac{\alpha_{i,Cal1} - \alpha_{i,Cal2}}{\Delta t_{(Cal1,Cal2)}} \cdot t \qquad \textit{(Eq. 3.2)}$$

As preceding experiments have indicated a linear characteristic of sensor drift (not shown), each of the four parameters was assumed to independently express a linear drift in time between the two calibrations. Each sample pH could thus be individually predicted from a time-dependent response function, ideally normalizing for drift in sensor response:

$$pH\left(R_{F1,F2},t\right) = pK_a(t) + \frac{\log\left(\frac{\alpha_2(t) - \alpha_1(t)}{R_{F1,F2} - \alpha_1(t)} - 1\right)}{\alpha_4(t)} \qquad \textit{(Eq. 3.3)}$$

The time dependent calibration procedure demonstrated a precision (defined as IUPAC pooled standard deviation) of 0.0044 pH units within the interval 6.985 – 7.852, compared to 0.0046 for the electrode used for standardization. Sensor analytical characteristics were thereby in principle limited by the performance of the standardization procedure. The progress of calibration functions and samples are illustrated in figure 3.3.1.

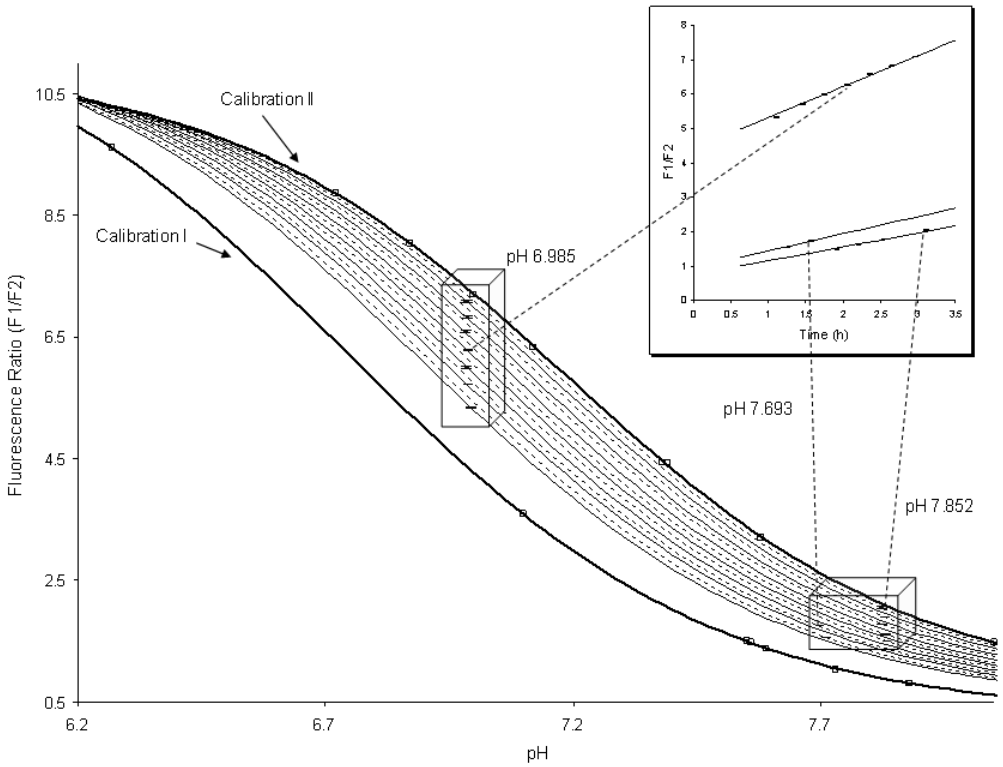

Fig. 3.3.1. An example of the the progressive evolution of sigmoidal calibration curves during experiments (from Paper II). Inset shows linear drift of separate samples.

The time dependent calibration procedure was evolved even further in paper IV to log linear (between $\log(R_{F1/F2})$ and pH) time dependent calibrations providing the benefit of two point calibrations. Also here a linear drift of the calibration parameters was assumed. The precision (P.S.D. of 0.0057 pH units) was slightly inferior to those in paper II and III, however, over a much wider pH range, 3 pH units compared with ~1 pH unit. Repeatability of these measurements is demonstrated in figure 3.3.2.

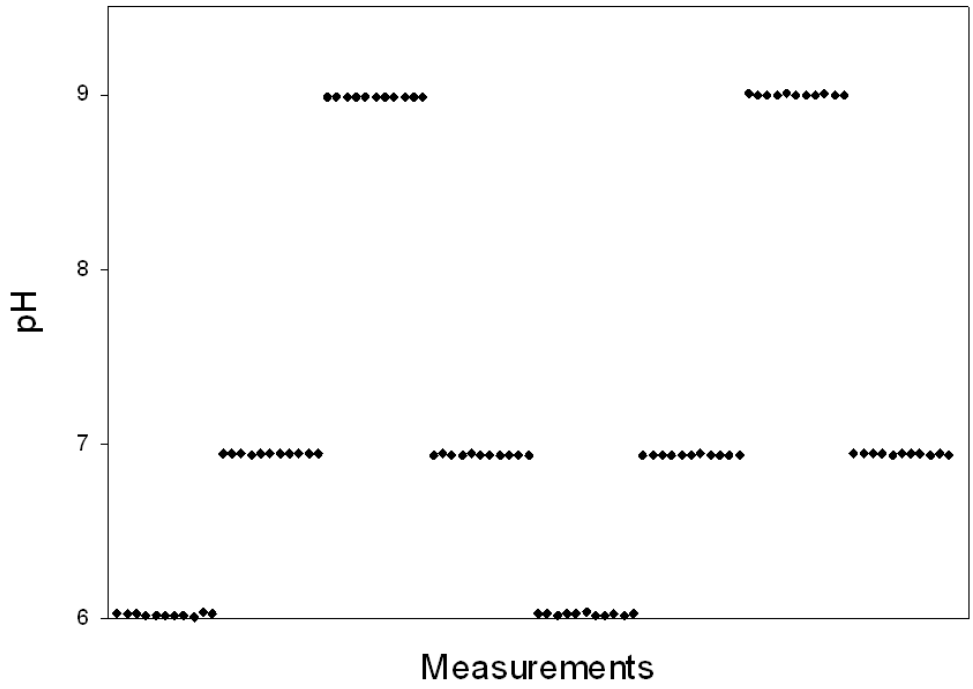

Fig. 3.3.2. Repeatability of pH measurements of the DHPDS based sensor in paper IV. The repeatability was tested on reference buffers of pH: 6.00, 7.01 and 9.01 (NIST).

3.4. Imaging sensors

The rapid progress of digital imaging has made it possible to image with high-resolution and high-precision in a convenient manner (An example of an imaging set-up is shown in Fig. 3.4.1). Hence, optical sensors have been found suitable for high-resolution imaging of gas and solute distributions in complex environments such as soil, aquatic sediments and living cells [18, 28, 43, 44, 51, 55, 69, 70]. One of the earliest examples of imaging with optodes was performed by Glud et al. in 1996, these authors demonstrated oxygen imaging within marine sediments [55].

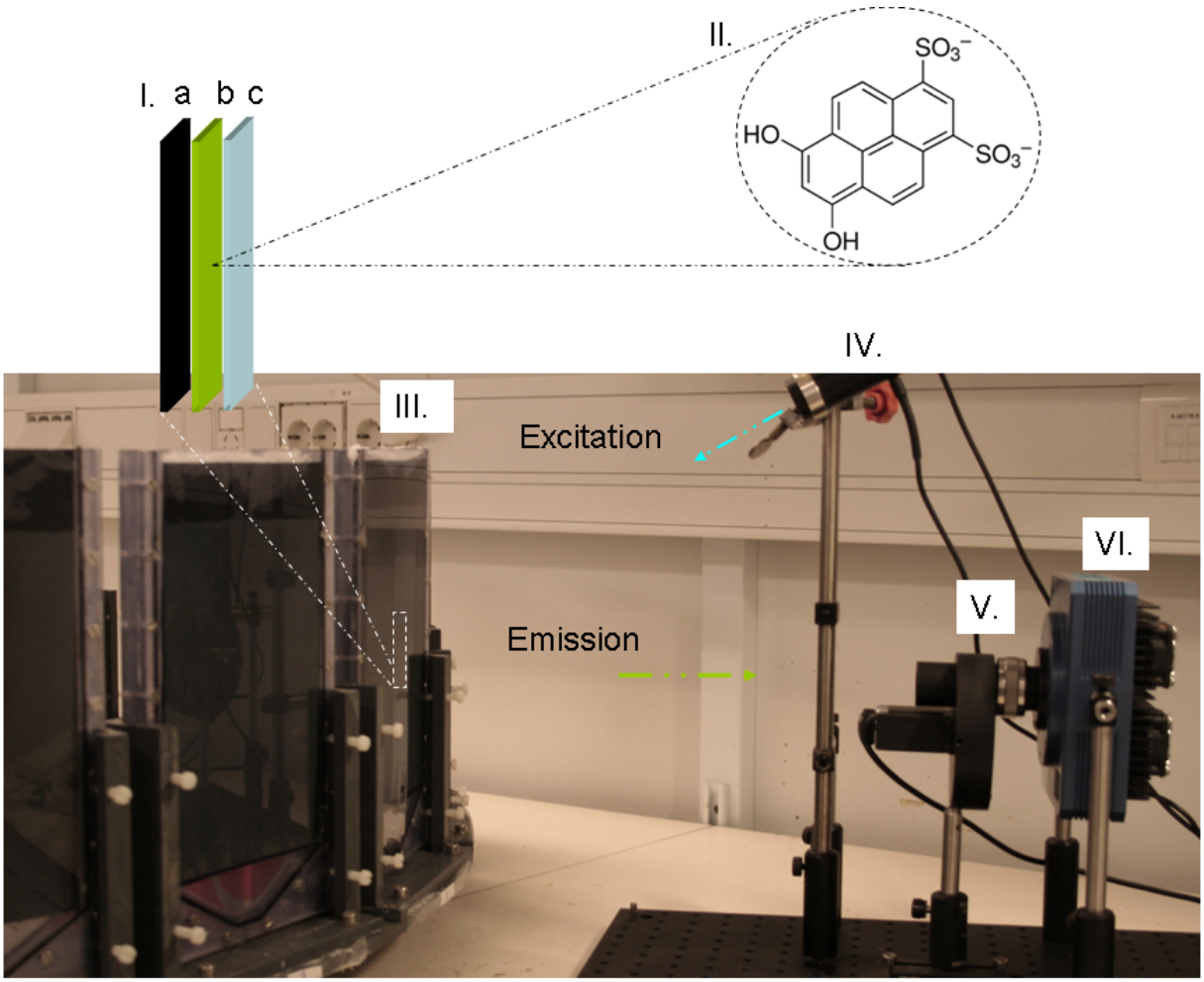

Figure 3.4.1. An example of an optical imaging system. I. Close up of: a) Black optical isolation and mechanical protection. b) Polymeric film with immobilized indicator dye. c) Aquarium wall (here polycarbonate). II. Dye molecule (here the pH sensitive fluorophore 6,8 – Dihydroxypyrene – 1,3 – disulphonate [42]). III. Aquarium for sample matrix (here marine sediment), mounted on a motorized multi-sample wheel. IV. LED excitation light source. V. Optics for emission collection with a filter-wheel for bandpass filters. VI. CCD camera.

The benefit of optode imaging is quite clear as you can get high-resolution 2D images of analyte distributions in a non-destructive way, compared with single point (or few point) measurements that conventional methods such as electrodes provide. Also for a specific time, gradients can be used to show in and out flows to single pixels, revealing patterns unseen in the plain concentration image. Figure 3.4.2 from paper I shows a time series of single pixel gradients.

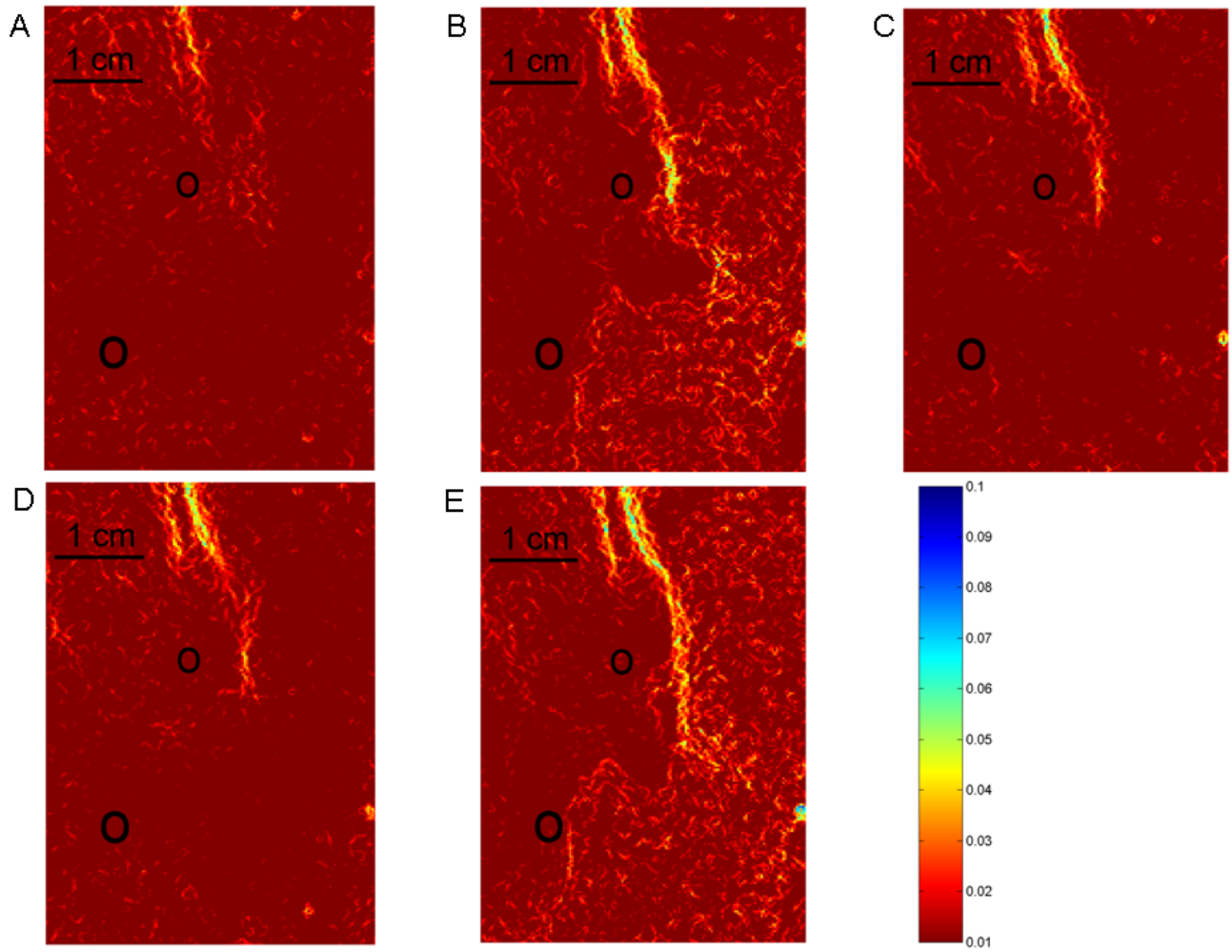

Figure 3.4.2. The figure shows a time series of single pixel gradients. Image B and E are morning images and the rest is from the afternoon. Black rings demonstrate locations of the animals and the scale bar show the pH gradient in pH units per pixel (from paper I).

3.5. Metal enhanced fluorescence (MEF)

Metal enhanced fluorescence (MEF) and plasmonics have reached a great deal of attention lately, and has become a widely explored technique for signal enhancement [71-73]. At least three metal-fluorophore interactions can be utilized for improved analytical sensitivity. Surface plasmons (SPs) are oscillating electronic excitations near the metal surface which can be produced by exposing the surface with electromagnetic radiation close to the metals resonance frequency [71-79]. For planar surfaces, fluorophore to metal distances of ~ 10-100 nm enhances the fluorescence by surface plasmon coupled

emission [79]. Surface plasmons can generally be well described by classical electrodynamics and correspond to Mie's solutions of Maxwell's equations [72, 79]. The SPs can interact in cooperation with the fluorophores excitation- or emission band depending on the location of the plasmon peak and the fluorophores excitation and emission, increasing either the absorption or quantum efficiency of the fluorophore [73]. Faster decay rates and increased photostability is also expected [72, 73, 80]. Fluorescence quenching by lossy surface waves (LSWs) [80] constitutes another important short range interaction for distances closer than ~ 100 nm and becomes dominating below ~ 10 nm [79]. A cubed quenching distance (d^3) dependence by LSWs has been shown [81]. The fundamental physics of LSWs is complex and not fully understood. Commonly this non-radiative energy dissipation is attributed to ohmic losses within the metal as the surface wave propagates [72, 79]. Additional characteristics of fluorophores in close range of colloidal metal surfaces includes amplification of the incident field of radiation by scattering [72, 82].

In paper V gold nanoparticles (GNPs) were lipophilized with dodecanethiol and incorporated in the ether phase of a coextraction based ammonium sensor previously developed by Strömberg and Hulth [43]. This new sensor configuration (Fig. 3.5.1) reduced noise and increased fluorescence signals (intensity as well as ratio). Surface plasmon enhancement, lossy surface wave quenching and likely scattering contributed to the signal improvement. Limit of detection (1.7 nM) was approximately three orders of magnitude better than preceding ammonium sensors.

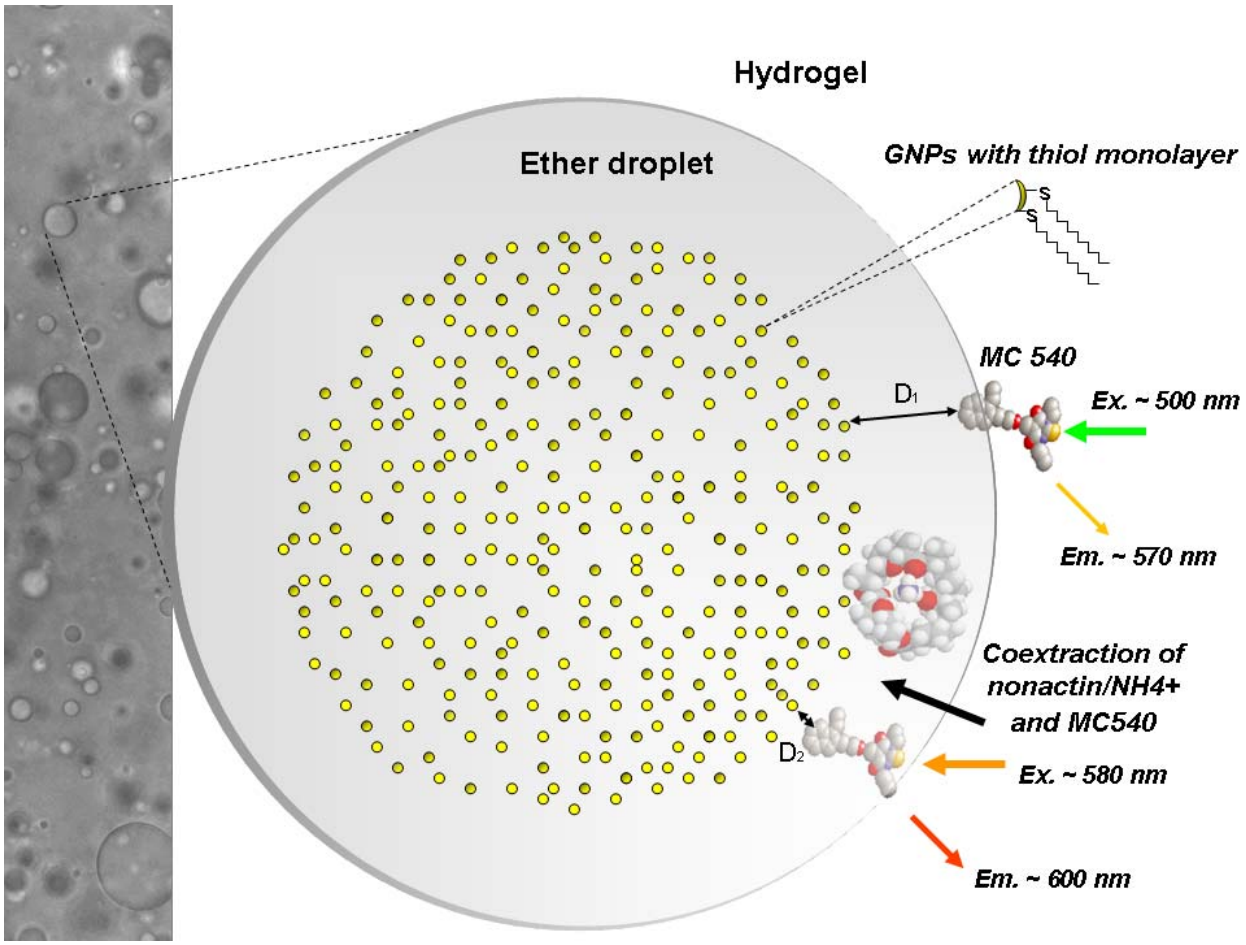

Figure 3.5.1. Proposed sensing scheme for the plasmon enhanced ammonium sensor (paper V). Average D_1 should be close enough to provide mainly plasmonic enhancement for Ex500/Em570 fluorescence, while D_2 should optimally be < 10 nm (where fluorescence quenching becomes dominating for the Ex500/Em570 wavelength pair).

The sensing scheme is general and can be utilized for numerous ions, by shifting the ionophore (for cations) or the co-extraction pair for anions. Some commercially available ionophores are listed in Table 3.5.1, and the number increases rapidly.

Table 3.5.1. Ions that have commercially available ionophores (Sigma Aldrich).

Aluminium	Cerium(III)	Hydrogen sulfite	Nitrate	Silver
Amine	Cesium	Iodide	Nitrite	Sodium
Ammonium	Chromium(III)	Iron(III)	Perchlorate	Thulium
Arsenite	Cobalt(II)	Lead	Phthalate	Tin(II)
Barium	Copper(II)	Lithium	Potassium	Uranyl
Benzoate	Cyanide	Magnesium	Rubidium	Ytterbium(III)
Cadmium	Erbium(III)	Mercury	Salicylate	Zinc
Calcium	Fluoride	Nickel	Samarium(III)	
Carbonate	Hydrogen			

4. Outlook and conclusions

4.1. Continuing projects

The nanoparticle enhanced sensor developed in paper V has successfully been applied for imaging of biological tissues (Hakonen and Strömberg, manuscript). The sensors were tested during 14 days of experiments on a high throughput imaging system recently developed by Strömberg et al. [83]. Some performance data from these experiments can be seen in table 4.1.1. Although applied in a high potassium matrix (5 mM) high-quality limits of detection were revealed (Table 4.1.1; for a binned area 300×300 pixels). The detection limit data also agrees well with previous research [60-62, 84]. However, at pixel level average LOD for the best performing NP sensor (Q) was ~ 400 nM, while the best NP free sensor (P) demonstrated a LOD of ~ 3 μM. The converging detection limits indicates that when approaching microscopic distances (approx. pixel size of 45×45 μm^2) the nanoparticle enhanced

sensor becomes more inclined to signal fluctuations due to insufficient statistics (varying fluorophore – GNP distance).

Table 4.1.1. Zero level ratio, standard deviation at zero level and limit of detection (binned area 300×300 pixels) for two ammonium sensors without GNPs (Y and P) and four with GNPs.

Sensor	Ratio	SD R	LOD (nM)	
Y	0,4608	4,65E-05	*	No GNPs
P	0,4042	1,15E-04	802	No GNPs
Q	0,6068	1,89E-05	22	Old batch GNPs high amount
R	0,5451	7,01E-05	359	Old batch GNPs low amount
M	0,4324	8,95E-05	420	New batch GNPs low amount
N	0,5133	3,01E-05	112	New batch GNPs high amount

* No response below 10 µm

Further, not only did the GNPs provide enhanced sensitivity, but also they appeared to enhance durability of the sensor. In figure 4.1.1 the almost complete recovery (>90% after 14 days) of the zero level ratiometric signal is demonstrated for NP sensor Q, while sensor P merely showed a 70 % recovery. The enhanced durability is likely due to the enhanced photo stability that the nanoparticles provide.

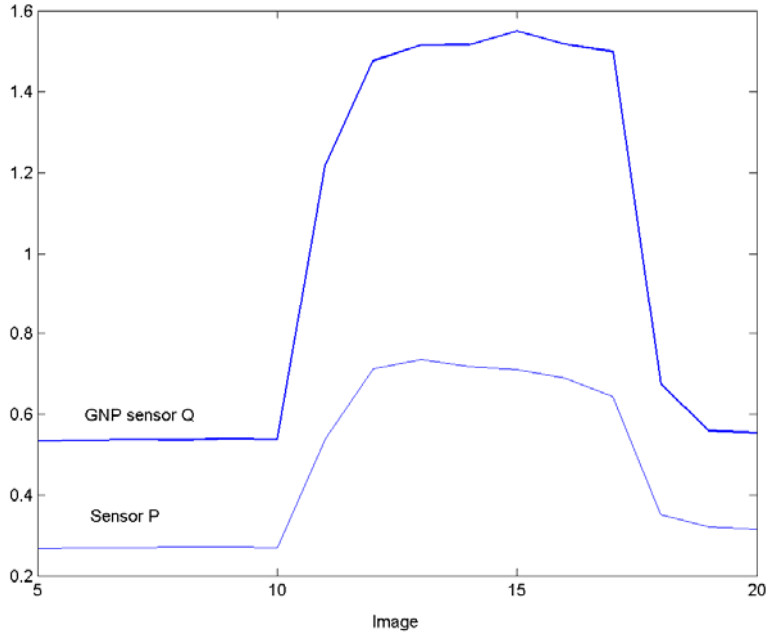

Figure 4.1.1 Binned ratiometric response for sensor Q (NPs) and P during samples (image 11 – 17) and zero level before and after samples.

The sensing scheme developed in paper V has also evolved to include ammonia measurements (Stromberg and Hakonen, manuscript). This was done by soaking the black optical isolation in silicon making it hydrophobic and impermeable for most ions and polar solvents. Ammonia is sufficiently non-polar to diffuse into the sensing membrane where it gets protonated and detected (as in the ammonium sensor) if it is slightly more acidic than in the sample matrix. However, the buffer capacity in the sensor must be quite low to avoid irreversibility. An image of a decomposing biological sample is shown in Fig. 4.1.2.

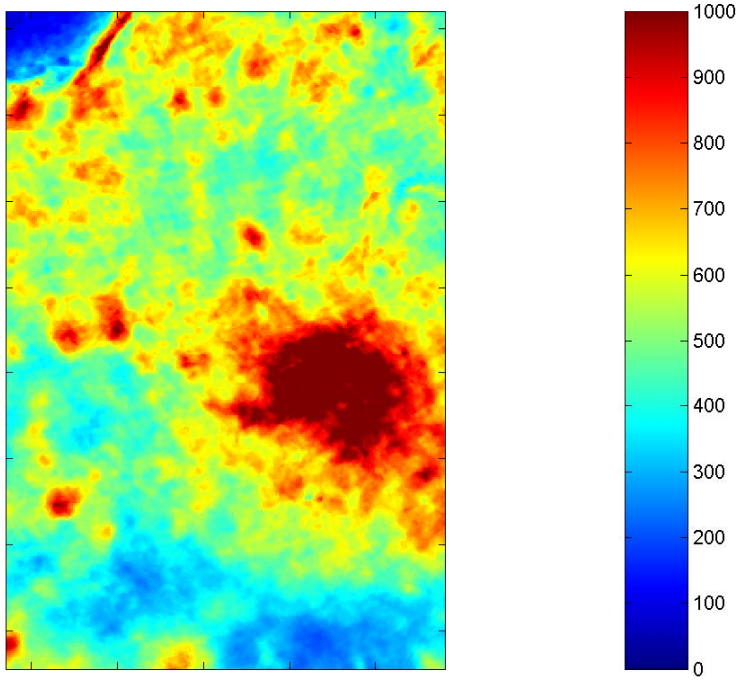

Figure 4.1.2. Imaging of ammonia concentrations at and surrounding decomposing biological samples. The colorbar demonstrates corresponding concentrations in µM and the image size is approximately 17×11 mm. The image was acquired after five days of decay.

The nanoparticle enhanced ammonia sensor demonstrated a LOD of 2 nM (34 ng/l) as a single point sensor and 20 nM (340 ng/l) at pixel level. This is somewhat better than previous optical ammonia sensors. For the best optode for ammonia (that I found) a LOD of 1 µg/l (59 nM) was reported by Waich et al. [85].

As mentioned in paper V the optimal conditions for that sensor are likely still to be revealed, this implies that the analytical performance can be far from the true limits. An indication of this is demonstrated in Fig. 4.1.3.

A

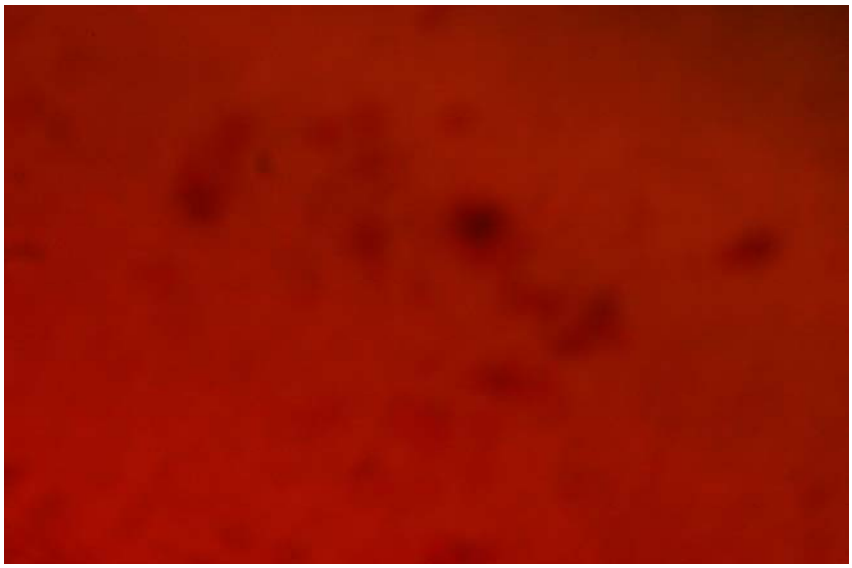

B

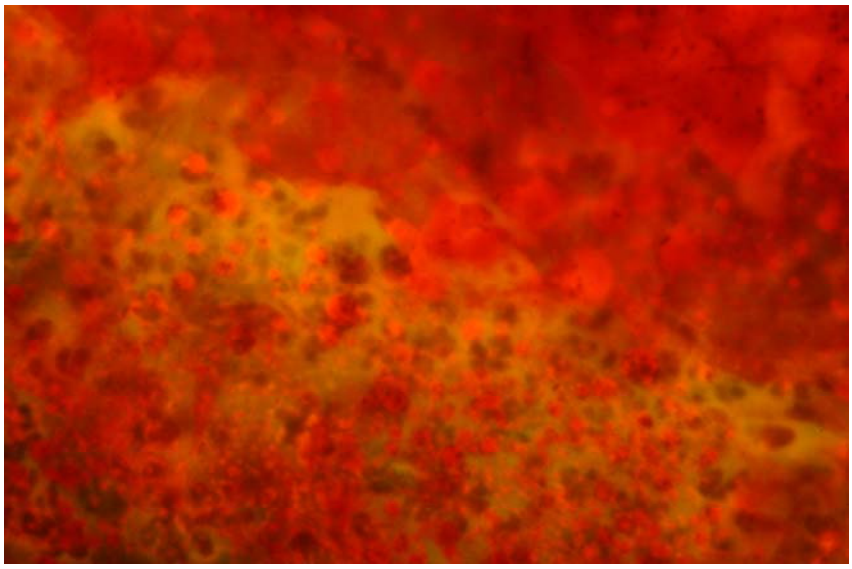

Figure 4.1.3. Fluorescence images (excitation 450 – 490 nm / emission long pass 515 nm) of: A) Dried Merocyanine 540 dye on a coverglass. B) Dried Merocyanine 540 and GNPs (~ 20 – 80 nm). The severe blue-shift in fluorescence may indicate that there are GNP sizes and/or Fluorophore-GNP distances that can cause a complete shift from red to green emission.

Important parameters to be optimized are: Amount of GNPs, size of GNPs, alkanethiol carbon chain length, type of material and angle of excitation light, of which I believe amount and size of GNPs and possibly excitation angle are the most important. However, for nanoparticle sizes approaching $0.1 \cdot \lambda$

localized surface plasmon resonance effect is weaker (i.e. ~ 50 nm for this system), which likely limits the optimization process to sizes below 50 nm [73]. Figure 4.1.4 demonstrates theoretical calculations of maximum fluorescence enhancement for gold/silver alloy nanoparticles [86]. This type of theoretical calculations could therefore conveniently provide supportive information for the optimization process.

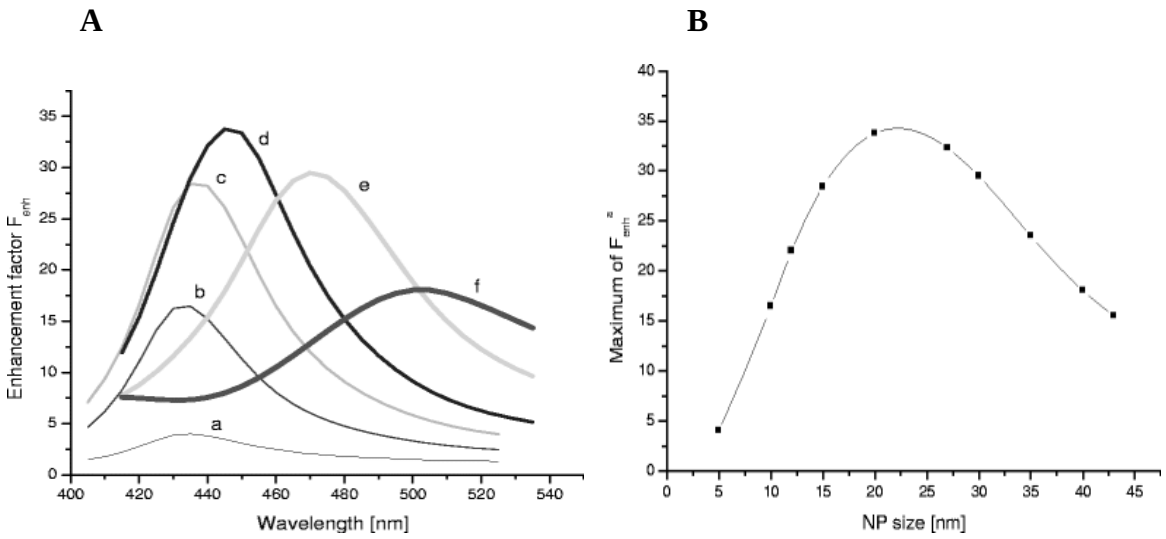

Figure 4.1.4. Adapted from [86]. **A)** Dependence of the enhancement factor on the excitation wavelength for different NP sizes. Parameters: gold/silver molar ratio x = 0.2, thickness of the silica shell d = 5 nm. Radius of the NPs *a* 5 nm, *b* 10 nm, *c* 15 nm, *d* 20 nm, *e* 30 nm, *f* 40 nm. **B)** Dependence of the maximum enhancement on the NP size. Parameters: gold/silver molar ratio x = 0.2, thickness of the silica shell d = 5 nm.

A major improvement to this sensing scheme could be achieved by reversing the emulsion to water in oil (w/o) emulsion. This would provide the interesting feature that the GNPs can be used without surface modification. One significant advantage of this approach would be to maintain full plasmon activity of the NPs (alkanethiol functionalization usually express a major reduction of plasmon absorption). Further, the sensors sensitivity towards ionic strength would likely also be eliminated, since the hydrophobic phase will face the sample. Most ions from the sample would therefore not be able to pass the hydrophobic barrier, only hydrophobic ones and the ones interacting with the ionophore.

4.2. Visions

The use of molecularly imprinted polymers (MIP) is a hot topic within analytical chemistry and separation technology. I would like to use MIPs on plasmonic nanoparticles and incorporate them in optical sensors. The thickness of the polymeric film can be optimized to fit a certain sensing scheme, with regards to enhancement and quenching, or preferably enhancement turning into quenching (similar to paper V) or vice versa. This approach can be taken a step further and be used within a capillary electrophoresis system. Within such a system the coated NPs will carry the benefit of enhanced sensitivity and selectivity for detection. The nanoparticles will also provide a pseudo stationary phase that carries additional selectivity through the separation process.

Though expected to be a versatile tool within many research areas the use of nanoparticles have also been pointed out as a serious environmental threat. Hence there is an urgent need to ensure sustainable development of nanotechnology, with appropriate risk assessments of engineered nanoparticles [87-89]. For example, there is an increasing use of silver nanoparticles for anti-bacterial and anti-fungal applications. The silver NPs are incorporated in a wide variety of products, from socks to refrigerators. Other anthropologically emitted nanoparticles includes combustion of fossile fuels which has been pointed out to be one major cause of the current elevated heart and coronary disease in urban areas [90]. This connection has frequently been verified, however physiological mechanisms for this is debated. Potentially, the most dangerous particles (at least with regards to heart and coronary disease) are particles that can penetrate deep down in the lungs, cross the lung – blood barrier, be able to freely travel with the blood and target ruptures or plaques in vascular endothelium where they cause local oxidative stress and proinflammatory effects. Potential candidates include particles below 100 nm that are water soluble and are probably charged. There are at present no standards set to limit nanoparticles in air and wastewater, therefore improved methods to detect, identify and characterize nanoparticles is warranted. A plausible pathway could be to use lipid vesicles connected by lipid nanotubes (d = 220

nm), in a similar way as Tokarz et al. [91], and transport sample with NPs with e.g. electrophoresis (Fig. 4.2.1). A major problem is likely the detection of these small particles. However, for plasmonic NPs addition of fluorophores that overlap with the plasmon peak could provide an interesting and highly sensitive method. Overall features: 1) The lipid nanotube provides a natural filter for NPs cutting off larger particles. 2) Likely quantifiable with signals immediately over 3*S.D., by in principle counting of individual NPs. 3) Determine biological availability by applying the sample outside the lipid vesicle. 4) Fourier transformations may be used to identify frequencies of different NPs in a sample, and to possibly quantify by the frequency. Applications: 1) Environmental analysis of NPs. 2) Characterization of NPs 3) Characterization of NP-fluorophore interactions (i.e. enhancement – quenching). 4) Optimize sensing systems based on fluorescence enhancement or quenching (or both).

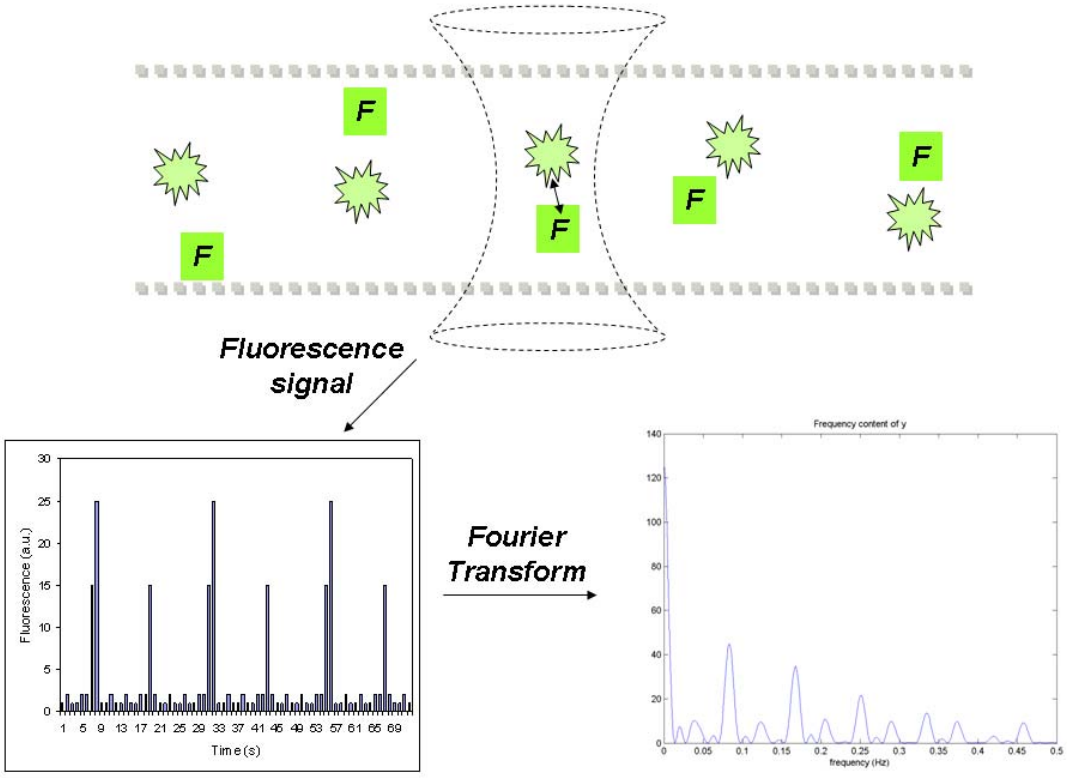

Figure 4.2.1. The top image shows a lipid nanotube with fluorophores [F] and nanoparticles being transported. The arrow indicates plasmonic interaction within the confocal volume.

Sensing techniques for nanoparticles would also be of highest interest. For this I expect similar sensing schemes as used in paper V to be useful. For example, negatively charged plasmonic nanoparticles could be detected by providing a positive charge to the inner phase (oil) of the emulsion, hence attracting the NPs. Within the oil phase there is a fluorophore that can interact with the NPs surface plasmons and therefore providing the signal change.

4.3. Conclusions

This thesis illustrates what a powerful tool optical sensors are within current measurement technology. High performance pH optodes were developed that demonstrated precisions down to 0.0029 pH units and dynamic ranges up to at least 3 pH units. Also, a nanoparticle enhanced ammonium sensor showed a preview of what tomorrow's nano engineered optical sensors, with fully realized potential, can produce. The ammonium sensor demonstrated a limit of detection as low as 1.7 nM (30 ng/l), approximately three orders of magnitude better than previous ammonium sensors. Further, the concept of enhancement and quenching interactions with nanoparticles can be implemented on in principle any ion.

Further, the work presented here demonstrates that optical sensors are remarkably suitable for high-precision high-resolution imaging, and can be used for non-invasive imaging of cellular responses.

It is also shown that time dependent calibrations are a useful complement to ratiometric measurements for signal drift compensation. This was demonstrated for a variety of optodes and a variety of time ranges, from a few hours up to 17 days.

5. Acknowledgements

In loving memory of my mother Seija Hakonen (1946 – 2009). I hope that I eventually will be able to contribute in the chase of methods for early detection of cancer.

Thank you, Stefan Hulth for fantastic support and enthusiastic response to all the scientific progress we have accomplished throughout the past five years. Scientific writing is an extremely important skill for a scientist and in my eyes you master that skill perfectly. I think (hope) that my writing is clearly influenced by the extensive writing we have done together.

Thank you, Niklas Strömberg for being my mentor and endless supply of knowledge within the areas of optics and optical sensing. We have had many fruitful scientific discussions and hopefully this will continue far beyond the point of my dissertation.

Thank you, Leif Andersson for being my supervisor (together with Stefan) during my first two years as a graduate student and lately for bringing me along in the Ocean acidification project.

Thank you, Roger Karlsson for being my second supervisor the last two years of my graduate student period. I will do the chiral separations of DFMO shortly after my dissertation!

Thank you, Erik Mattsson for doing most of the practical work for paper III and found the article that brought DHPDS (used in paper IV) to my attention.

Thank you, Suzanne, Stina and Malin, for good collaboration during various aquaria experiments.

Thank you, Johan Engelbrektsson for technical support throughout my graduate student period, and now especially for Labview assistance for the Ocean acidification project.

Thank you, Tobias Larsson for computer assistance, mainly concerning the Fluoromax computer, during my first year as a graduate student.

Thank you, Esa and Alpo, for excellent technical support.

Thank you everybody at AMK, both former and present oodles, for providing a friendly atmosphere.

Thank you all my friends for lots of fun!

Thank you dad, for all support you have provided throughout the years. I can just wish that I could be such a generous person that you are. You are the best!

Thank you, Bodil for being a perfect wife as well as a source of hot information from your own research. I love you forever!

Thank you, my wonderful children Clara and Rasmus. You both have fantastic capabilities that I hope you will evolve in your future lives.

6. References

[1] K. Caldeira, M.E. Wickett, Anthropogenic carbon and ocean pH, Nature 425 (2003) 365-365.

[2] B.N.G. Giepmans, S.R. Adams, M.H. Ellisman, R.Y. Tsien, Review - The fluorescent toolbox for assessing protein location and function, Science 312 (2006) 217-224.

[3] D.A. Giljohann, C.A. Mirkin, Drivers of biodiagnostic development, Nature 462 (2009) 461-464.

[4] W. Min, S.J. Lu, S.S. Chong, R. Roy, G.R. Holtom, X.S. Xie, Imaging chromophores with undetectable fluorescence by stimulated emission microscopy, Nature 461 (2009) 1105-1109.

[5] X.K. Shu, A. Royant, M.Z. Lin, T.A. Aguilera, V. Lev-Ram, P.A. Steinbach, R.Y. Tsien, Mammalian Expression of Infrared Fluorescent Proteins Engineered from a Bacterial Phytochrome, Science 324 (2009) 804-807.

[6] R.Y. Tsien, Imagining imaging's future, Nat. Rev. Mol. Cell Biol. (2003) SS16-SS21.

[7] N. Engheta, Circuits with light at nanoscales: Optical nanocircuits inspired by metamaterials, Science 317 (2007) 1698-1702.

[8] J. Heber, Plasmonics: Surfing the wave, Nature 461 (2009) 720-722.

[9] R.W. Murray, Nanoelectrochemistry: Metal nanoparticles, nanoelectrodes, and nanopores, Chem. Rev. 108 (2008) 2688-2720.

[10] P. Nagpal, N.C. Lindquist, S.H. Oh, D.J. Norris, Ultrasmooth Patterned Metals for Plasmonics and Metamaterials, Science 325 (2009) 594-597.

[11] H. Nakanishi, K.J.M. Bishop, B. Kowalczyk, A. Nitzan, E.A. Weiss, K.V. Tretiakov, M.M. Apodaca, R. Klajn, J.F. Stoddart, B.A. Grzybowski, Photoconductance and inverse photoconductance in films of functionalized metal nanoparticles, Nature 460 (2009) 371-375.

[12] E. Ozbay, Plasmonics: Merging photonics and electronics at nanoscale dimensions, Science 311 (2006) 189-193.

[13] A. Polman, APPLIED PHYSICS Plasmonics Applied, Science 322 (2008) 868-869.

[14] C. McDonagh, C.S. Burke, B.D. MacCraith, Optical chemical sensors, Chem. Rev. 108 (2008) 400-422.

[15] J.R. Lakowicz, Principles of Fluorescence Spectroscopy, 2 ed., Kluwer Academic and Plenum, New York, 1999.

[16] R.P. Haugland, The Handbook: A guide to fluorescent probes and labeling technologies, 10 ed., Invitrogen Corp. 2005.

[17] R.B. Thompson, J.R. Lakowicz, Fiber Optic Ph Sensor Based on Phase Fluorescence Lifetimes, Analytical Chemistry 65 (1993) 853-856.

[18] G. Liebsch, I. Klimant, C. Krause, O.S. Wolfbeis, Fluorescent imaging of pH with optical sensors using time domain dual lifetime referencing, Analytical Chemistry 73 (2001) 4354-4363.

[19] I. Bergman, Rapid-Response Atmospheric Oxygen Monitor Based on Fluorescence Quenching, Nature 218 (1968) 396-&.

[20] H. Stahl, A. Glud, C.R. Schroder, I. Klimant, A. Tengberg, R.N. Glud, Time-resolved pH imaging in marine sediments with a luminescent planar optode, Limnol. Oceanogr. Meth. 4 (2006) 336-345.

[21] S.R. Scheicher, B. Kainz, S. Kostler, M. Suppan, A. Bizzarri, D. Pum, U.B. Sleytr, V. Ribitsch, Optical oxygen sensors based on Pt(II) porphyrin dye immobilized on S-layer protein matrices, Biosens. Bioelectron. 25 (2009) 797-802.

[22] S.M. Ji, W.H. Wu, Y.B. Wu, T.Y. Zhao, F.K. Zhou, Y.B. Yang, X. Zhang, X.F. Liang, W.T. Wu, L.N. Chi, Z.G. Wang, J.Z. Zhao, Real-time monitoring of luminescent lifetime changes of PtOEP oxygen sensing film with LED/photodiode-based time-domain lifetime device, Analyst 134 (2009) 958-965.

[23] C. Maule, H. Gonçalves, C. Mendonça, P. Sampaio, J.C.G. Esteves da Silva, P. Jorge, Wavelength encoded analytical imaging and fiber optic sensing with pH sensitive CdTe quantum

dots, Talanta 80 1932-1938.
[24] Z. Zhujun, W.R. Seitz, A Fluorescence Sensor for Quantifying Ph in the Range from 6.5 to 8.5, Analytica Chimica Acta 160 (1984) 47-55.
[25] R.Y. Tsien, M. Poenie, Fluorescence Ratio Imaging - A New Window Into Intracellular Ionic Signaling, Trends In Biochemical Sciences 11 (1986) 450-455.
[26] H. Hochreiner, I. Sanchez-Barragan, J.M. Costa-Fernandez, A. Sanz-Medel, Dual emission probe for luminescence oxygen sensing: a critical comparison between intensity, lifetime and ratiometric measurements, Talanta 66 (2005) 611-618.
[27] R.B. Thompson, E.R. Jones, Enzyme-Based Fiber Optic Zinc Biosensor, Analytical Chemistry 65 (1993) 730-734.
[28] E.J. Park, M. Brasuel, C. Behrend, M.A. Philbert, R. Kopelman, Ratiometric optical PEBBLE nanosensors for real-time magnesium ion concentrations inside viable cells, Analytical Chemistry 75 (2003) 3784-3791.
[29] R. Badugu, J.R. Lakowicz, C.D. Geddes, Wavelength-ratiometric probes for the selective detection of fluoride based on the 6-aminoquinolinium nucleus and boronic acid moiety, Journal of Fluorescence 14 (2004) 693-703.
[30] A. Ojida, H. Nonaka, Y. Miyahara, S.I. Tamaru, K. Sada, I. Hamachi, Bis(Dpa-Zn-II) appended xanthone: Excitation ratiometric chemosensor for phosphate anions, Angewandte Chemie-International Edition 45 (2006) 5518-5521.
[31] H. Xu, J.W. Aylott, R. Kopelman, T.J. Miller, M.A. Philbert, A real-time ratiometric method for the determination of molecular oxygen inside living cells using sol-gel-based spherical optical nanosensors with applications to rat C6 glioma, Analytical Chemistry 73 (2001) 4124-4133.
[32] K. Kurihara, M. Ohtsu, T. Yoshida, T. Abe, H. Hisamoto, K. Suzuki, Micrometer-sized sodium ion-selective optodes based on a "tailed" neutral ionophore, Analytical Chemistry 71 (1999) 3558-3566.
[33] N. Stromberg, S. Hulth, Ammonium selective fluorosensor based on the principles of coextraction, Analytica Chimica Acta 443 (2001) 215-225.
[34] D.A. Williams, K.E. Fogarty, R.Y. Tsien, F.S. Fay, Calcium Gradients in Single Smooth-Muscle Cells Revealed by the Digital Imaging Microscope Using Fura-2, Nature 318 (1985) 558-561.
[35] W. Scheenen, L.R. Makings, L.R. Gross, T. Pozzan, R.Y. Tsien, Photodegradation of indo-1 and its effect on apparent Ca2+ concentrations, Chemistry & Biology 3 (1996) 765-774.
[36] O.S. Wolfbeis, E. Furlinger, H. Kroneis, H. Marsoner, Fluorimetric Analysis .1. a Study on Fluorescent Indicators for Measuring near Neutral (Physiological) Ph-Values, Fresenius Zeitschrift Fur Analytische Chemie 314 (1983) 119-124.
[37] O.S. Wolfbeis, Fluorescence Optical Sensors In Analytical-Chemistry, Trac-Trends In Analytical Chemistry 4 (1985) 184-188.
[38] F.X. Felberbauer, J. Graf, Fiberoptic Measurement of Intracellular Ph in Intact Rat-Liver Using Ph-Sensitive Dyes, Pflugers Archiv-European Journal of Physiology 419 (1991) 215-217.
[39] X.D. Ge, M. Hanson, H. Shen, Y. Kostov, K.A. Brorson, D.D. Frey, A.R. Moreira, G. Rao, Validation of an optical sensor-based high-throughput bioreactor system for mammalian cell culture, J. Biotechnol. 122 (2006) 293-306.
[40] A. Hakonen, S. Hulth, A high-precision ratiometric fluorosensor for pH: Implementing time-dependent non-linear calibration protocols for drift compensation, Analytica Chimica Acta 606 (2008) 63-71.
[41] T. Forster, Fluoreszenzspektrum Und Wasserstoffionenkonzentration, Naturwissenschaften 36 (1949) 186-187.
[42] A. Hakonen, S. Hulth, A high-performance fluorosensor for pH measurements between 6 and 9, Talanta 80 (2010) 1964-1969.
[43] N. Stromberg, E. Mattsson, A. Hakonen, An imaging pH optode for cell studies based on covalent attachment of 8-hydroxypyrene-1,3,6-trisulfonate to amino cellulose acetate films, Analytica Chimica Acta 636 (2009) 89-94.

[44] Q.Z. Zhu, R.C. Aller, Y.Z. Fan, High-performance planar pH fluorosensor for two-dimensional pH measurements in marine sediment and water, Environmental Science & Technology 39 (2005) 8906-8911.
[45] P.C.A. Jeronimo, A.N. Araujo, M. Montenegro, Optical sensors and biosensors based on sol-gel films, Talanta 72 (2007) 13-27.
[46] D.A. Nivens, M.V. Schiza, S.M. Angel, Multilayer sol-gel membranes for optical sensing applications: single layer pH and dual layer CO2 and NH3 sensors, Talanta 58 (2002) 543-550.
[47] D. Wencel, B.D. MacCraith, C. McDonagh, High performance optical ratiometric sol-gel-based pH sensor, Sensors and Actuators B-Chemical 139 (2009) 208-213.
[48] S.A. Borman, Optrodes, Analytical Chemistry 53 (1981) A616-A618.
[49] W.R. Seitz, Chemical Sensors Based on Fiber Optics, Analytical Chemistry 56 (1984) A16-&.
[50] X.P. Li, Z. Rosenzweig, A fiber optic sensor for rapid analysis of bilirubin in serum, Analytica Chimica Acta 353 (1997) 263-273.
[51] S. Hulth, R.C. Aller, P. Engstrom, E. Selander, A pH plate fluorosensor (optode) for early diagenetic studies of marine sediments, Limnology And Oceanography 47 (2002) 212-220.
[52] A. Tengberg, J. Hovdenes, H.J. Andersson, O. Brocandel, R. Diaz, D. Hebert, T. Arnerich, C. Huber, A. Kortzinger, A. Khripounoff, F. Rey, C. Ronning, J. Schimanski, S. Sommer, A. Stangelmayer, Evaluation of a lifetime-based optode to measure oxygen in aquatic systems, Limnol. Oceanogr. Meth. 4 (2006) 7-17.
[53] Q.Z. Zhu, R.C. Aller, Y.Z. Fan, A new ratiometric, planar fluorosensor for measuring high resolution, two-dimensional pCO(2) distributions in marine sediments, Marine Chemistry 101 (2006) 40-53.
[54] Q.Z. Zhu, R.C. Aller, Y.Z. Fan, Two-dimensional pH distributions and dynamics in bioturbated marine sediments, Geochimica Et Cosmochimica Acta 70 (2006) 4933-4949.
[55] R.N. Glud, N.B. Ramsing, J.K. Gundersen, I. Klimant, Planar optrodes: A new tool for fine scale measurements of two-dimensional O-2 distribution in benthic communities, Marine Ecology-Progress Series 140 (1996) 217-226.
[56] S.M. Borisov, O.S. Wolfbeis, Temperature-sensitive europium(III) probes and their use for simultaneous luminescent sensing of temperature and oxygen, Analytical Chemistry 78 (2006) 5094-5101.
[57] S.M. Barnard, D.R. Walt, A Fiberoptic Chemical Sensor with Discrete Sensing Sites, Nature 353 (1991) 338-340.
[58] J. Ji, Z. Rosenzweig, Fiber optic pH/Ca2+ fluorescence microsensor based on spectral processing of sensing signals, Analytica Chimica Acta 397 (1999) 93-102.
[59] J. Janata, Do Optical Sensors Really Measure Ph, Analytical Chemistry 59 (1987) 1351-1356.
[60] N. Stromberg, S. Hulth, A fluorescence ratiometric detection scheme for ammonium ions based on the solvent sensitive dye MC 540, Sensors and Actuators B-Chemical 90 (2003) 308-318.
[61] N. Stromberg, S. Hulth, Time correlated pixel-by-pixel calibration for quantification and signal quality control during solute imaging, Sensors and Actuators B-Chemical 115 (2006) 263-269.
[62] N. Stromberg, S. Hulth, Assessing an imaging ammonium sensor using time correlated pixel-by-pixel calibration, Analytica Chimica Acta 550 (2005) 61-68.
[63] Y. Tang, E.C. Tehan, Z.Y. Tao, F.V. Bright, Sol-gel-derived sensor materials that yield linear calibration plots, high sensitivity, and long-term stability, Analytical Chemistry 75 (2003) 2407-2413.
[64] E.J. Wang, K.F. Chow, V. Kwan, T. Chin, C. Wong, A. Bocarsly, Fast and long term optical sensors for pH based on sol-gels, Analytica Chimica Acta 495 (2003) 45-50.
[65] B.D. MacCraith, C. McDonagh, Enhanced fluorescence sensing using sol-gel materials, J. Fluoresc. 12 (2002) 333-342.
[66] C. von Bultzingslowen, A.K. McEvoy, C. McDonagh, B.D. MacCraith, I. Klimant, C. Krause, O.S. Wolfbeis, Sol-gel based optical carbon dioxide sensor employing dual luminophore referencing for application in food packaging technology, Analyst 127 (2002) 1478-1483.

[67] I.H. Huisman, G. Tragardh, Determining the zeta potential of ultrafiltration membranes using their salt retention, Colloid Surf. A-Physicochem. Eng. Asp. 157 (1999) 261-268.
[68] M.F. Choi, Spectroscopic behaviour of 8-hydroxy-1,3,6-pyrenetrisulphonate immobilized in ethyl cellulose, Journal Of Photochemistry And Photobiology A-Chemistry 104 (1997) 207-212.
[69] N. Stromberg, Determination of ammonium turnover and flow patterns close to roots using Imaging optodes, Environmental Science & Technology 42 (2008) 1630-1637.
[70] A. Hakonen, S. Hulth, S. Dufour, Analytical performance during ratiometric long-term imaging of pH in bioturbated sediments., Talanta (2010).
[71] J.R. Lakowicz, Radiative Decay Engineering: Biophysical and Biomedical Applications, Analytical Biochemistry 298 (2001) 1.
[72] J.R. Lakowicz, Radiative decay engineering 5: metal-enhanced fluorescence and plasmon emission, Analytical Biochemistry 337 (2005) 171-194.
[73] C. McDonagh, O. Stranik, R. Nooney, B.D. MacCraith, Nanoparticle strategies for enhancing the sensitivity of fluorescence-based biochips, Nanomedicine 4 (2009) 645-656.
[74] P. Andrew, W.L. Barnes, Energy transfer across a metal film mediated by surface plasmon polaritons, Science 306 (2004) 1002-1005.
[75] P.P. Pompa, L. Martiradonna, A. Della Torre, F. Della Sala, L. Manna, M. De Vittorio, F. Calabi, R. Cingolani, R. Rinaldi, Metal-enhanced fluorescence of colloidal nanocrystals with nanoscale control, Nature Nanotechnology 1 (2006) 126-130.
[76] A.W. Wark, H.J. Lee, A.J. Qavi, R.M. Corn, Nanoparticle-enhanced diffraction gratings for ultrasensitive surface plasmon biosensing, Analytical Chemistry 79 (2007) 6697-6701.
[77] M. Scharte, R. Porath, T. Ohms, M. Aeschlimann, J.R. Krenn, H. Ditlbacher, F.R. Aussenegg, A. Liebsch, Do Mie plasmons have a longer lifetime on resonance than off resonance?, Applied Physics B-Lasers and Optics 73 (2001) 305-310.
[78] K. Ray, M.H. Chowdhury, J.R. Lakowicz, Aluminum nanostructured films as substrates for enhanced fluorescence in the ultraviolet-blue spectral region, Anal. Chem. 79 (2007) 6480-6487.
[79] G.W. Ford, W.H. Weber, Electromagnetic-Interactions of Molecules with Metal-Surfaces, Physics Reports-Review Section of Physics Letters 113 (1984) 195-287.
[80] K.H. Drexhage, Influence of a Dielectric Interface on Fluorescence Decay Time, Bulletin of the American Physical Society 14 (1969) 873-&.
[81] A. Campion, A.R. Gallo, C.B. Harris, H.J. Robota, P.M. Whitmore, Electronic energy transfer to metal surfaces: a test of classical image dipole theory at short distances, Chemical Physics Letters 73 (1980) 447.
[82] K. Sokolov, G. Chumanov, T.M. Cotton, Enhancement of molecular fluorescence near the surface of colloidal metal films, Analytical Chemistry 70 (1998) 3898-3905.
[83] N. Stromberg, J. Engelbrektsson, S. Delin, A high throughput optical system for imaging optodes, Sens. Actuator B-Chem. 140 (2009) 418-425.
[84] A. Hakonen, Plasmon Enhancement and Surface Wave Quenching for Phase Ratiometry in Coextraction-Based Fluorosensors, Analytical Chemistry 81 (2009) 4555-4559.
[85] K. Waich, T. Mayr, I. Klimant, Fluorescence sensors for trace monitoring of dissolved ammonia, Talanta 77 (2008) 66-72.
[86] O. Stranik, R. Nooney, C. McDonagh, B.D. MacCraith, Optimization of nanoparticle size for plasmonic enhancement of fluorescence, Plasmonics 2 (2007) 15-22.
[87] V.L. Colvin, The potential environmental impact of engineered nanomaterials, Nat. Biotechnol. 21 (2003) 1166-1170.
[88] M. Hassellov, J.W. Readman, J.F. Ranville, K. Tiede, Nanoparticle analysis and characterization methodologies in environmental risk assessment of engineered nanoparticles, Ecotoxicology 17 (2008) 344-361.
[89] A.D. Maynard, R.J. Aitken, T. Butz, V. Colvin, K. Donaldson, G. Oberdorster, M.A. Philbert, J. Ryan, A. Seaton, V. Stone, S.S. Tinkle, L. Tran, N.J. Walker, D.B. Warheit, Safe handling of nanotechnology, Nature 444 (2006) 267-269.

[90] A.K. Madl, K.E. Pinkerton, Health effects of inhaled engineered and incidental nanoparticles, Crit. Rev. Toxicol. 39 (2009) 629-658.
[91] M. Tokarz, B. Hakonen, P. Dommersnes, O. Orwar, B. Akerman, Electrophoretic transport of latex particles in lipid nanotubes, Langmuir 23 (2007) 7652-7658.

Paper I

Talanta xxx (2010) xxx–xxx

Contents lists available at ScienceDirect

Talanta

journal homepage: www.elsevier.com/locate/talanta

Analytical performance during ratiometric long-term imaging of pH in bioturbated sediments

Aron Hakonen[a,*], Stefan Hulth[a], Suzanne Dufour[b]

[a] Department of Chemistry, University of Gothenburg, SE-412 96 Göteborg, Sweden
[b] Department of Earth and Planetary Sciences, McGill University, 3450 University Street, Montreal, QC, Canada

ARTICLE INFO

Article history:
Received 14 October 2009
Received in revised form 8 February 2010
Accepted 13 February 2010
Available online xxx

Keywords:
pH optode
Fluorescence imaging
Thyasira sarsi
Bioturbation

ABSTRACT

In this study, the long-term analytical performance of a high-resolution ratiometric imaging sensor for pH was quantitatively determined. The sensor was applied in an experimental microcosm to illustrate biogeochemical consequences from mining activities by the chemosymbiotic bivalve *Thyasira sarsi*. Utilizing time-correlated pixel-by-pixel calibration protocols during imaging, close to 90% of the pixels were associated with a precision (S.D.) of <0.05 pH units at the end of an experimental period of 17 days. For comparison, a precision of <0.05 pH units was achieved for less than 50% of the pixels throughout experiments using conventional pre-sample calibration procedures. The average standard deviation of pixels was 0.01 pH units. Image analysis of single pixel derivatives and pH measurements over time suggested that *T. sarsi* affect pH distributions and general sediment geochemistry more than would be expected based on the small size of the bivalves. A significant decrease of pH in the overlying water suggested a considerable release of reduced compounds from the exhalent stream of the thyasirids. Strong pH gradients were demonstrated not only across the sediment–water interface but, also associated with bioturbation activities immediately adjacent to *T. sarsi* burrowing tracts, inhalant tubes and pedal tracts in the sediment matrix. Gradients of up to 1.16 pH units per mm were observed.

1. Introduction

Optical sensors (optodes) have been found suitable for high-resolution imaging of gas and solute distributions in complex environments such as soil, aquatic sediments and living cells [1–6]. Typically, imaging optodes are made from a translucent thin polymer film or a sol–gel in which a solute sensitive fluorescent dye is immobilized by e.g. ionic interactions or covalent attachment [4,6–11]. After equilibration with the sample matrix (e.g. sediment pore water), the indicator film is illuminated and the light emitted from the sensor is collected on a CCD chip to obtain a two-dimensional image of solute distributions.

Analytical protocols for the normalization of artifacts and signal quality control are crucial in the design and use of intensity-based imaging optodes [12]. Although frequently used in a variety of applications, optical sensors are commonly susceptible to a drift in sensor response [7,8,12]. Sensor drift is a phenomenon only rarely acknowledged or fully compensated for by appropriate analytical protocols [12]. Several spectroscopic techniques and analytical calibration protocols, including the detection of luminescence by fluorescence lifetime and fluorescence ratiometry, are designed to normalize for signal drift and for sensor response not associated with changes in analyte concentration [7,13–15]. The wavelength ratiometric normalization procedure is intended to efficiently remove artifacts in sensor response caused by e.g. variations in excitation light intensities, heterogeneous distribution of the indicator dye, photobleaching and leaching of the indicator dye [14,16]. For a ratiometric ammonium sensor, induced variations in oxygen concentrations, excitation light intensity and pH were more or less completely accounted for by the ratiometric procedure. It was, however, not possible to eliminate artifacts associated with fluctuations in temperature, effective indicator concentrations and sample ionic strength [17]. Fluorescence lifetime is a procedure often assumed insensitive to most analytical artifacts and therefore considered advantageous compared to, for example, the ratiometric approach. For a luminescent oxygen sensor, however, normalization by wavelength ratiometry improved the quality of measurements at least as much as sensing using fluorescence lifetime [15]. Stahl et al. [18] introduced an imaging sensor for pH based on time domain dual-lifetime referencing (t-DLR) into a sediment mesocosm. There was a continuous drift in the lifetime-ratiometric response (>0.1 pH unit) of this sensor during exposure to a phosphate buffer solution for 4 days. The authors presented an overall accuracy of ±0.1 pH units and from the data a spatial resolution of ~0.1 pH unit could be calculated.

The time-correlated pixel-by-pixel calibration protocol, either utilizing linear or non-linear parameterization, provides a promis-

* Corresponding author. Fax: +46 31 772 13 94.
E-mail address: hakonen@chem.gu.se (A. Hakonen).

0039-9140/$ – see front matter © 2010 Elsevier B.V. All rights reserved.
doi:10.1016/j.talanta.2010.02.041

ing approach to further reduce artifacts during ratiometric fluorescence imaging with a unique set of calibrations for each pixel and time of measurement [8,12,19].

With increasing reports of low oxygen or anoxic conditions in coastal marine bottom waters world-wide [20,21], an appropriate understanding of the response of benthic communities to oxygen deficiency and organic enrichment is critical for remediation and a sustainable recovery of coastal ecosystems. For example, during re-colonization following eutrophication events, anoxic sediment layers may be re-oxidized through the irrigation and particle reworking activities (i.e. bioturbation) of early successional-stage benthic macrofauna [20]. In some habitats, early colonists include species that benefit from living near oxic/anoxic interfaces, such as invertebrates living in symbiosis with chemoautotrophic bacteria. Like other invertebrates bearing sulfide-oxidizing bacterial symbionts, the chemosymbiotic bivalve *Thyasira sarsi* requires access to both reduced sulfur and an energetically favorable oxidant for the successful maintenance of the symbionts on which they feed [22]. Irrigation and oxidation of burrows, cavities and sediment regions associated with *T. sarsi* pedal tracts may not only influence the community succession in *T. sarsi* habitats, but also affect the biogeochemistry and local cycling of redox sensitive elements such as iron and sulfur [23,24].

In this study, redox gradients as a direct result from organic matter mineralization, particle redistribution and irrigation by macrofauna were quantified by a high-resolution ratiometric imaging sensor for pH. The use of pH- instead of oxygen-imaging sensors was justified given the rapid consumption of oxygen introduced to anoxic sediments, which limits its detection over timescales larger than seconds. Biogeochemical consequences from oxygen within sediments and burrow constructions can, however, be inferred from ensuing chemically- or biologically-mediated redox reactions. Imaging studies have demonstrated that macrofaunal bioturbation may affect distributions of pH and CO_2 for several days [3,25]. While H^+ is produced indirectly during microbial aerobic respiration, pH is directly affected in additional redox reactions that do not involve oxygen as an oxidant, or organic matter as a reductant. Examples include the diagenetic suite of reactions during organic matter mineralization (i.e. NO_3^-—denitrification, Mn(IV)/Fe(III) and SO_4^{2-}—reduction), as well as the reoxidation of NH_4^+ (nitrification), Mn^{2+}/Fe^{2+}, and HS- by oxygen or other oxidants [26,27]. Furthermore, oceanic uptake of anthropogenic CO_2 is presently altering the chemical signature of the world's oceans [28], with potential consequences for marine organisms, ecosystem functioning, and biogeochemical feedbacks, e.g. [29]. The majority of investigations on seawater acidification have focused on open water systems while; in contrast, benthic systems have only rarely been considered. The sensitivity and resilience of coastal benthic ecosystems towards a reduced pH in the overlying water are therefore virtually unknown.

The main objective of this study was to quantitatively evaluate the long-term analytical performance of a high-resolution ratiometric imaging sensor for pH, and to experimentally illustrate the versatility of imaging sensors in bioturbated sediments. To the best of our knowledge, there are no previous studies that include experimental data on the analytical performance of imaging sensors throughout experiments. Although Zhu et al. performed a 16-day study of pH distributions following macrofaunal reworking in marine sediments, no data on the analytical performance of the sensor during the experiment was presented [30].

Analytical procedures included ratiometric normalization of fluorescence and time-correlated pixel-by-pixel calibrations. Ecological implications of pH modifications in surface sediments as a consequence of *T. sarsi* activities are presented elsewhere (Dufour et al., manuscript).

2. Materials and procedures

2.1. General overview

Two adult specimens of *T. sarsi* were introduced to an experimental microcosm with sediment and overlying seawater, and net effects from faunal activities were periodically quantified by high-resolution imaging of pH distributions. There were 4 days between the collection of bivalves and the initiation of pH imaging. The sensor was applied into the experimental system and calibrated in the beginning and at the end of the experiment. Sensor operation lasted 17 days.

Bivalves and sediment were collected by an Olausson box-corer from the deepest part of the Gullmarsfjord (Alsbäck, 118 m), western Sweden. Surface sediment (~20 cm depth) was wet-sieved (1 mm grid) for use in the experimental microcosm. Retrieved specimens of *T. sarsi* (6–8 mm length) were kept in flow-through containers with unfiltered seawater (continuously supplied deep-water, 8°C) and sediment until their introduction to the microcosm 7 days later. The sampling site is exposed to seasonal cycles of bottom water oxygenation and organic matter deposition [31,32]. Due to high concentrations of Mn- and Fe-oxides in the solid phase of the sediment [33], sulfides are likely to be metal-bound. As a consequence, free sulfide is rarely released to the overlying bottom water despite periodically low oxygen concentrations. At this site, the organic content of the sediment is ~3% and the C/N ratio of the solid phase ~10 [33].

2.2. Experimental microcosm

The experimental microcosm (aquarium) was made in-house from two plates of transparent plexiglass (200 mm × 240 mm × 5 mm), separated by a silicone tube and fixed together by plastic screws and clamps. The aquarium was directly mounted on a PVC box containing the optical system (Fig. 1). The front wall of the microcosm could be quickly removed, providing easy access to the inner wall of the aquarium for sensor introduction and calibration. The inner width of the assembled aquarium was ~10 mm. On day 1, the aquarium was partially filled with a slurry of wet-sieved sediment which was allowed to settle for 2 days prior to the addition of two specimens of *T. sarsi*. During the course of experiment, a separate pump-system continuously supplied un-filtered, oxygenated deep-water from the Gullmarsfjord (Fig. 1). This water has a composition close to that of the sampling site. At the end of experiment, the microcosm was X-rayed (Andrex Smart, 300 kV, exposure 80 kV/1 mA, focal distance 60 cm, exposure time 4.5 min) to locate the thyasirids and their burrows. All experiments were performed in the dark in a temperature controlled (10 °C) wet-laboratory.

2.3. Fluorosensor

The ratiometric imaging pH sensor was prepared according to [3]. In brief, a 15 cm × 20 cm sheet (100 μm polyester support, 10 μm cellulose acetate sensor layer) of transparent overhead film (HP C3835A) was immersed over night in filtered seawater with the pH sensitive ratiometric fluorophore 8-hydroxypyrene 1,3,6-trisulfonic acid (HPTS, 7.5 μM, >97%, Sigma Aldrich). The sensor was immersed in filtered seawater for 24 h prior to attachment to the inner wall of the microcosm. A black sheet of paper (120 μm thick) secured between the sensor foil and the sediment was used as optical isolation and mechanical protection. Total thickness of the immersed sensing layer and optical isolation was 200–300 μm due to the passive uptake of water during preconditioning.

Please cite this article in press as: A. Hakonen, et al., Talanta (2010), doi:10.1016/j.talanta.2010.02.041

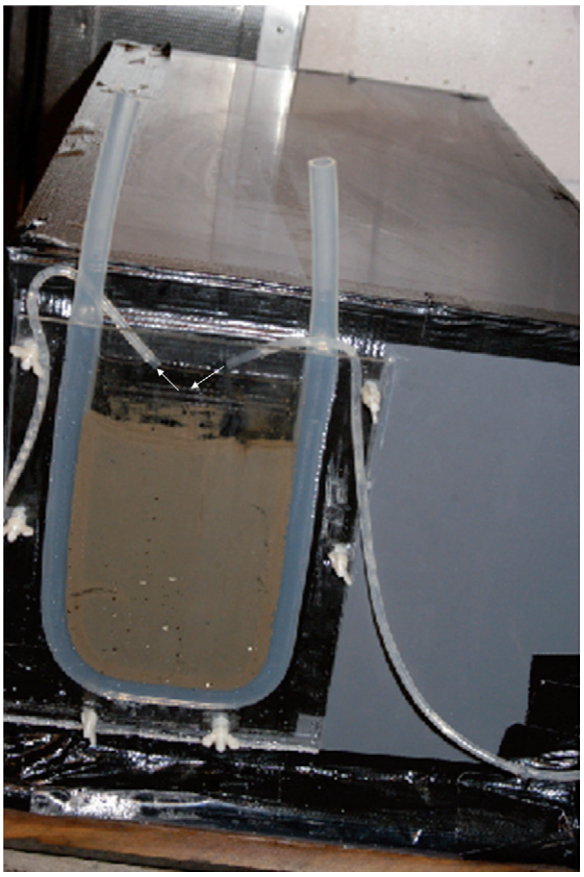

Fig. 1. The experimental microcosm (aquarium) was made from two plates of transparent plexiglass (200 mm × 240 mm × 5 mm), separated by a silicone tube. The inner width of the assembled aquarium was ~10 mm. The arrows indicate the in- and outflow of seawater. Observe that the inflow is directed to the left side of the aquarium which corresponds to the right-hand side of the optode images.

2.4. Optical setup

The optical system for imaging of pH included a 300 W xenon UV/VIS arc lamp with interchangeable band-pass filters (405 BP10 and 450 BP10 nm), a liquid light-guide, and a 16-bit CCD camera (Apogee Alta U13, 1280 × 1024 pixel resolution). A band-pass filter (510 BP10 nm) fixed between the Nikon standard SLR objective and the CCD chip provided appropriate emission wavelength. Pixels were binned 2 × 2, i.e. the effective pixel size was 277 μm × 277 μm. Sensor response 1–2 cm from the edge of the sensor was excluded from further treatment to minimize edge effects. Actual image size used for quantification was therefore 8.3 cm × 12.2 cm ($w \times h$, area ≈101 cm^2). The dual excitation filter switch and the CCD camera were controlled by the software InCytIm2 and MaxImDL/CCD 4.51, respectively. The liquid light-guide, the CCD camera and the aquarium were fixed to an optical breadboard and enclosed within a dark-grey PVC box made in-house to minimize interferences from background light and to protect the CCD camera from the corrosive atmosphere in the wet-laboratory.

2.5. Sensor calibrations

The aquarium was filled with unfiltered seawater during the initial sensor calibrations performed prior to the addition of sediment and bivalves. Additions of 200 mM HCl sequentially adjusted pH of the seawater to 8.196, 7.981, 7.639, 7.393, 7.145, 7.011, 6.755 and 6.587. Five consecutive images of the fluorescence ratio ($R = F_1/F_2$) were acquired at each pH. A pH-electrode (model 6.0232.100, 780 pH meter; Metrohm Ltd.) was used to determine the pH (NIST) of the calibration solutions. At the end of experiment, the microcosm was dismantled, the sediment gently removed and the surface of the optical sensor carefully rinsed with seawater. The sensor calibration procedure was repeated at pH 8.170, 7.967, 7.679, 7.368, 7.190, 7.030 6.862 and 6.715. Set of calibrations were linearly linked in time to provide a unique calibration in each pixel at each time of sampling [12].

2.6. Image acquisition and analysis

After adding the two bivalves, 68 images were acquired over a period of 8 days (day 3 to day 11) for long-term imaging of pH in bioturbated sediments. An additional 12 images were taken before ($n = 6$) and after ($n = 6$) the sediment was X-rayed at the end of experiments (day 17). During the course of experiments, images were primarily taken from 8 AM to 9 PM. Occasionally and in response to visual observations of faunal activities, images were acquired more frequently. The following image sequence was preset: (1) $F_{2,dark}$ ($\lambda_{ex/em}$: 450/510 nm, camera shutter closed); (2) $F_{2,light}$ ($\lambda_{ex/em}$: 450/510 nm); (3) $F_{1,dark}$ ($\lambda_{ex/em}$: 405/510 nm, camera shutter closed); (4) $F_{1,light}$ ($\lambda_{ex/em}$: 405/510 nm). Integration time was 10 s. For each excitation wavelength, the respective dark images with background noise were subtracted from images of fluorescence (i.e. $F_1 = F_{1,light} - F_{1,dark}$ and $F_2 = F_{2,light} - F_{2,dark}$). The ratiometric pH response ($R = F_1/F_2$) of the sensor was determined as the fluorescence ratio between F_1 ($\lambda_{ex/em}$: 405/510 nm) and F_2 ($\lambda_{ex/em}$: 450/510 nm) in each effective pixel after dark image correction.

Image analysis was performed using Matlab 6.5. By the time-correlated calibration procedure, obtained fluorescence ratio of images could be evaluated using a response function unique for each pixel, individually determined at the time of detection [12]. The pH in each pixel was median filtered (3 × 3 pixels) to remove salt and pepper noise while still preserving the edge response. Quiver plots were generated by the gradient (extracting partial derivatives) and quiver (vectorizing) functions in Matlab [2]. The partial derivatives were used to calculate the magnitude (M) of the gradient in each pixel ($M = [\delta x^2 + \delta y^2]^{1/2}$).

2.7. Analytical performance

For quality control and to compare between the time-correlated and more conventional calibration protocols, two different approaches were used to quantify the spatial and temporal precision of measurements. In the first approach, the spatial precision in a pixel was defined as the standard deviation (S.D.) of measurements in the 3 × 3 neighbouring group of pixels. This approach was motivated by the fact that pixel values have been extracted by median filtration (3 × 3 pixels), and that pixels do not have discrete optical pathways. The latter implies potential scattering of light within the sensor and divergence of light between the sensor and the optical set-up. Preliminary experiments with this particular optical system have shown that about 30% of the signal detected in a pixel can also be detected in the neighbouring pixels (data not shown). In the second approach, the temporal precision in a pixel was defined as the S.D. of the pixel response from six images acquired consecutively at the end of experiments (day 17). It was assumed that sensor response after about 17 days of experiments would provide the most unfavorable analytical precision throughout the experimental period.

To further evaluate sensor performance and to distinguish between systematic errors and bivalve activities, images captured during mornings and evenings were analyzed in blocks of 5 × 5 pixels (as in the quiver plots). Statistical significance related to an integrated pH response was thereby increased at the expense of

Please cite this article in press as: A. Hakonen, et al., Talanta (2010), doi:10.1016/j.talanta.2010.02.041

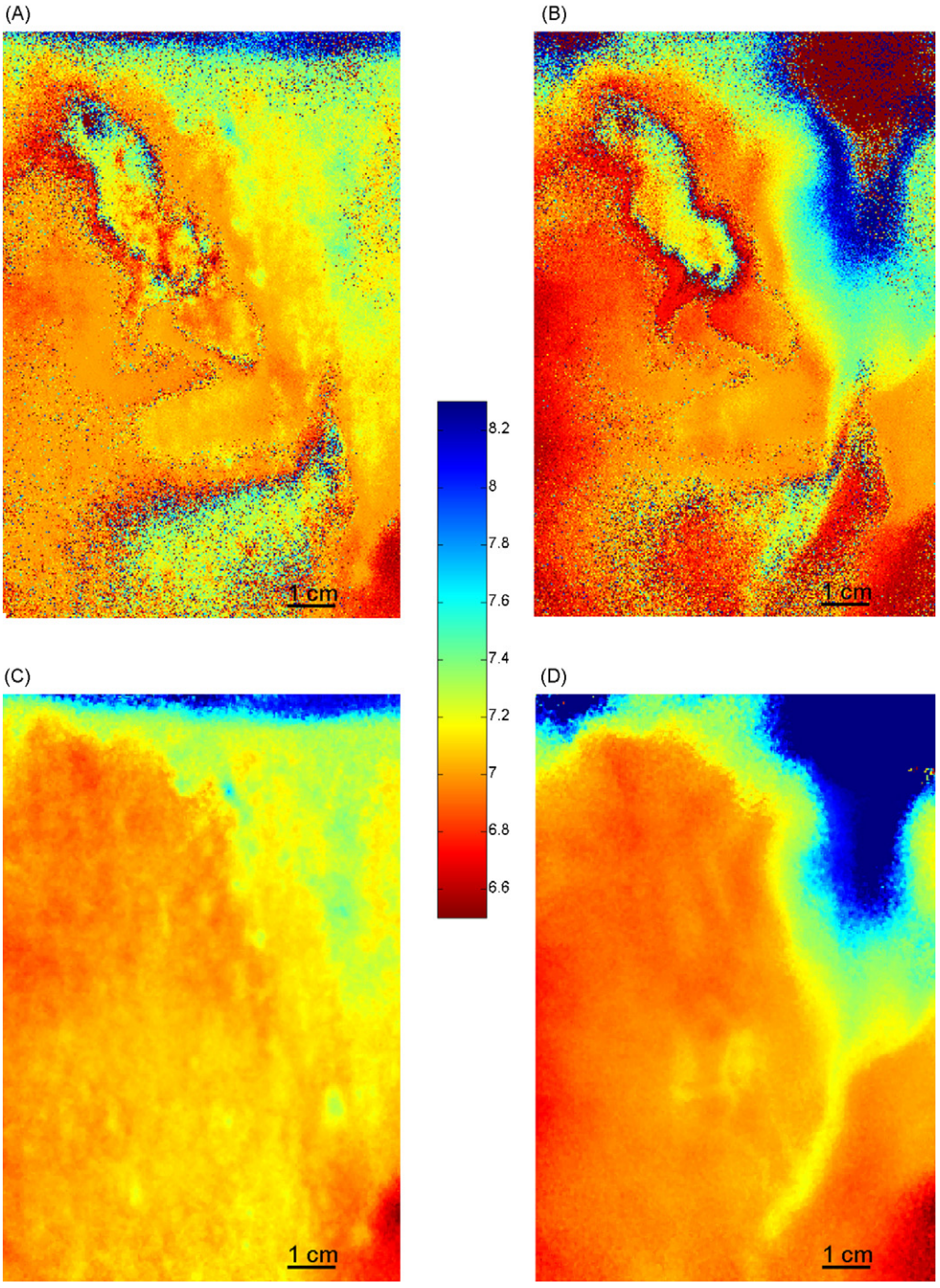

Fig. 2. Distribution of pH illustrated by ratiometric images without (A and B) and with (C and D) the time-correlated calibration protocol, here exemplified after 76 h (A and C) and 406 h (B and D) of experiment. Images A and B revealed areas of salt and pepper noise, while fine structures became evident after the normalization protocol (C and D). The colorbar displays pH values.

spatial resolution. Each group of blocked pixels for analysis corresponded to an area <2 mm^2.

3. Results and discussion

3.1. Calibration assessment and analytical performance

Analytical developments to normalize fluorescence response and to compensate for signal drift over time include ratiometric sensing schemes coupled to time-correlated calibration procedures [12]. A comparison of ratiometric images with and without the time-correlated calibration protocol indicated that uncorrected images have large areas of seemingly noisy response patterns (Fig. 2A and B), while even fine structures became evident after the normalization protocol was applied to images (e.g. Fig. 2D).

Overall, sensitivity and precision were reduced in regions with high pH (~8) due to the apparent pK_a (pK_a') of immobilized HPTS, $pK_a' \approx 6.4$ [3]. The dynamic range of optical sensors is normally considered to cover a pH range of $pK_a' \pm 1$ pH units [34]. Accordingly, imaging pH sensors based on HPTS (immobilized as in this study) have a theoretical maximum performance within the interval $5.4 \leq pH \leq 7.4$. Although pH of many subsurface marine

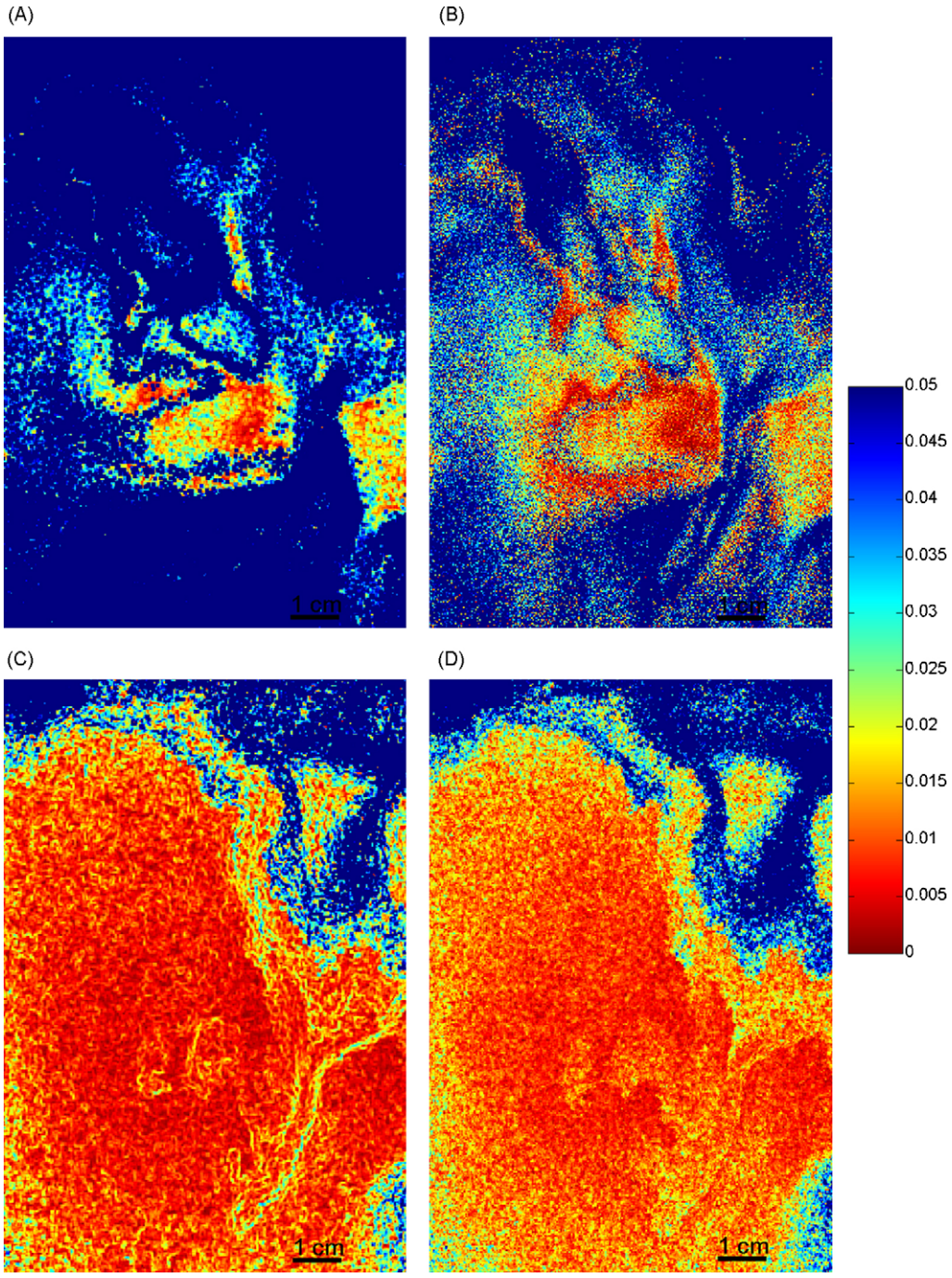

Fig. 3. Quantitative image of the analytical performance at the end of experiments (day 17) illustrated as the spatial (A and C, 3 × 3 group of pixels) and temporal (B and D, six consecutive images) precision of measurements (S.D.) in each pixel. Images A and B were evaluated using pre-sample calibration, while time-correlated protocols were applied to C and D. The colorbar displays S.D. of measurements (pH units).

sediments is ~7 [3,4], this range is somewhat below the pH often found in other marine systems [35]. However, optimal range of sensor performance is determined by how well low concentrations of indicator species can be detected [3]. For example, the dynamic range would cover 4 pH units ($pK_a' \pm 2$ pH units) if either of the two species in the indicator acid/base conjugate pair of HPTS could be measured at a relative concentration of 1%. Using modern optical technology, this is normally readily achieved. Further, from an analytical perspective it often is more appropriate to discuss analytical performance in a quantitative manner, for example in relation to a preset precision of measurements. The HPTS analogue, 6,8-dihydroxypyrene-1,3-disulfonic acid (DHPDS), was recently immobilized in a sensor membrane for high-performance (e.g. precision 0.0057 pH units) measurements of pH between pH 6 and 9 [36]. This pH dye demonstrated a log-linear relationship with pH over 5 pH units. DHPDS may thus provide an interesting alternative to HPTS for pH measurements in marine environments, including pH distributions in sediments with a large range in pH.

The spatial precision of measurements was utilized to compare the analytical performance of the pH sensor throughout the experiment (all images), applying conventional calibration (pre-sample) and time-correlated-calibration protocols. During the first 10 days of experiment, >98% of pixels were associated with a precision better than 0.05 pH units using the time-correlated calibration pro-

Please cite this article in press as: A. Hakonen, et al., Talanta (2010), doi:10.1016/j.talanta.2010.02.041

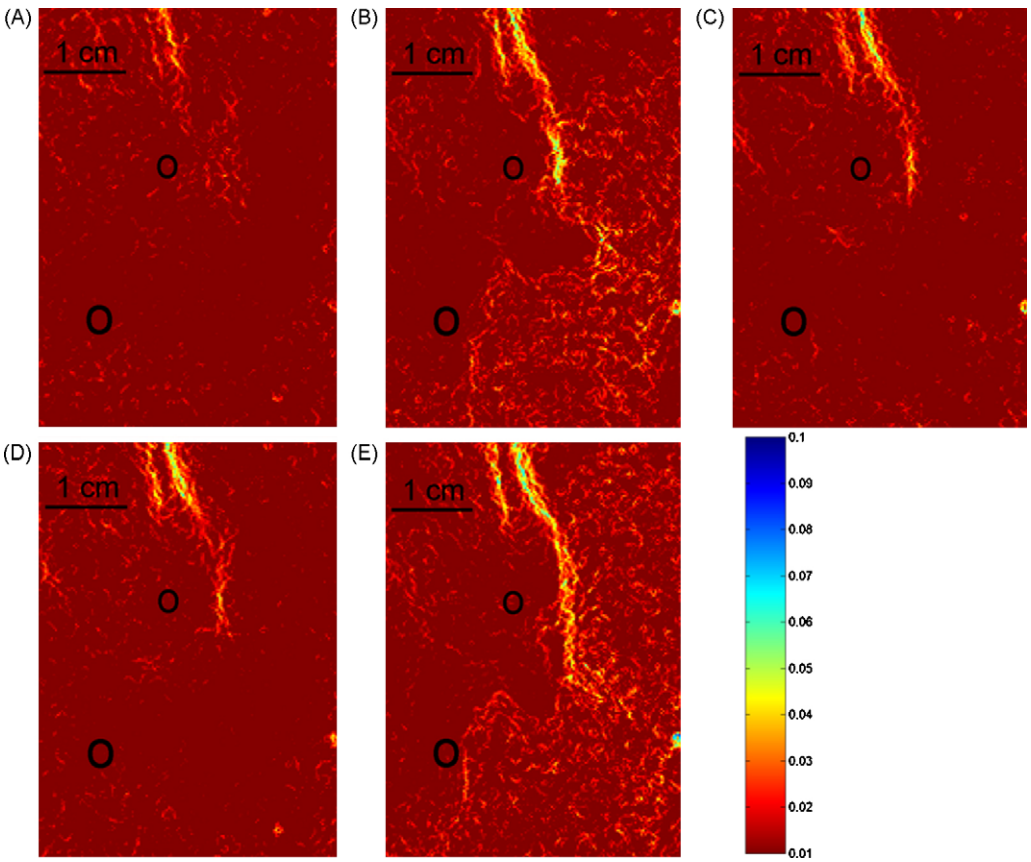

Fig. 4. Images of pH gradients ($[\delta x^2 + \delta y^2]^{1/2}$) in each pixel. Images were captured at: (A) 20:02 day 9, (B) 10:22 day 10, (C) 14:26 day 10, (D) 16:51 day 10 and (E) 10:10 day 11. Black rings were inserted to illustrate end-locations of the bivalves. The color bar denotes pH units per pixel.

cedure. In contrast, this precision was ascribed to only 30–40% of pixels using pre-sample calibration protocols. At the end of experiments (day 17), the spatial precision for 89% of pixels was better than 0.05 pH units using the time-correlated calibration procedure (Fig. 3), while only 24% of pixels were associated with a precision better than 0.05 pH units using the more conventional calibration protocol (Fig. 3A).

Six images were taken before and after the sediment was X-rayed at the end of experiments ($n_{tot} = 12$; day 17). The temporal precision of measurements was similar for the two sets of images. More than 87% of the pixels were associated with a temporal precision better than 0.05 pH units using the time-correlated calibration (Fig. 3D). For comparison, the precision was better than 0.05 pH units for ~47% of the pixels using conventional calibrations (Fig. 3B). Our study therefore demonstrated and confirmed previous studies by [12] that significantly more pixels in the final pH image were associated with high precision (S.D. < 0.05) when sensor response was evaluated using time-correlated calibrations compared to more conventional pre-calibration protocols. Average S.D. for both the spatial and the temporal precision (overall S.D. < 0.05) were constant using time-correlated (0.01 pH units) and pre-sample (0.03 pH units) calibration procedures, respectively. Using the time-correlated calibration procedure, an additional 46–73% pixels were associated with a precision (S.D.) better than 0.05 pH units.

For future imaging studies the sigmoidal and log-linear approach for time dependent calibrations are highly interesting [8,36]. Also, involvement of nanoparticles or nanostructures for signal enhancement and increased photo-stability provides a performance increasing and drift minimizing tool, recent examples are [37–39].

3.2. Systematic errors or diurnal variations in bivalve activities?

The variation in response for images taken at ~8:00 compared ~20:00 demonstrated differences related to the time of measurement in regions used to evaluate system background (close to the edges of the sensor). The observed time-dependent systematic drift in system response could be a consequence from switching the instrument on and off, affecting the light intensity of the light source and possibly the temperature within the experimental box. Artifacts associated with changes in excitation light intensities are normally cancelled out by the ratiometric procedure [16]. However, time-dependent changes in the spectral properties of the excitation lamp may not be cancelled by the ratiometric procedure. A shift in fluorescence partitioning due to potential fluctuations in temperature would also change the observed sensor response in a methodical way. The quantitative importance of these effects was, however, not individually evaluated. Assuming that this systematic change in pH (δpH/δt) reflects the maximum "background" contribution from system fluctuations to the measured sensor response, the sensor drift was 0.0025 ± 0.0003 pH units h^{-1} ($n = 90$; 5×5 blocks). This systematic drift caused the measured pH to increase during the day and decrease during the night.

To further illustrate and localize small-scale temporal and spatial variations in sensor response, the pH gradient in each pixel was calculated (Fig. 4). The gradients revealed fine structures in the sediment down to single pixel resolution, with an overall structure similar to naturally occurring pore water and distribution patterns created by the bivalves. The latter were at the end of experiment confirmed by the X-radiograph (Fig. 5). In addition to a temporal variability in the systematic error of sensor response, imaging of pH gradients in each pixel suggested time-dependent patterns

Please cite this article in press as: A. Hakonen, et al., Talanta (2010), doi:10.1016/j.talanta.2010.02.041

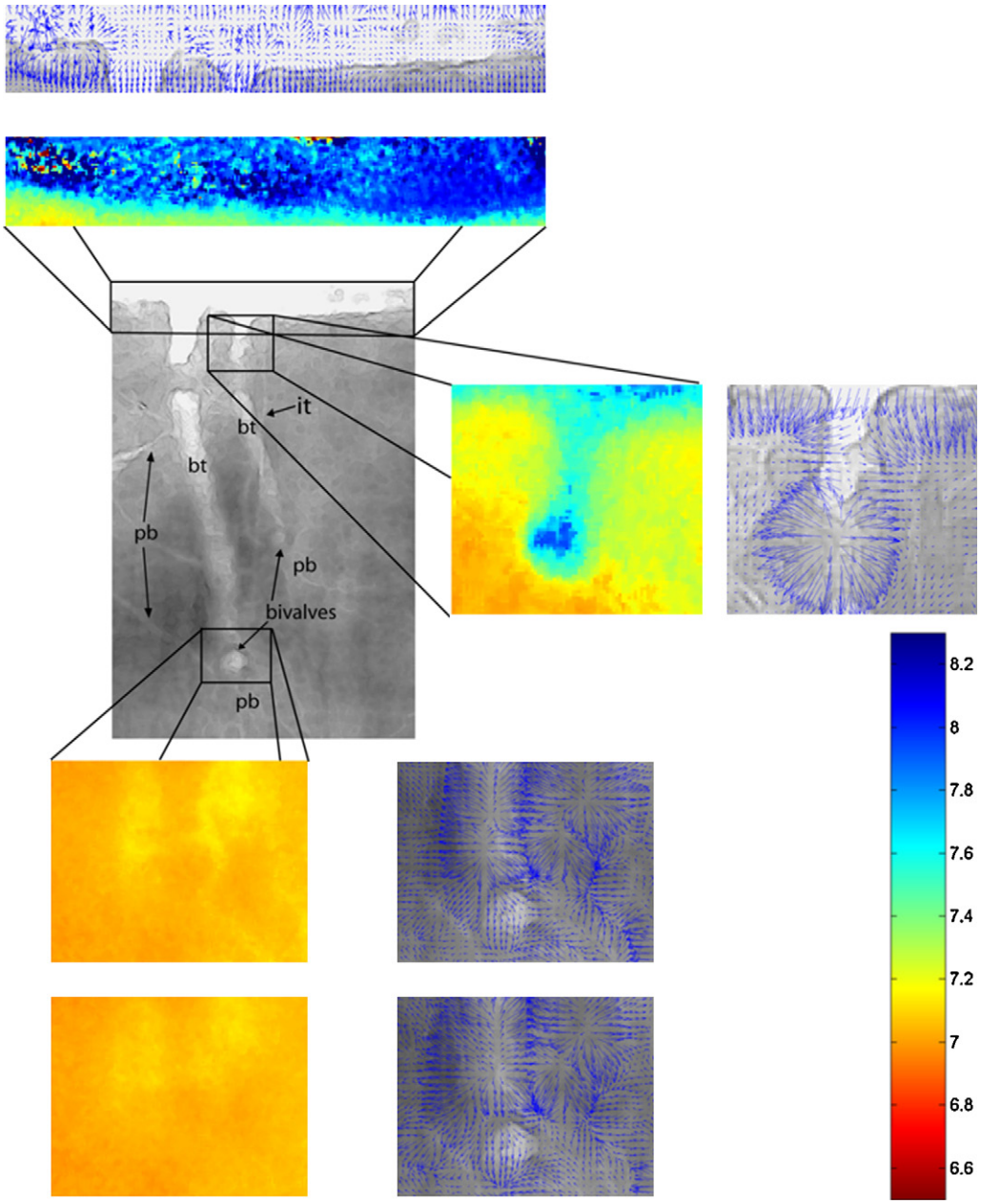

Fig. 5. The large image in the center represents an X-radiograph of the aquarium at the end of the experiment. The final position of the bivalves, their burrowing tracts (bt), inhalent tubes (it), and pedal burrowing tracts (pb) are indicated. *Above radiograph*. A close-up of the sediment surface at the beginning of experiments. *Beside radiograph*. The initial burrowing tract of a bivalve. *Below radiograph*. The sediment surrounding a bivalve just before (upper panels) and after (lower panels) X-rays were taken. Quiver plots (Matlab 6.5) highlight the strong pH gradients associated with imaging of pH distributions in sediments bioturbated by *T. sarsi*.

in activities by the thyasirids (Fig. 4). The pH gradients were progressively more developed (magnitude and spatial extension) in all images captured in the morning compared to those obtained in the afternoon and evening.

3.3. General patterns during imaging of pH

The pH imaging sensor qualitatively and quantitatively demonstrated temporal and spatial patterns of pH distributions in the overlying water and sediment matrix during the experiment. Overall, pH of the overlying water was higher than that of the underlying sediment, with a concentration gradient depending on the time of experiment. At the beginning of experiment, there was a distinct drop in pH (from 8.2 to 7.3; Fig. 2C) immediately below the sediment-water interface, likely associated with aerobic mineralization of organic material and the re-oxidation of products resulting from anaerobic respiration diffusing from below. While there were regions with more or less constant pH, primarily in deeper sediment layers not initially exposed to macrofaunal reworking, the imaging sensor clearly revealed small and large-scale variations in pH which would normally be obscured by principles of spatial averaging over finite depth intervals (e.g. by pH electrodes). For example, the distinct drop in pH at the sediment surface was associated with gradients of up to 1 pH unit over a distance of less than 5 mm.

The overall pH decrease with time of experiment is likely due to a combined effect from enhanced aerobic organic matter mineralization and induced re-oxidation of reaction products caused by macrofaunal activities, as well as a release of H^+ as a consequence from the reoxidation of symbiotic metabolites. The pH decrease

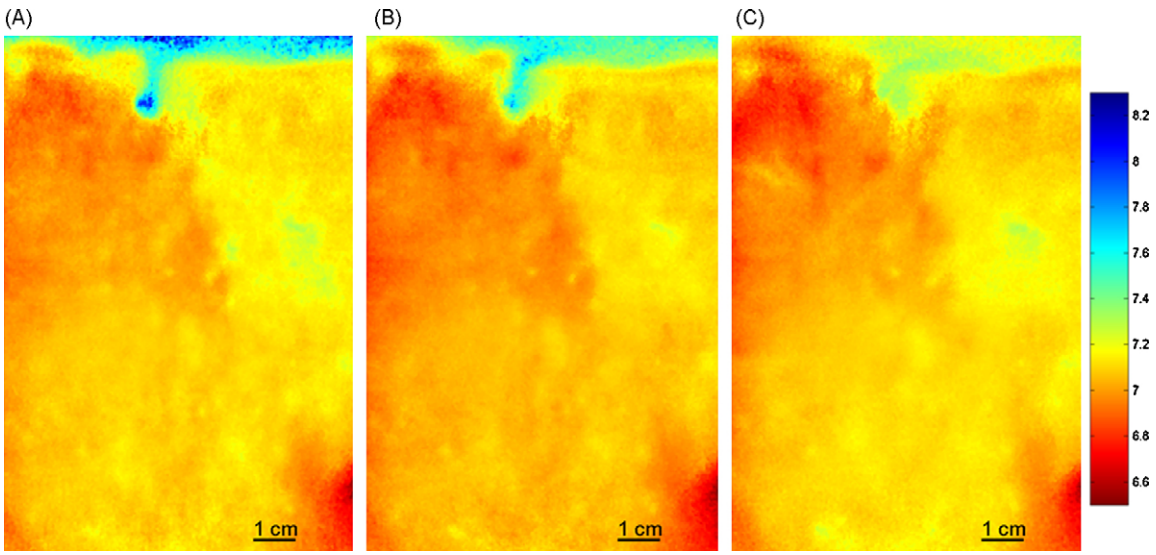

Fig. 6. The images display the acidification of overlying water during the initial period of burrowing by the bivalves. Images of pH are shown after 92 h (A), 100 h (B) and 116 h (C) of experiment. During this period, the pH of the overlying water dropped from >8 to 7.2 despite a continuous flow of seawater to the microcosm. The decrease in pH was likely attributed to pore water irrigation by *T. sarsi* that supplied reduced and acidic compounds through the exhalent tube to the overlying water.

was first observed and was most pronounced in the overlying water (Fig. 6). Initial pH values in the overlying water was consistent with open ocean conditions (~8.2), but relatively quickly decreased, reaching a pH of ~7 on day 4, and remained more or less constant through day 10. It therefore appeared as the flow of incoming bottom water was insufficient to completely maintain biogeochemical characteristics (i.e. pH) of the overlying water. However, although dissolved oxygen was not directly measured, the frequent visual inspections of the microcosm in general, and the surface sediment in particular, confirmed a well-oxygenated bottom water and sediment surface. Further, considering the alkalinity ($A_T \sim 2350$ μM) and general buffer capacity of the bottom water, the sediment supply of H^+ must have been significant to cause the pH change observed in the overlying water. Preliminary results from follow-up experiments using oxygen and pH electrodes positioned immediately above the opening of the exhalent tube of *T. sarsi* have confirmed a strongly reduced and acidic exhalent stream that may, at least locally, drastically affect pH of bottom waters (data not shown).

On day 17, a tongue of high pH values was observed to extend from the sediment surface into the sediment on the right-hand side of the aquarium close to the region where the inflow of oxygenated bottom water was directed (Figs. 1 and 2D). Although burrowing and irrigation by the thyasirids cannot be completely excluded, the X-ray image integrating faunal activities does not support extensive and large-scale bioturbation patterns directly associated with this progressive evolution of pH (Fig. 5). Alternatively, extensive and more long-term reworking of particles by the highly extensible foot of this small bivalve may have contributed to a partial disruption of the sediment structure and thereby increased the permeability of the sieved sediment. As an indirect consequence from *T. sarsi* bioturbation activities by the extensible foot, overlying water could progressively passively penetrate relatively deep into the sediment immediately below the tube that supplied oxygenated replacement water.

3.4. Changes in pH due to activities by T. sarsi

With time, the bivalves created burrows around which pH changed dramatically compared to the adjacent sediment (Fig. 5 and 6A). From visual observations, the bivalves had burrowed into the sediment ~3 h after their introduction into the aquarium. About 16 h after the addition of animals (i.e. the following morning) there was clear evidence of a burrowing tract (Figs. 5 and 6A). This cavity is the beginning of a pathway from the sediment surface to the final position of the bivalve in the sediment, with the remainder of the tract being consecutively refilled with sediment. This tract should be of no use to the burrowed animal, as it is known to construct an inhalent tube with its foot for ventilation purposes and for direct contact with the overlying water.

The pH within the burrowing tract at the beginning of the experiment was >8.0, i.e. significantly higher than that of the surrounding sediment (pH 7.0–7.5) and more similar to the pH of the overlying water (Figs. 5 and 6A). Later in the experiment, when the burrowing tracts were refilled, the pH within them was lower than the surrounding sediment (6.90 compared to 7.05; Fig. 2D). Lower pH values in relict formations confirm observations by Zhu et al. [25]. These authors reported increased concentrations of CO_2 in relict burrow structures by the polychaete *Nephtys incisa*, a consequence suggested related to the local injection of reactive substrate (e.g. mucus) and energetically favorable oxidants (Mn- and Fe-oxides) formed within the burrow walls. Alternatively, the burrowing tracts may in our study have constituted pathways for the bivalve to eject water of low pH (including symbiotic metabolites) to the overlying water. In addition to lower pH measured in the relict burrow, the latter assumption was strongly supported by the drastic pH decrease in the overlying water after addition of the bivalves (Fig. 6). Significant pH gradients close to the burrows of *T. sarsi* were confirmed by Quiver plots (Matlab 6.5). The strongest gradients were observed immediately adjacent to the burrowing tracts, inhalant tube and pedal tracts (Fig. 5). For example, during the initial burrowing of one of the bivalves, gradients of up to 1.16 pH units per mm (0.32 units per pixel) were observed (burrowing tract in Fig. 6 A). In contrast to the lower pH in burrowing tracts, pedal tracts demonstrated higher pH than the surrounding sediment (Fig. 2D). Interestingly, at the end of experiments the narrow pedal tracts seemed to be directed towards the region where inflow of overlying water likely penetrated the sediment (Fig. 2D). This pattern may indicate an intentional pathway whereby the bivalve could actively reach oxygenated bottom water, possibly containing soluble sulfides (e.g. thiosulfate and acid volatile sulfides) in addition to other oxidants such as nitrate.

Please cite this article in press as: A. Hakonen, et al., Talanta (2010), doi:10.1016/j.talanta.2010.02.041

4. Conclusions

Utilizing time-correlated pixel-by-pixel calibration protocols during imaging, close to 90% of the pixels were associated with a precision (S.D.) of <0.05 pH units at the end of an experimental period of 17 days. Average S.D. for both the spatial and the temporal precision (overall S.D. < 0.05) were constant using time-correlated (0.01 pH units) and pre-sample (0.03 pH units) calibration procedures, respectively. Using the time-correlated calibration procedure, an additional 46–73% of pixels were associated with a precision (S.D.) better than 0.05 pH units. Strong pH gradients were demonstrated not only across the sediment-water interface but also associated with bioturbation activities immediately adjacent to *T. sarsi* burrowing tracts, inhalant tubes and pedal tracts in the sediment matrix. Gradients of up to 1.16 pH units per mm were observed.

Acknowledgements

Financial support was obtained by the Swedish Research Council (VR), the Foundation for Strategic Environmental Research (MISTRA), the Swedish Research Council for Environment, Agricultural Sciences and Spatial Planning (FORMAS), the Royal Swedish Academy of Sciences, and the Swedish Marine Research Centre (GMF). E. Väänänen provided technical support. R. Rosenberg and K. Norling assisted during field sampling.

References

[1] R.N. Glud, N.B. Ramsing, J.K. Gundersen, I. Klimant, Marine Ecology-Progress Series 140 (1996) 217–226.
[2] N. Stromberg, Environmental Science & Technology 42 (2008) 1630–1637.
[3] S. Hulth, R.C. Aller, P. Engstrom, E. Selander, Limnology and Oceanography 47 (2002) 212–220.
[4] Q.Z. Zhu, R.C. Aller, Y.Z. Fan, Environmental Science & Technology 39 (2005) 8906–8911.
[5] J.I. Peterson, S.R. Goldstein, R.V. Fitzgerald, D.K. Buckhold, Analytical Chemistry 52 (1980) 864–869.
[6] N. Stromberg, E. Mattsson, A. Hakonen, Analytica Chimica Acta 636 (2009) 89–94.
[7] C. McDonagh, C.S. Burke, B.D. MacCraith, Chemical Reviews 108 (2008) 400–422.
[8] A. Hakonen, S. Hulth, Analytica Chimica Acta 606 (2008) 63–71.
[9] P.C.A. Jeronimo, A.N. Araujo, M. Montenegro, Talanta 72 (2007) 13–27.
[10] D.A. Nivens, M.V. Schiza, S.M. Angel, Talanta 58 (2002) 543–550.
[11] D. Wencel, B.D. MacCraith, C. McDonagh, Sensors and Actuators B-Chemical 139 (2009) 208–213.
[12] N. Stromberg, S. Hulth, Analytica Chimica Acta 550 (2005) 61–68.
[13] R.B. Thompson, J.R. Lakowicz, Analytical Chemistry 65 (1993) 853–856.
[14] R.Y. Tsien, M. Poenie, Trends In Biochemical Sciences 11 (1986) 450–455.
[15] H. Hochreiner, I. Sanchez-Barragan, J.M. Costa-Fernandez, A. Sanz-Medel, Talanta 66 (2005) 611–618.
[16] Z. Zhujun, W.R. Seitz, Analytica Chimica Acta 160 (1984) 47–55.
[17] N. Stromberg, S. Hulth, Sensors and Actuators B-Chemical 90 (2003) 308–318.
[18] H. Stahl, A. Glud, C.R. Schroder, I. Klimant, A. Tengberg, R.N. Glud, Limnology and Oceanography-Methods 4 (2006) 336–345.
[19] N. Stromberg, S. Hulth, Sensors and Actuators B-Chemical 115 (2006) 263–269.
[20] R.J. Diaz, R. Rosenberg, Science 321 (2008) 926–929.
[21] R. Vaquer-Sunyer, C.M. Duarte, Proceedings of the National Academy of Sciences of the United States of America 105 (2008) 15452–15457.
[22] S.C. Dufour, H. Felbeck, Marine Ecology-Progress Series 320 (2006) 185–194.
[23] P.R. Dando, A.J. Southward, E.C. Southward, Marine Ecology-Progress Series 280 (2004) 181–187.
[24] S.C. Dufour, H. Felbeck, Nature 426 (2003) 65–67.
[25] Q.Z. Zhu, R.C. Aller, Y.Z. Fan, Marine Chemistry 101 (2006) 40–53.
[26] S. Hulth, R.C. Aller, F. Gilbert, Geochimica Et Cosmochimica Acta 63 (1999) 49–66.
[27] K. Soetaert, A.F. Hofmann, J.J. Middelburg, F.J.R. Meysman, J. Greenwood, Marine Chemistry 106 (2007) 380–401.
[28] K. Caldeira, M.E. Wickett, Nature 425 (2003) 365–1365.
[29] S. Widdicombe, S.L. Dashfield, C.L. McNeill, H.R. Needham, A. Beesley, A. McEvoy, S. Oxnevad, K.R. Clarke, J.A. Berge, Marine Ecology-Progress Series 379 (2009) 59–75.
[30] Q.Z. Zhu, R.C. Aller, Y.Z. Fan, Geochimica Et Cosmochimica Acta 70 (2006) 4933–4949.
[31] L. Arneborg, Continental Shelf Research 24 (2004) 443–460.
[32] O. Lindahl, A. Belgrano, L. Davidsson, B. Hernroth, Ices Journal of Marine Science 55 (1998) 723–729.
[33] P. Engstrom, T. Dalsgaard, S. Hulth, R.C. Aller, Geochimica Et Cosmochimica Acta 69 (2005) 2057–2065.
[34] A. Jang, J.H. Lee, P.R. Bhadri, S.A. Kumar, W. Timmons, F.R. Beyette, I. Papautsky, P.L. Bishop, Environmental Science & Technology 39 (2005) 6191–6197.
[35] I. Hansson, Deep-Sea Research 20 (1973) 479–491.
[36] A. Hakonen, S. Hulth, Talanta 80 (2010) 1964–1969.
[37] C. Maule, H. Gonçalves, C. Mendonça, P. Sampaio, J.C.G. Esteves da Silva and P. Jorge, Talanta 80, 1932–1938.
[38] C. McDonagh, O. Stranik, R. Nooney, B.D. MacCraith, Nanomedicine 4 (2009) 645–656.
[39] A. Hakonen, Analytical Chemistry 81 (2009) 4555–4559.

Please cite this article in press as: A. Hakonen, et al., Talanta (2010), doi:10.1016/j.talanta.2010.02.041

Paper II

ANALYTICA CHIMICA ACTA 606 (2008) 63–71

available at www.sciencedirect.com

ScienceDirect

journal homepage: www.elsevier.com/locate/aca

A high-precision ratiometric fluorosensor for pH: Implementing time-dependent non-linear calibration protocols for drift compensation

Aron Hakonen, Stefan Hulth*

Department of Chemistry, GöteborgUniversity, SE-412 96 Göteborg, Sweden

ARTICLE INFO

Article history:
Received 10 August 2007
Received in revised form
12 October 2007
Accepted 20 October 2007
Published on line 26 October 2007

Keywords:
pH
Optode
8-hydroxypyrene-1,3,6-trisulfonic acid
Photoacidity
Non-linear calibration
Signal drift
Fluorescence ratio

ABSTRACT

We present a versatile time-dependent non-linear calibration protocol for optical sensors, implemented on the pH sensitive ratiometric fluorophore 8-hydroxypyrene-1,3,6-trisulfonic acid (HPTS) immobilized in ethyl-cellulose. The calibration protocol individually compensated for the progressive drift of calibration parameters, whereby sensor precision and accuracy, as well as applicable lifetime were improved. A severely reduced photoacidity was observed for the immobilized fluorophore, for which excited state dynamics was characterized and benefited from during measurements. Due to the significantly reduced photoacidity of HPTS immobilized in the ethyl-cellulose sensing membrane, a dual excitation/dual emission (F_1, ex/em: 405/440 nm and F_2, ex/em: 465/510 nm) ratiometric ($R_{F_1,F_2} = F_1/F_2$) sensing scheme could be used to amplify sensor response. The signal to noise (S/N) ratio was enhanced by ~400% utilizing the dual excitation/dual emission ratiometric sensing scheme, rather than the more commonly used protocol of dual excitation/single emission for HPTS fluorescence. Apparent pK_a of the fluorophore ranged from 6.74 to 8.50, mainly determined by the immobilization procedure. The repeatability (IUPAC, pooled standard deviation) over three pH values (6.986, 7.702 and 7.828) was 0.0044 pH units for the optical sensor, compared to 0.0046 for the electrode used for standardization. Sensor analytical characteristics were thereby in principle limited by the performance of the standardization procedure.

1. Introduction

The activity of hydrogen ions (pH) is a key analytical parameter reflecting the thermodynamic state of acid-base processes and overall balances between multiple reactions. In 1980, Peterson et al. [1] developed the first optical sensor (optode) for pH measurements utilizing absorbance of the indicator dye phenol red. Shortly after, the first fluorescence-based pH-optode was described [2]. Up to date, numerous optodes have been developed for pH-measurements, realizing a variety of immobilization and spectroscopic techniques [3–15]. Overall, optodes have many appealing features, of which no need for a reference signal is perhaps the most advantageous. Further, optodes are normally not sensitive to electrical interferences and are comparably easy to miniaturize, e.g. for in-vivo measurements [16–18]. Optodes are also suitable for high-resolution imaging of solute distributions in complex environments such as aquatic sediments [6], and there are exciting possibilities for multi-parameter and multi-analyte sensing [19–21]. Important drawbacks of most optical sensors include an inherent sensitivity to changes in ionic strength of the sample matrix [22]. They are also influenced by variations

* *Corresponding author*. Tel.: +46 31 772 2878; fax: +46 31 772 2785.
E-mail address: hakonen@chem.gu.se (A. Hakonen).
0003-2670/$ – see front matter © 2007 Elsevier B.V. All rights reserved.
doi:10.1016/j.aca.2007.10.035

in excitation light intensity, and often have a limited long-term stability due to leaching and photobleaching of the indicator dye [23–25]. In fact, optical sensors are commonly susceptible to a drift in sensor response, a phenomenon only rarely fully compensated for by appropriate analytical protocols.

There are, however, several spectroscopic techniques and analytical calibration protocols designed to normalize for signal drift and a sensor response not associated with changes in analyte activity. Such procedures include time and frequency-domain fluorescence lifetime measurements. Lifetime-based sensing schemes often demonstrate a significantly reduced susceptibility for intensity and wavelength dependent interferences [11,13]. Though lifetime-based sensing of fluorescence provides an analytical tool versatile for many applications, direct investigations on the quantitative importance and analytical character of drift during lifetime measurements are to the best of our knowledge missing. In addition, fluorescence lifetime measurements are usually associated with complex and costly instrumentation.

Ratiometric normalization schemes provide an alternative technique to time and frequency-domain fluorescence lifetime measurements. During the last few decades, ratiometric probes and ratiometric normalization schemes, more recently including time-domain dual lifetime referencing (t-DLR) [13], have frequently been used to reduce artifacts during reversible fluorescence detection [3,23]. Ratiometric procedures are feasible when the solute specific fluorescent probe induces a spectral shift in response to changes in analyte concentrations [3]. Preferably, changes in analyte concentrations are associated with signal amplification during the ratiometric protocol, i.e., the individual fluorescence signals are anti-correlated [25]. Reversible ratiometric probes have up to recently been in diminutive supply, but lately ratiometric probes have been developed for several ions e.g., Zn^{2+}, Mg^{2+}, F^{-}, PO_4^{3-} and molecular oxygen [26–30]. Until the study by Kurihara et al. [31], ratiometric analytical schemes were only applied on solute specific probes with intrinsic ratiometric properties. However, implementing ionophores as analyte carriers in conjunction with solvent (or polarity) sensitive fluorescent dyes that exhibit a spectral shift upon change of environment, has realized ratiometric sensing schemes for a progressively increasing number of solutes. Examples for which ionophores and principles of coextraction have been utilized for ratiometric solute detection include Na^{+} and NH_4^{+} [31,32]. The ratiometric normalization procedure is normally assumed to remove artifacts that induce a sensor response not related to changes in analyte concentrations, e.g., variations in ambient and excitation light intensities, uneven dye concentration, photobleaching and wash-out of the indicator dye [23]. However, there are at present only few investigations that have qualitatively and quantitatively evaluated the efficiency of the ratiometric approach. For example, Stromberg and Hulth [25] demonstrated that variations in excitation light intensity (10–100% incident light) were found more or less completely eliminated by a ratiometric sensing scheme. It was, however, not possible to compensate for artifacts associated with fluctuations in temperature, effective probe concentration, and sample ionic strength.

Analytical improvements to normalize and control signal drift over time have encompassed a ratiometric sensing scheme coupled to a time-correlated calibration procedure [33,34]. The main objective of this study was to further evolve the time-correlated ratiometric calibration procedure to also include non-linear parameterization for quantification. To apply this we also developed a fluorescence-based ratiometric pH sensor that is straightforward and quick to manufacture for high-precision detection of pH.

2. Experimental

2.1. Materials

To prepare the sensor layer the ratiometric fluorophore 8-hydroxypyrene-1,3,6-trisulfonic acid (HPTS; 2.0 mg of the tri-sodium salt; n_{HPTS} = 3.70 μmol, >97%, Sigma–Aldrich) was dissolved in tetraoctylammonium (TOA^{+}) hydroxide solution (200 μL of 10% TOA^{+} in methanol, n_{TOA+} = 33.3 μmol, Purum, Fluka) and diluted with ethanol (800 μL, 99.5%, Kemetyl AB). Ethyl-cellulose solution was prepared by dissolving 200 mg ethyl-cellulose (48% ethoxyl content, Sigma–Aldrich) in an ethanol (1400 μL, 99.5%, Kemetyl AB)/toluene (2000 μL, HPLC grade, Fisons Scientific Equipment) mixture. The sensor cocktail was finalized by mixing 320 μL HPTS solution with 680 μL cellulose solution. The cocktail was spin-coated on a ∼100 μm thick transparent plastic film (Brilliant transparency film, Art. no. 901121). Deionized water utilized for buffers was further purified by a Milli-Q system (Millipore Corp.) to a resistivity of >18 MΩ cm^{-1}. Phosphate buffers were prepared from Milli-Q and H_3PO_4 (85%, J.T. Baker), where pH and ionic strength were adjusted by appropriate additions of NaOH (p.a., Merck) and NaCl (p.a., Merck).

2.2. Instrumentation

Spin-coating of the sensor cocktail was performed by a spin-coating device made in-house, resulting in a sensing layer thickness of ∼10 μm. The final thickness was verified by fluorescence microscopy (Leica Microsystems DMI 6000B). The sensor was mounted onto a plexiglass support and secured in a specially designed flow-through plastic cuvette (3 mL), placed in the spectroflourometer (Fluoromax-3, SPEX Instruments Int. Inc.). To minimize background noise and reflection from incident light, the angle of incidence for the excitation light was set to 60°. Matrix scans (excitation 300–480 nm, emission 430–550 nm) were performed at pH 6.25 and 9.20 to determine the optimal excitation/emission wavelength pairs for this pH interval. The ratiometric pH response (R_{F_1,F_2}) of the sensor was determined as the ratio between F_1 and F_2 (i.e., $R_{F_1,F_2} = F_1/F_2$). Matrix scans were performed at 1.00 nm resolution, 0.5 s integration time and 2.00 nm slit widths.

Working solutions for calibrations were prepared by mixing different ratios of two phosphate buffer solutions of pH 6.00 and 8.50 (ionic strength; I_{Tot} = 3.0 mM and $[PO_4^{3-}]_{Tot}$ = 1.95 mM). Mixing of the two buffers was performed on-line with an HPLC pump with multiple input solutions and mixing chambers. The mixed solution was pumped into the flow-through cuvette secured in the spectrofluorometer. The pH of the final solution was measured on-line with a pH-electrode (model 6.0232.100, 780 pH meter; Metrohm Ltd.),

calibrated by a one-point calibration procedure utilizing commercially available buffer solutions certified traceable to NIST Standard Reference Material (pH 7.00 Buffer, Thermo Orion). Temperature during all experiments was $20 \pm 1\,^{\circ}C$.

2.3. Procedures

Prior to experiments, the sensor film was rinsed for a few minutes in a solution with a composition similar to that of the samples. During experiments, solutions were allowed to equilibrate for ~7 min. Six ratios were measured per minute utilizing a flow rate of 10 mL min^{-1}, an integration time of 2 s, and slit widths of 2.00 nm. Measurements included two sets of calibrations made before and after the samples, respectively. The two sets of complete calibrations were linearly linked by a time-dependent calibration function. In this way, obtained fluorescence ratio of each sample could be evaluated using a unique response function, individually determined at the time of detection. Furthermore, calibrations were of different characteristics (e.g., pH values and number of data points) to emphasize the performance of the parametric sigmoidal calibration, and to increase the statistical significance of calibrations. Parameters for each calibration set were determined by minimizing the sum of squares of the errors between measured fluorescence ratios during sensor calibrations and calculated ratios from a four-parameter sigmoidal logistic function (Eq. (1)).

$$R_{F_1,F_2}(\mathrm{pH}) = \alpha_1 + \frac{\alpha_2 - \alpha_1}{1 + 10^{(\mathrm{pH}-\alpha_3)\alpha_4}} \quad (1)$$

where α_1 and α_2 are the asymptotic minimum and maximum of the sigmoidal function, respectively, α_3 is the apparent pK_{a4} of HPTS (i.e., the inflection point of the sigmoidal function), and α_4 is a constant that determines the slope of the function between α_1 and α_2. Hereafter, the apparent pK_{a4} of HPTS is referred to as pK_a.

Samples ($n = 14$) were executed by switching between three solutions: pH_1 6.985, pH_2 7.693 and pH_3 7.852 (average values determined on-line by the pH electrode). Overall performance of the ratiometric fluorosensor was evaluated according to IUPAC definition of the pooled standard deviation (P.S.D.) [35] of measurements at pH_1, pH_2 and pH_3. These pH values were selected on grounds of previous studies of HPTS in solution ($pK_a \sim 7.3$, 25 °C) [36] and immobilized in ethyl-cellulose ($pK_a \sim 8.4$, 25 °C) [5]. We would thereby predict sample pH close to the inflection point of the calibration function, as well as at pH values approaching the lowest ratio (α_1) of the calibration function.

In this study, we have utilized and compared three basic models for quantification of pH – (A) Piece-wise linear calibration: linear correction with time; (B) four-parameter sigmoidal calibration: linear correction of parameters with time; (C) four-parameter sigmoidal calibration: single calibration (i.e., no correction with time). Model A has previously been described and evaluated for a ratiometric ammonium sensor [33], where the calibration procedure was successfully used to predict analytical sensitivity, limit of detection, and signal variation throughout measurements.

Since HPTS fluorescence ratio follows a sigmoidal non-linear relation with pH [3], the models B and C were fit (least squares) to a four-parameter sigmoidal logistic function (Eq. (1)). In model B, the calibration made before the samples were linked in time to the calibration that followed the samples, supporting a time-dependent calibration function (Eq. (2)).

$$R_{F_1,F_2}(\mathrm{pH}, t) = \alpha_1(t) + \frac{\alpha_2(t) - \alpha_1(t)}{1 + 10^{(\mathrm{pH}-\mathrm{pK_a}(t))\alpha_4(t)}} \quad (2)$$

where each of the four time-dependent parameters varies according to (Eq. (3)):

$$\alpha_i(t) = \alpha_{i,\mathrm{Cal1}} + \frac{\alpha_{i,\mathrm{Cal1}} - \alpha_{i,\mathrm{Cal2}}}{\Delta t_{(\mathrm{Cal1,Cal2})}} t \quad (3)$$

As preceding experiments have indicated a linear characteristics of sensor drift (not shown), each of the four parameters was assumed to independently express a linear drift in time between the two calibrations. Each sample pH could thus be individually predicted from a time-dependent response function, ideally normalizing for drift in sensor response (Eq. (4)).

$$\mathrm{pH}(R_{F_1,F_2}, t) = \mathrm{pK_a}(t) + \frac{\log((\alpha_2(t) - \alpha_1(t)/R_{F1,F2} - \alpha_1(t)) - 1)}{\alpha_4(t)} \quad (4)$$

3. Results and discussion

3.1. General sensor characteristics

Fluorescence characteristics of HPTS in water ("free" HPTS) and immobilized on various supports have been evaluated in great detail (e.g. [3–7]). It was considered outside the scope of this study to particularly evaluate general fluorescent prop-

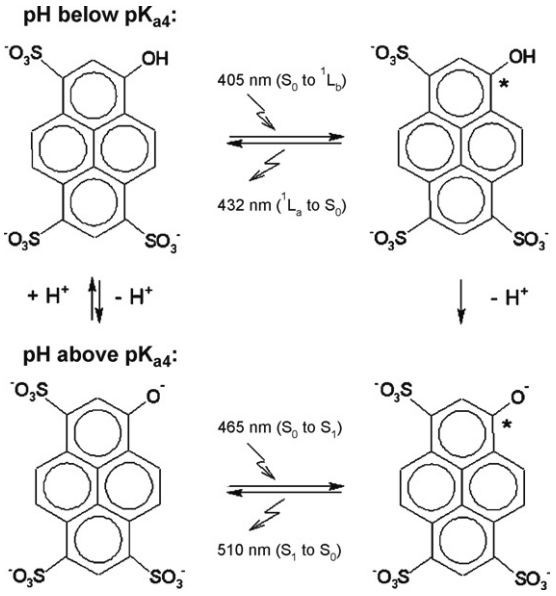

Fig. 1 – Molecular model and principles of fluorescence for the ratiometric pH indicator 8-hydroxypyrene-1,3,6-trisulfonate (HPTS).

erties of the sensor, e.g., quantum yield and photo-stability, but rather to recognize the drift in ratiometric response as a multi-linear process aimed to be normalized for. Experiments focused on flow-rate, temperature and illumination time have depicted leaching with a subsequent attenuation of dynamic quenching and photobleaching as the major linear components for sensor drift (not shown).

General properties of HPTS fluorescence (Fig. 1) and observed shift in fluorescence are essentially governed by the protonation/deprotonation equilibrium of the hydroxyl hydrogen and the photoacidity of HPTS. A severely reduced photoacidity was observed for the immobilized fluorophore, whereby excited state dynamics of HPTS was characterized and benefited from during measurements.

3.2. *Photoacidity of HPTS*

Several fluorescent compounds are photoacidic, i.e., the fluorophore is more acidic in its electronically excited state than in its ground state [37]. Typically, the pK_a of excited photoacidic compounds is 6–7 pH units lower than in the ground state [38], and for HPTS in deuterated water a pK_a of 0.0 has been demonstrated [39]. Mechanisms behind photoacidity have been investigated comprehensively (e.g. [38–46]), and although still not fully understood, a number of transition pathways have been proposed for HPTS [40–42]. Partly based on fluorescent properties demonstrated in this study, a schematic representation of excited state dynamics during excitation and relaxation of HPTS is provided (Fig. 2). In essence, observed photoacidic properties of HPTS are fundamentally associated with solvent relaxation and the acceptance of protons by protic solvents (hydrogen bonding) [41,42]. The solvent relaxation arises via the axial rotation of the surrounding solvent molecules due to the slightly modified dipole moments in the excited HPTS* [24]. Due to difficulties to resolve the O–H stretch in water, Mohammed et al. [41] used transient mid-infrared spectroscopy to evaluate optical properties of HPTS in DMSO. In DMSO, there was a pronounced absorption maximum at ~3400 cm^{-1}, i.e. close to the energy gap between the two observed (Fig. 3b) emission maxima at 432 and 508 nm (~3460 cm^{-1}). Therefore, a plausible route for relaxation of HPTS* in water is that the O–H stretch, through intra-molecular resonance energy transfer (RET), absorbs vibration energy during the electronic relaxation. A decreased pK_a for HPTS* would thus be expected and the photoacidity of the molecule is realized. The remaining difference in energy could be related to additional rearrangement of dipoles following the deprotonation of HPTS* in water.

Due to the photoacidic properties of HPTS, the electronic transition from ^1L_a to S_1 in HPTS* is highly probable, and in water at pH > 3 the transition is practically complete. As a consequence, the emission band at ~510 nm is particularly favored compared to the fluorescence emission at ~430 nm. In combination with the pronounced emission (λ_{em} ~ 510 nm) following excitation of deprotonated HPTS at ~450 nm, a dual excitation/single emission sensing scheme is particularly suitable for signal amplification in protic solvents.

3.3. *Fluorescent properties of HPTS immobilized in ethyl-cellulose*

The general concept behind the dual excitation/dual emission ratiometric sensing scheme utilized in this study can be deduced from the excitation and emission spectra of HPTS immobilized in the ethyl-cellulose sensing membrane (Fig. 3a and b). In contrast to the commonly used properties of HPTS with a dual excitation/single emission fluorescence ratio (i.e., ex/em: 403/511 nm and ex/em: 454/511 nm; [36]), we observed dual excitation and dual emission properties of HPTS immobilized in ethyl-cellulose (F_1, ex/em: 405/440 nm and F_2, ex/em: 465/510 nm). Thus, we realize that for HPTS* immobilized in a restricted and hydrophobic environment such as the ethyl-cellulose membrane, the transition of electrons from ^1L_a to S_1 is severely hindered, probably due to a reduced vibrational overlap and increment of S_1 energy. As a direct consequence, the photoacidity of HPTS is significantly reduced. At pH < pK_a, most pronounced excitation of the sensor was found at ~405 nm, with a second maximum at ~383 nm (Fig. 3a). This pattern of fluorescence is likely associated with the electronic transition from S_0 to ^1L_b and from S_0 to ^1L_a, respectively (Fig. 2). Below pK_a, immobilized HPTS* relaxes via solvent molecules and vibrations (and conversion from ^1L_b to ^1L_a if excited at ~405 nm). Sequentially it either fluoresces by the transition ^1L_a to S_0 (λ_{max} = ~432 nm), or transfers part of the energy by resonance linking of vibrations in the pyrene ring and the O–H stretch (RET). However RET occurs to a much smaller extent in the ethyl-cellulose membrane than in water. As a consequence from deprotonation caused by RET, a shoulder peak was also observed at ~508 nm in the emission spectrum (corresponding to the electron transfer S_1 to S_0). The latter fluorescence was, however, significantly smaller than that observed at 432 nm (Fig. 3b). At pH > pK_a, excitation maximum of the deprotonated fluorophore is red-shifted to ~465 nm. Due to the insignificant probability for protonation of excited HPTS ($^3sPyO^{-*}$) when pH > pK_a, main relaxation pathway is the combined solvent – vibrational – fluorescence (λ_{max} ~ 515 nm). The small red-shift of this maximum with increasing pH (508 to 515 nm) is likely caused by the decreased energy of the S_1 orbital (Fig. 2) [42]. Based on our experimental observations of HPTS immobilized in ethyl-cellulose, a dual excitation/dual emission normalization protocol seems more feasible than a dual excitation/single emission sensing scheme. Furthermore, signal amplification was improved by several orders of magnitude and the signal to noise ratio increased by ~400% using the dual excitation/dual emission sensing scheme compared to the protocol normally associated with HPTS fluorescence (Fig. 4a).

3.4. *Time-dependent drift of sensor parameters*

Directly based on observations of a time-dependent multilinear drift of sensor response (e.g., samples in Fig. 4b), the calibration parameters were assumed to correlate in a linear fashion to this drift (Eq. (2)). The parametric time-dependent drift can be illustrated by the evolution of the sigmoidal calibration functions with time of experiment (Fig. 5). How the fluorescence ratio is expected to drift over time as an outcome of the linear parametric compensation is exem-

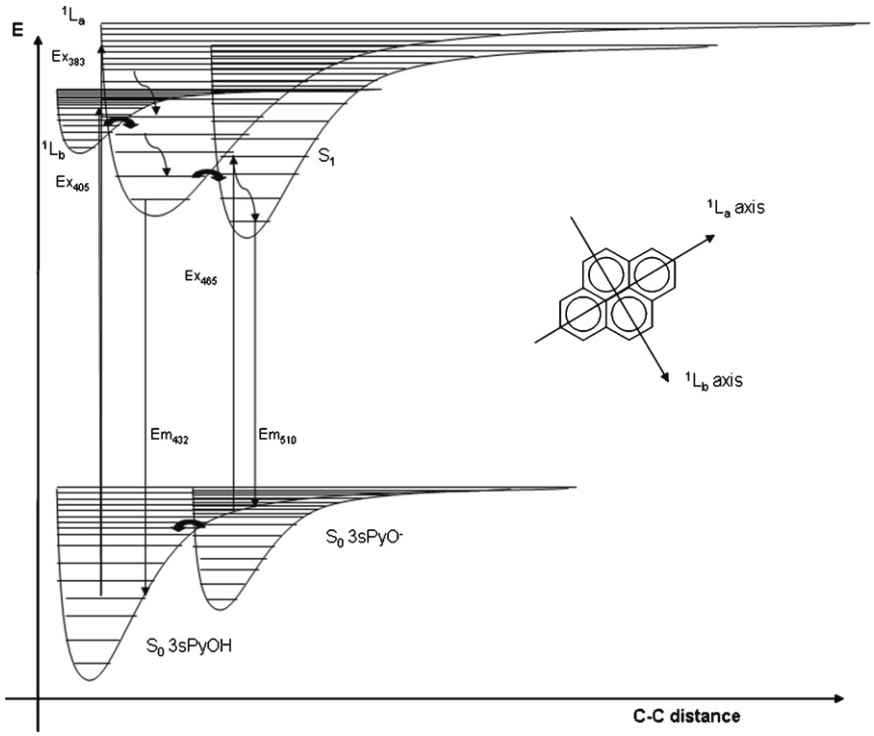

Fig. 2 – Schematic representation of the ground state and excited state dynamics for HPTS dissolved in water (pH ~ 4). 3sPyOH and 3sPyO$^-$ denote protonated and deprotonated HPTS, respectively. According to most recent models, the first singlet excited state (S_1) of the photoacid is degenerated to ^1L_a and ^1L_b, corresponding to through-atom and through-bond axis, respectively [38,41,42].

plified by linear regressions of calculated ratio (model B, pH_{optode} = 6.986, 7.702, and 7.828) with time (insertion Fig. 5). Linear correlation coefficients were above 0.9974. Further, the good agreement between experimental and modeled ratio is demonstrated. The pK_a (α_3) of HPTS immobilized in the ethyl-cellulose sensor film ranged between 6.74 and 7.19 (Fig. 5), with a progressively increasing pK_a with time of experiments. Significantly higher pK_a (up to ~8.5) was observed for sensors

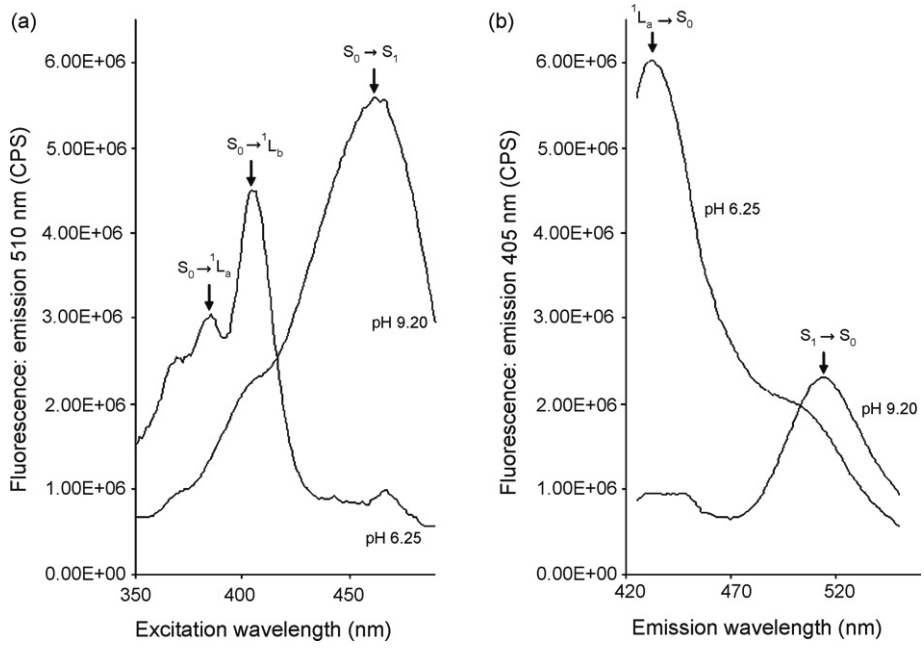

Fig. 3 – (a) Fluorescence excitation spectrum (emission at 510 nm, slit widths: ex 5 nm/em 2 nm) and (b) fluorescence emission spectrum (excitation at 405 nm, slit widths: ex 2 nm/em 2 nm) for HPTS immobilized in ethyl-cellulose at pH 6.25 and 9.20.

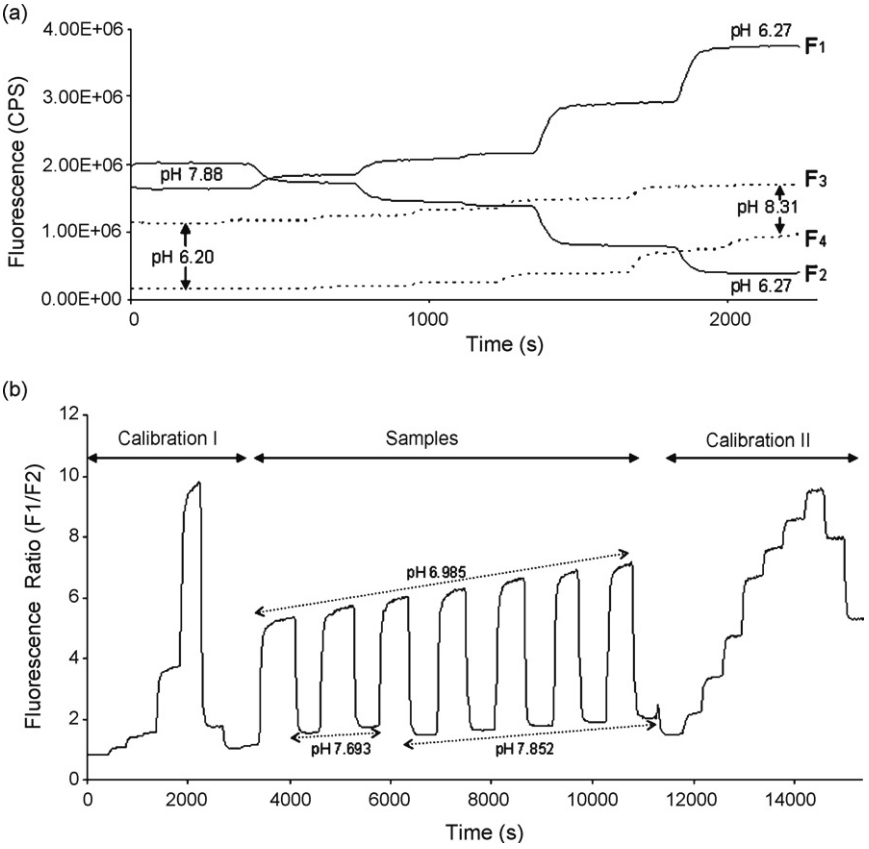

Fig. 4 – (a) A comparison between representative examples of individual fluorescence signals (F_1, ex/em: 405/440 nm and F_2, ex/em: 465/510 nm, solid lines), and the more commonly used dual excitation/single emission calibration (F_3 ex/em: 405/510 nm and F_4 ex/em: 455/510 nm, dotted lines) of HPTS immobilized in ethyl-cellulose. (b) Raw data of dual excitation/dual emission fluorescence ratio ($R_{F_1,F_2} = F_1/F_2$) for a set of samples between two calibrations ($n = 8$ and $n = 11$).

following long-term experiments (weeks) and for membranes exposed to a prolonged rinsing procedure before use (not shown). The lower end ($pK_a \sim 6.7$) of apparent pK_a for immobilized HPTS is slightly higher, but similar to, observations of HPTS immobilized by hydrophobic interactions onto cellulose acetate ($pK_a \sim 6.4$) [6], but lower than pK_a observed for HPTS in free solution ($pK_a \sim 7.3$) [36]. Values of pK_a in the higher end ($pK_a > 8$) resemble those reported for HPTS immobilized in ethyl-cellulose by ionic interactions ($pK_a \sim 8.4$) [5]. A time-dependent drift in calculated pK_a of the ratiometric pH fluorosensor is therefore likely associated with the immobilization technique and the complex interactions of HPTS in the sensing membrane. There are at least four main types of HPTS interactions in the sensing membrane, including HPTS attached to TOA^+ by ionic attractions, HPTS physically entrapped in the ethyl-cellulose network, HPTS immobilized by hydrophobic interactions, and "free" HPTS. Although combinations of equilibrium reactions and reaction feedbacks further increase the complexity of the sensor system, "free" HPTS is likely easily leachable from the membrane during the experimental procedure. A diffusive and turbulent (e.g., during active rinsing) removal of "free" HPTS from the membrane would therefore cause an increased pK_a with time of experiment, as was also supported by experimental observations (Fig. 5). It is thus possible to shift the pK_a of the sensor and thereby the dynamic range of sensor response depending on the immobilization and pre-treatment procedure.

The extreme values of the sigmoidal calibration function (α_1 and α_2) were affected in the opposite way throughout experiments (Fig. 5). While values for α_1 increased (0.27–0.67), α_2 values decreased with time (12.23–10.98). Ideally, this drift would have been eliminated and normalized by the ratiometric procedure. However, due to the complex mixture of HPTS interactions including leaching, quenching and bleaching, there were non-constant excitation and emission properties of HPTS in the sensor membrane.

The slope of the sigmoidal calibration function (α_4) increased from 1.164 to 1.247 during 3.25 h of experiments. However, as the asymptotic maximum (α_1) and minimum (α_2) simultaneously converged, the sensitivity of the sensor was only modestly affected. In fact, the derivative of the sigmoidal calibration function where pH equals the pK_a of the sensor (i.e., maximum sensitivity) decreased in a linear fashion by ~5%, from −7.849 to −7.422.

3.5. *Sensor performance*

Experiments were conducted, and sensor performance and overall quality control evaluated, under non-optimized condi-

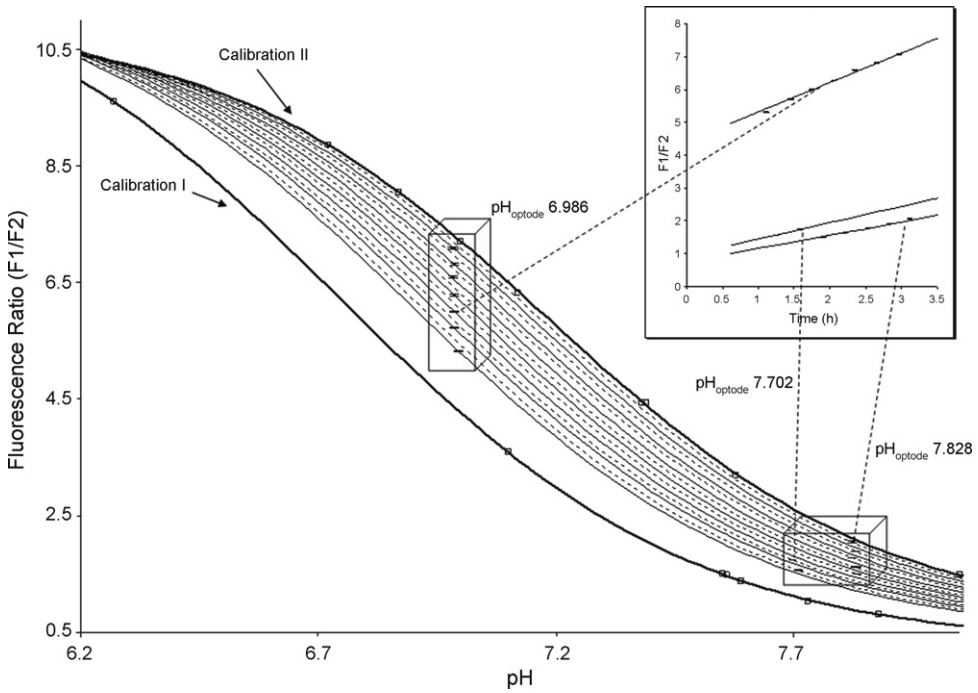

Fig. 5 – Least squares four-parameter sigmoidal fit of experimental data (□) describing calibrations prior to (I) and after (II) sample analysis. Calibration functions calculated from the drift in parameters are illustrated for the samples pH$_{optode}$ 6.986 (solid lines), and pH$_{optode}$ 7.702 and 7.828 (dotted lines). Sample concentrations predicted from the sigmoidal functions are shown as error bars (±S.D., $m = 10$). The insertion shows linear regressions of modeled (model B) fluorescence ratio with experimental time, for the average optode values. Equations and correlation coefficients are: $y_{6.986} = 0.8996x + 4.4222$, $R^2 = 0.9993$; $y_{7.702} = 0.4962x + 0.9495$, $R^2 = 0.9975$; $y_{7.828} = 0.4034x + 0.7531$, $R^2 = 0.9974$. Experimental fluorescence ratio are shown as error bars (±S.D., $m = 10$).

tions frequently found in ordinary laboratory environments. For example, calibration solutions were mixed on-line in a random fashion, and measurements were performed at ambient room temperature (20 ± 1 °C). Fig. 6 shows calculated data for the three ratiometric quantification models. Comparing the analytical performance, referred to as the pooled standard deviation of pH measurements, utilizing the ratiometric models A (piece-wise linear calibration and linear correction with time), B (four-parameter sigmoidal calibration and linear correction of parameters with time), and C

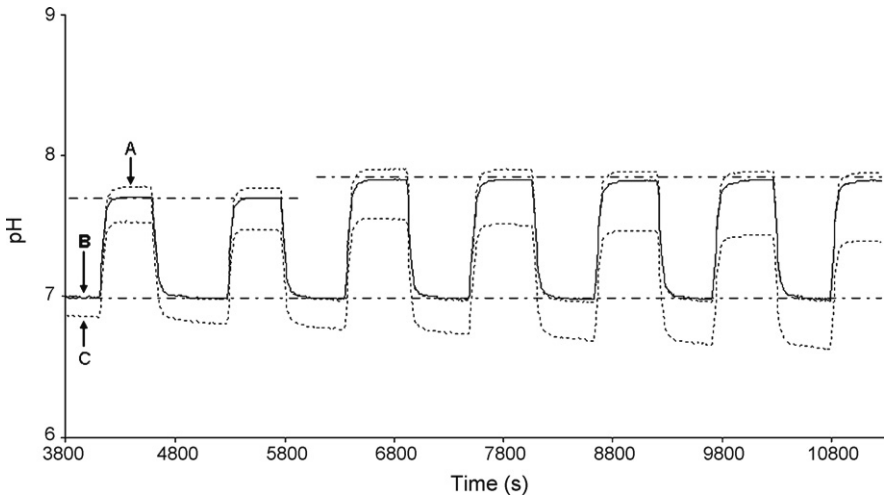

Fig. 6 – A comparison of pH (samples from Fig. 4b) predicted from the three models used to quantify pH – (A) piece-wise linear calibration: linear correction with time (dotted line); (B) four-parameter sigmoidal calibration: linear correction of parameters with time (solid line); (C) four-parameter sigmoidal calibration: single calibration (i.e., no correction with time, dotted line). The dash–dotted lines display mean values of sample pH (6.985, 7.693 and 7.852) measured on-line by a pH electrode.

Table 1 – Precision and accuracy for the calibration models

	Ref. (ISE)	Model A	Model B	Model C	Model C[a]
Mean ($n=7$)	6.985	6.975	6.986	6.738	7.128
S.D.	0.004	0.009	0.004	0.080	0.087
Accuracy[b]	–	−0.010	0.001	−0.247	0.143
Mean ($n=2$)	7.693	7.775	7.702	7.499	7.975
S.D.	–	–	–	–	–
Accuracy[b]	–	0.083	0.009	0.193	0.282
Mean ($n=5$)	7.852	7.894	7.828	7.468	7.937
S.D.	0.005	0.009	0.004	0.062	0.078
Accuracy[b]	–	0.041	−0.025	−0.384	0.084
Pooled S.D. ($n=14$)	0.0046	0.0091	0.0044	0.0707	0.0812

[a] Calibration performed after samples.
[b] Difference between the mean of the model and the mean of the reference method (ISE).

(four-parameter sigmoidal calibration without correction with time), the repeatability of measurements was significantly better for model B (P.S.D. = 0.0044 pH units) than for the other two evaluation procedures (model A: P.S.D. = 0.0091, model C: P.S.D. = 0.0707). The within laboratory repeatability of the ratiometric pH sensor, calibrated using the four-parameter sigmoidal calibration and linear correction of parameters with time (model B), was similar to that of the pH electrode (P.S.D. = 0.0046). Considering the experimental conditions of calibrations and measurements, the performance of the ratiometric fluorosensor implementing non-linear calibration protocols for drift compensation was in close agreement (or even better) than that of the reference method (ISE). In principle, the overall performance of the pH fluorosensor was thereby limited by that of the pH electrode used during standardization. For comparison, excluding sensor error and under reference conditions, the repeatability (S.D.) of the potentiometer used together with the pH electrode was ∼0.003 pH units [47]. A precision (S.D.) of down to ±0.001 pH units has been demonstrated by utilizing absorbance-based pH indicators such as Phenol Red, however requiring a temperature control of ±0.1 °C [48]. Experiments utilizing fiber optic pH sensing based on phase fluorescence lifetime reported a precision and accuracy of ∼0.02 pH units [11]. The overall performance of the ratiometric pH fluorosensor developed in this study, implementing time-dependent non-linear calibration protocols for drift compensation, was therefore comparable to those of pH electrodes and absorbance-based pH indicators, but seemed better than the performance of fluorescence lifetime-based sensors. Furthermore, the calibration protocol provides a versatile analytical tool to enhance sensor precision and accuracy (Fig. 6 and Table 1), as well as the applicable lifetime of the optical sensor (time of operation within a certain analytical performance).

4. Conclusion and outlook

We have successfully implemented a time-dependent, non-linear calibration protocol on ratiometric fluorescence from the pH sensitive fluorophore 8-hydroxypyrene-1,3,6-trisulfonic acid. Due to the significantly reduced photoacidity of HPTS immobilized in the ethyl-cellulose sensing membrane, a dual excitation/dual emission (F_1, ex/em: 405/440 nm and F_2, ex/em: 465/510 nm) ratiometric ($R_{F_1,F_2} = F_1/F_2$) sensing scheme was utilized to amplify sensor response. Using the dual emission sensing scheme, the signal to noise ratio was enhanced by ∼400%. Sensor performance, including the time-dependent non-linear calibration procedure, was limited by the electrode used for standardization. The apparent pK_a of the sensor ranged from 6.74 to 8.50, mainly determined by the immobilization procedure of HPTS. Principles and mechanisms of the ratiometric fluorosensor, implementing non-linear calibration protocols for drift compensation, can be applied for pH measurements in a variety of environments. Complex sampling environments include e.g., soils and aquatic sediments, and bioanalytical applications for cells and cell-signalling networks. In principle, the non-linear calibration protocols for drift compensation presented in this study are likely to be general and applicable on optical sensors that show a sigmoidal response that demonstrates an explicit linear drift.

Acknowledgements

Financial support was obtained from the Swedish Research Council (VR), the Foundation for Strategic Environmental Research (MISTRA), the Swedish Research Council for Environment, Agricultural Sciences and Spatial Planning (FORMAS), and the Swedish Marine Research Centre (GMF). N. Strömberg provided comments that improved the manuscript. The final manuscript benefited from comments made by the Editor and two anonymous reviewers.

REFERENCES

[1] J.I. Peterson, S.R. Goldstein, R.V. Fitzgerald, D.K. Buckhold, Anal. Chem. 52 (1980) 864.
[2] L.A. Saari, W.R. Seitz, Anal. Chem. 54 (1982) 821.
[3] Z. Zhujun, W.R. Seitz, Anal. Chim. Acta 160 (1984) 47.
[4] S.G. Schulman, S.X. Chen, F.L. Bai, M.J.P. Leiner, L. Weis, O.S. Wolfbeis, Anal. Chim. Acta 304 (1995) 165.
[5] M.F. Choi, J. Photochem. Photobiol. A-Chem. 104 (1997) 207.
[6] S. Hulth, R.C. Aller, P. Engstrom, E. Selander, Limnol. Oceanogr. 47 (2002) 212.

[7] Q.Z. Zhu, R.C. Aller, Y.Z. Fan, Environ. Sci. Technol. 39 (2005) 8906.
[8] C. Munkholm, D.R. Walt, F.P. Milanovich, S.M. Klainer, Anal. Chem. 58 (1986) 1427.
[9] G. Gabor, D.R. Walt, Anal. Chem. 63 (1991) 793.
[10] H. Szmacinski, J.R. Lakowicz, Anal. Chem. 65 (1993) 1668.
[11] R.B. Thompson, J.R. Lakowicz, Anal. Chem. 65 (1993) 853.
[12] A. Song, S. Parus, R. Kopelman, Anal. Chem. 69 (1997) 863.
[13] G. Liebsch, I. Klimant, C. Krause, O.S. Wolfbeis, Anal. Chem. 73 (2001) 4354.
[14] A.J. Marshall, J. Blyth, C.A.B. Davidson, C.R. Lowe, Anal. Chem. 75 (2003) 4423.
[15] I. Sanchez-Barragan, J.M. Costa-Fernandez, A. Sanz-Medel, M. Valledor, F.J. Ferrero, J.C. Campo, Anal. Chem. Acta 562 (2006) 197.
[16] S.A. Borman, Anal. Chem. 53 (1981) A616.
[17] W.R. Seitz, Anal. Chem. 56 (1984) A16.
[18] X.P. Li, Z. Rosenzweig, Anal. Chem. Acta 353 (1997) 263.
[19] S.M. Borisov, O.S. Wolfbeis, Anal. Chem. 78 (2006) 5094.
[20] S.M. Barnard, D.R. Walt, Nature 353 (1991) 338.
[21] J. Ji, Z. Rosenzweig, Anal. Chem. Acta 397 (1999) 93.
[22] J. Janata, Anal. Chem. 59 (1987) 1351.
[23] R.Y. Tsien, M. Poenie, Trends Biochem. Sci. 11 (1986) 450.
[24] J.R. Lakowicz, Principles of Fluorescence Spectroscopy, Kluwer Academic and Plenum, New York, 1999.
[25] N. Stromberg, S. Hulth, Sens. Actuators B-Chem. 90 (2003) 308.
[26] R.B. Thompson, E.R. Jones, Anal. Chem. 65 (1993) 730.
[27] E.J. Park, M. Brasuel, C. Behrend, M.A. Philbert, R. Kopelman, Anal. Chem. 75 (2003) 3784.
[28] R. Badugu, J.R. Lakowicz, C.D. Geddes, J. Fluoresc. 14 (2004) 693.
[29] A. Ojida, H. Nonaka, Y. Miyahara, S.I. Tamaru, K. Sada, I. Hamachi, Angew. Chem. Int. Ed. 45 (2006) 5518.
[30] H. Xu, J.W. Aylott, R. Kopelman, T.J. Miller, M.A. Philbert, Anal. Chem. 73 (2001) 4124.
[31] K. Kurihara, M. Ohtsu, T. Yoshida, T. Abe, H. Hisamoto, K. Suzuki, Anal. Chem. 71 (1999) 3558.
[32] N. Stromberg, S. Hulth, Anal. Chem. Acta 443 (2001) 215.
[33] N. Stromberg, S. Hulth, Anal. Chem. Acta 550 (2005) 61.
[34] N. Stromberg, S. Hulth, Sens. Actuators B-Chem. 115 (2006) 263.
[35] IUPAC Compendium of Chemical Terminology, International Union of Pure and Applied Chemistry, 1997.
[36] R.P. Haugland, The Handbook: A Guide to Fluorescent Probes and Labeling Technologies, Invitrogen Corp., 2005.
[37] T. Forster, Naturwissenschaften 36 (1949) 186.
[38] T.H. Tran-Thi, T. Gustavsson, C. Prayer, S. Pommeret, J.T. Hynes, Chem. Phys. Lett. 329 (2000) 421.
[39] M. Rini, B.Z. Magnes, E. Pines, E.T.J. Nibbering, Science 301 (2003) 349.
[40] J.T. Hynes, T.H. Tran-Thi, G. Granucci, J. Photochem. Photobiol. A-Chem. 154 (2002) 3.
[41] O.F. Mohammed, J. Dreyer, B.Z. Magnes, E. Pines, E.T.J. Nibbering, Chemphyschem 6 (2005) 625.
[42] T.H. Tran-Thi, C. Prayer, P. Millie, P. Uznanski, J.T. Hynes, J. Phys. Chem. A 106 (2002) 2244.
[43] E. Bardez, A. Chatelain, B. Larrey, B. Valeur, J. Phys. Chem. 98 (1994) 2357.
[44] W. Domcke, A.L. Sobolewski, Science 302 (2003) 1693.
[45] R. Knochenmuss, S. Leutwyler, J. Chem. Phys. 91 (1989) 1268.
[46] O.F. Mohammed, D. Pines, J. Dreyer, E. Pines, E.T.J. Nibbering, Science 310 (2005) 83.
[47] 780 pH Meter: Instructions for use, Metrohm AG, Herisau/Switzerland, 2002.
[48] G.L. Robertbaldo, M.J. Morris, R.H. Byrne, Anal. Chem. 57 (1985) 2564.

Paper III

Analytica Chimica Acta 636 (2009) 89–94

Contents lists available at ScienceDirect

Analytica Chimica Acta

journal homepage: www.elsevier.com/locate/aca

An imaging pH optode for cell studies based on covalent attachment of 8-hydroxypyrene-1,3,6-trisulfonate to amino cellulose acetate films

Niklas Strömberg*, Erik Mattsson, Aron Hakonen

Department of Chemistry, Göteborg University, SE-412 96 Göteborg, Sweden

ARTICLE INFO

Article history:
Received 21 November 2008
Received in revised form 16 January 2009
Accepted 22 January 2009
Available online 30 January 2009

Keywords:
pH
Imaging
Optode
Planar
Cells
Neurons

ABSTRACT

The objective of this study was to create a thin film optode for fast pH measurements that meets the requirements for imaging pH-responses from cells as well as for a future hybrid design for detection of multiple analytes simultaneously. The sensor is based on the covalent attachment of 8-hydroxypyrene-1,3,6-trisulfonate (HPTS) to a film forming cellulose acetate material through a sulfonamide linkage. The synthesis routes of the cellulose material and regio-specific covalent attachment of the dye are described in detail. The sensor was sterilized in two different ways and showed excellent biocompatibility with Chinese hamster ovary cells. Imprints from cells and μm thin cell extensions were visualized when altering pH of the surrounding solution. The sensor was tested together with time-dependent sigmoidal calibrations giving pH determinations with an exceptional precision and accuracy during measurement within pH 6–8. The precision of the optode, calculated as pooled S.D. ($n = 8$) according to IUPAC recommendations between pH 6.641 and 7.742 was 0.0029. The accuracy was significantly better than the electrode used as reference during the measurements. The response time (0–95%) was 100 s between pH 6.641 and 7.742 and the reverse response (95–0%) was 80 s. The sensor shows great potential for extra-cellular pH determination over time during cell growth and pharmacological exposure.

1. Introduction

Extra- and intracellular qualitative measurements of ions using fluorescent dyes have been used successfully over the past 30 years. Normalization procedures based on fluorescence intensity ratios have increased the analytical performance of these measurements dramatically [1] and are nowadays fairly applicable for quantification. The drawback associated with these techniques are, however, that dye sensors distributed in the cell matrix become hard to calibrate due to matrix effects such as uneven dye distribution and highly unpredictable quenching conditions. Further, there are severe problems with signal drift due to photobleaching and uneven leaching from stained cells and tissues even though fluorescence is normalized by quotients [1]. Although qualitative information can be retrieved, dye interactions with proteins, organelles and adsorption to cell walls make reliable quantifications of the analyte very difficult. By using imaging optodes instead of dye sensors, extracellular quantification of analytes can be made with a minimum of these artifacts. The general principle of optodes is to incorporate the dye sensor in a solute permeable material, which is in close vicinity but not in direct contact with the object. The concept makes it possible to transfer the sensing scheme to any matrix, minimize matrix effects since the sensing scheme is confined in a protected environment and perhaps most notably calibrations become feasible. Furthermore, calibrations before and after the experiment (i.e. time correlated calibrations), facilitate compensations for signal drift over time and help keeping track of analytical performance during the experiment [2,3]. Due to these interesting features, dye interactions are minimized and the accuracy of the measurements is maintained.

Despite numerous sensors and optodes for pH measurements [4–17], most of them have been designed for clinical and physiological non-imaging applications [4,5,17]. Imaging optodes for pH have successfully been used as a research tool for sediment studies [15,18]. However, cell applications, where cells are grown directly on top of the sensor material [19] and the rather recent introduction of multi-analyte (hybrid) optodes for simultaneous detection of several analytes or physical parameters [20–22] put new demands on the optode design. A common design for pH optodes rely on dissolution of the dye in a plastic material together with a hydrophobic counter ion, for example tetraoctylammonium (TOA+) [7]. Both the additive and dye can leak from these sensors and thereby makes it difficult to design hybrid optodes based on either coextraction or ion exchange together with this type of pH sensor. Moreover, in a measurement where cells are grown directly onto the optode film, leakage of chemicals might affect the natural cell growth and

* Corresponding author. Tel.: +46 31 7722784; fax: +46 31 7722785.
E-mail address: niklasst@chem.gu.se (N. Strömberg).

0003-2670/$ – see front matter © 2009 Elsevier B.V. All rights reserved.
doi:10.1016/j.aca.2009.01.045

cell adsorption to the surface. Alternatively, dye sensors have been covalently attached to e.g. polyvinyl alcohol (PVA) [18]. However, PVA swells in water providing a redundantly thick film (which gives poor response times) and are temperature sensitive. Further, the dye is coupled to the film via a rather weak ester linkage, hence becomes susceptible to photoionization. What is lacking is a thin film forming biocompatible material with properties for a sturdy regio-selective attachment of the pH-sensitive dye. In a pioneering work by Tiller et al. [23], cellulose was modified and designed at a molecular level to give good film forming properties and functionality for an amide linkage. The film forming properties were altered by changing the lengths of the ester covalently attached to the secondary alcohols on the backbone of cellulose while the primary alcohol on cellulose was unaffected due to a protecting group. The primary alcohol at carbon 6 was then regio-selectively replaced with a diamine by removal of the protecting group, thus facilitating a handle for covalent attachment through a strong amide linkage.

The objective of this study was to create a thin film optode for fast pH measurements that meets the requirements for imaging pH-responses from cells as well as for a future hybrid design for detection of multiple analytes simultaneously. Thus, the sensor should ideally respond within the physiological pH range i.e. pH 6–8, be thin in order to get fast response times, possible to sterilize and have minimal leakage of the dye or other sensor components. In this study 8-hydroxypyrene-1,3,6-trisulfonate (HPTS), a commonly used fluorescent ratiometric pH dye, was chlorinated and regio-selectively attached to an amino cellulose acetate matrix (see Fig. 1). Covalent attachment makes it possible to measure pH responses without additives or risk for dye leakage. The response of the sensor was tested before and after sterilization by ultraviolet light and autoclavation. Finally, the resulting sensor was used to study pH alterations made within the extra-cellular solution surrounding spontaneously fixed cells.

2. Experimental

2.1. Chemicals

All chemicals, 8-hydroxypyrene-1,3,6-trisulfonic acid (HPTS), Avicel® PH-101, N,N-dimethylacetamide (DMA), lithium chloride (LiCl), sodium chloride (NaCl), potassium chloride (KCl), phosphoric acid, p-toluene-4-sulfonylchloride, toluene, acetone, isopropyl alcohol (IPA), triethylamine (TEA), methanol, ethanol, dimethylformamide (DMF), acetonitrile (ACN) sodium acetate (anhydrous), acetic anhydride, pyridine, dimethyl sulfoxide (DMSO), ethylenediamine, phosphorus pentachloride were from Sigma–Aldrich. All chemicals except for Avicel® (see preparation procedure) were used without any further purification and used as received. The specific batch of Avicel® had a degree of polymerization of 218 according to the manufacturer i.e. on average 218 anhydrous glucose units (AGU:s) are linked together.

Glassware used in the synthesis was heated to 200 °C for 24 h before use. Chlorination of HPTS were made using PCl_5 in DMF or acetone. Due to the changes and modifications in addition to that many steps comes from separate articles [23–26] the full typical procedure for the synthesis of the support material (amino cellulose acetate) are given below.

2.2. Pretreatment of Avicel® PH-101

Avicel® PH-101 (20 g), was stirred vigorously with Milli-Q H_2O (100 mL), for 24 h, suction filtered (fritted glass funnel pore size 1) to dryness. Next the white solid powder was stirred vigorously in methanol (100 mL) for 1 h and thereafter suction filtrated. This step was repeated three times. Finally methanol washed Avicel® was stirred 1 h in DMA (100 mL) and subsequently suction filtrated. The last procedure was done five times.

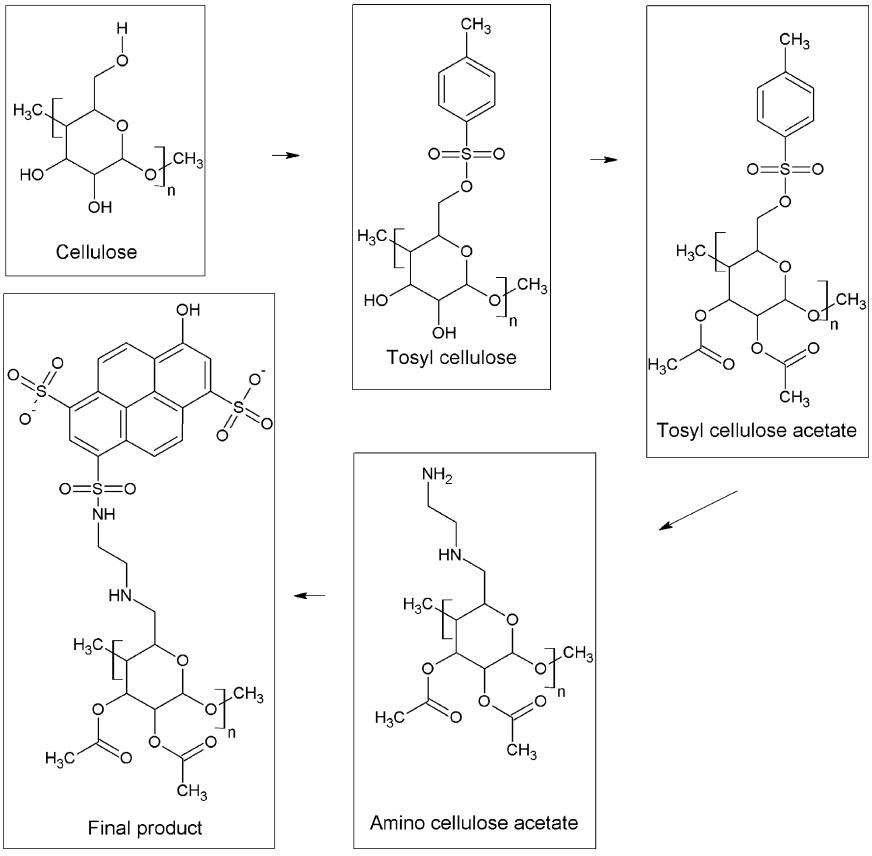

Fig. 1. Description of the synthesis steps from Avicel® (cellulose starting material) to final product for the thin film pH sensor.

Stock solution for cellulose dissolution was prepared by dissolving of LiCl (8.4 g) in DMA (100 mL). The solution was heated to 80 °C and thereafter cooled to room temperature before use.

2.3. Synthesis of tosyl cellulose

The pretreated Avicel® (2 g wet weight after suction to dryness; corresponding to 1.4 g dry weight) was dissolved in the DMA/LiCl solution (100 mL) in a three-neck round-bottom flask equipped with a Liebig condenser, dropping funnel and gas (N_2 (g)) inlet to provide inert atmosphere. The solution became turbid after heating to 80 °C but after cooling to 40 °C in room temperature the solution became completely clear. TEA (49 mL; 352 mmol) was added dropwise through the dropping funnel. Another solution of p-toluene-4-sulfonylchloride (22.4 g; 116 mmol) in DMA (40 mL) was added through the dropping funnel and the solution was cooled by immersing the round-bottom flask in an ice bath for 24 h. The brown precipitate solution was thereafter suction filtered (fritted glass funnel pore size 2) and the filtrate was precipitated on ice (600 g). The resulting product and ice mixture was filtered and then washed in methanol (2× 200 mL) and Milli-Q H_2O (5 l). The resulting product (3.82 g) was dried in a desiccator for 24 h.

2.4. Acetylation of tosyl cellulose

Dry tosylated cellulose (3.82 g) was dissolved in DMF (20 mL) in a three-neck round-bottom flask. Another solution of sodium acetate (1.62 g), pyridine (18 mL; 412 mmol, 12 equiv./AGU)), acetic acid anhydride (15.6 mL; 336 mmol, 10 equiv./AGU) and DMF (20 mL), was poured over the dissolved tosyl cellulose and the temperature was elevated (40 °C) for 48 h. The resulting product was precipitated in ice cooled ethanol (100 mL) (fritted glass funnel pore size 2) and washed by pouring the filtrate (3× 100 mL) through the funnel under reduced pressure. The solid product was dried in desiccator for 24 h.

2.5. Amination of cellulose acetate

The tosylated cellulose acetate product was dissolved in DMSO (15 mL), 1,2-diaminoethane (3.78 mL; 420 mmol). The temperature was raised to 80 °C for 16 h. The final product was precipitated in ice water mixture (100 mL), suction filtrated (fritted glass funnel pore size 2) and washed by pouring the filtrate (3 × 100 mL) through the funnel under reduced pressure. The resulting product dry weight was 0.5 g after drying in a desiccator for 24 h. The dried product was immediately dissolved in 20 mL DMSO.

2.6. Synthesis of 8-hydroxypyrene-1,3,6-trisulfonic acid chloride and dye attachment

HPTS (20 mg) and PCl_5 (200 mg) in 1:10 (w/w) were mixed together (dry) in a three-neck round-bottom flask with nitrogen sparging. Thereafter DMF or acetone (10 mL) was poured through the condenser and the solution was heated to 60 °C for 1 h. Prior to dye attachment the complete batch of amino cellulose acetate dissolved in DMSO was heated to 70 °C during sonication for 5 min to break clusters. The dye solution was centrifuged 8000 rpm for 10 min and aliquots of the supernatant (54 μL) transferred without purification via syringe to a vial containing 100 μL amino cellulose acetate dissolved in DMSO (2.3%, w/w). The resulting solution has a 1:100 molar ratio relation (HPTS/AGU) based on mole HPTS to be chlorinated (assuming 100% chlorination efficiency). The reaction mixture heated to 70 °C and mixed for at least 1 h before casting. Pyridine (10 times mole HPTS used for chlorination) was also added to some of the sensor cocktails to test basic pH conditions for the covalent attachment to the amino cellulose material.

Casting the solution on substrates resulted in the thin film pH optode. The organic synthesis steps of the cellulose material were in this study followed by infrared spectroscopy (Perkin-Elmer 1600 FTIR; see spectra supporting info). Electrospray mass spectrometry (ESI-MS) was used for evaluation of chlorination efficiency (Micromass Quattro-LC) of the dye. DMF has a high boiling point (bp 153 °C) and is not easily removed and incompatible with ESI-MS analysis. Therefore, the compound synthesized in acetone was used for such analysis. The dye solution was rotary evaporated to dryness and thereafter 4.9 mg of the chlorinated product was dissolved in 100 mL ACN and the resulting mass spectrum was compared to mass spectrum of equally concentrated HPTS in 50/50 ACN/Milli-Q solution (Fig. S1; supporting information).

2.7. Preparations of substrates and casting techniques

28 mm in diameter deckgläser (Menzel-Gläser) were washed in acetone or IPA and dried under nitrogen before amino cellulose acetate was added to the slide. The cleaned slides were spin coated at 600 rpm for 30 s using a simple spin coater made in the lab. Thin films were also produced by adding 20 μL solution on to a microscope slide, press another slide on top, and thereafter pull the slides apart. Sensors were also spun onto cellulose acetate film (thickness = 100 μm) for determination of the spectral properties as well as collection of response curves in a spectrofluorometer. Before any measurements the sensors were washed in copious amount of Milli-Q and thereafter stored in buffer solution before use.

2.8. Sterilization and cell culturing

Sensors were exposed to intense ultraviolet light for 30 min or autoclaved at 120 °C for 1 h in a sterile bag. The responses were compared with how the same sensor responded prior sterilization. Chinese hamster ovary cells were seeded on to the autoclaved sensor (28 mm menzel glass) and incubated in 37 °C.

2.9. Matrix scans and response curves

The sensors spun on cellulose acetate films were mounted onto a Plexiglas support and secured in a custom-made flow-through plastic cuvette (3 mL), placed in the spectrofluorometer (Fluoromax-3, SPEX Instruments Int. Inc.). To minimize background noise and reflection from incident light, the angle of incidence for the excitation light was set to 60°. Matrix scans (excitation (ex) 390–500 nm, emission (em) 400–550 nm) were performed at pH 6.641 and 7742 to determine the optimal excitation/emission wavelength pairs used in a fluorescence ratio. Matrix scans were performed at 10.00 nm resolution, 0.5 s integration time and 2.00 nm band pass.

Working solutions for calibrations were prepared by mixing different ratios of two phosphate buffer solutions of pH 6.641 and 7.742 made of KCl 5 mM and $[PO_4{}^{3-}]_{tot}$ = 10mM adjusted with NaOH and NaCl to give the correct pH and ionic strength; I_{tot} = 145 mM. Mixing of the two buffers was performed on-line with an HPLC pump with multiple input solutions and mixing chambers. The fluorescence retrieved at 510 nm after excitation at 460 nm (F_1) and 405 nm (F_2) were used in a ratio for pH determination (F_1/F_2). Measurements of the ratiometric response to altering pH between 6.641 and 7.742 (Fig. 2) were made in the spectrofluorometer using a 20 s increment, 0.5 s integration time for each wavelength, 2 nm band pass and a continuous buffer flow rate of 10 mL/min. The pH of the final solution was measured on-line with a pH-electrode (model 6.0232.100, 780 pH meter; Metrohm Ltd.), calibrated by a one-point calibration procedure utilizing commercially available buffer solutions certified traceable to NIST Standard Reference Material (pH 7.00 Buffer, Thermo Orion). Temperature during test of the sensor performance was 20 ± 1 °C.

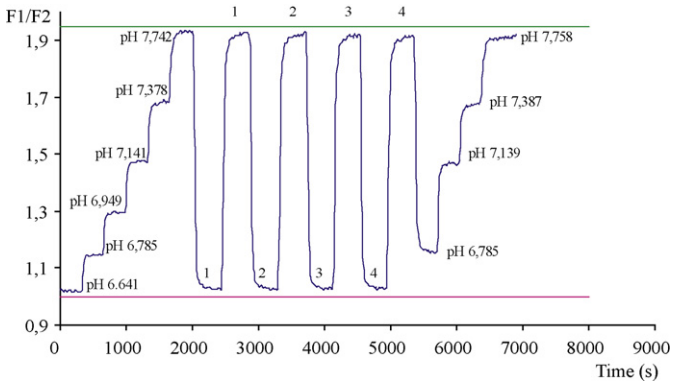

Fig. 2. Calibrations and repeatability test of the optode. The fluorescence response was compared to an electrode inserted after the flow cell (inserted pH values). The readout from the electrode was used as correct values for the fluorescence response in the calibration. The accuracy and precision was determined by altering pH four times (denoted as 1–4 in figure) from pH 6.641 to 7.742 and thereafter compared these absolute values with the readout from the electrode and optode, respectively. The solid lines are inserted to visualize the minimal drift associated with the optode response. However, the accuracy and precision was improved when applying time-dependent sigmoidal calibrations.

2.10. Microscope setup

The pH optode with cells was assembled in a custom-made flow cell attached to a fluorescence microscope (Leica DMI 6000B). Optimal ex/em 460/510 nm and 405/510 nm wavelengths pairs (see Fig. 3) were selected by utilizing two sets of filter cubes I3 (450–490 nm excitation, dichromatic mirror 510 nm and suppression long pass filter with emission from 515 nm) and A4 (360 nm excitation with band pass 40 nm, dichromatic mirror 400 nm and 470 nm emission filter with band pass 40 nm. Buffer solutions were heated to 37 °C and injected over the incubated cells with altering pH between 6.641 and 7.742. The images were normalized through a ratio (I3/A4) for pH measurement.

3. Results and discussion

3.1. The design of thin film imaging optodes

The most important distinction between imaging optodes and dye sensors is that the sensing components for optodes are confined in a material and thereby situated within a close distance but not in direct contact with the sample. Central parameters for speed of such sensors are the film thickness and permeability. Too thick sensors tend to accumulate ions and thereby buffer the responses but on the other hand these sensors provide more sites for dye attachment and become brighter. Thus, there is a balance between maximum dye loading for increased sensitivity and thickness of the sensor for speed. The regio-selective dye attachment suggested here was optimized to a 1:100 ratio of HPTS-Cl:AGU (data not shown). Thus, proton-accepting amino groups were still available in the film for polarity and efficient cell attachment. The autoclaved sensors showed a great adhesion to cells (Fig. 4) but also a large reduction in sensing performance (>80%) probably caused by decomposition of the cellulose matrix at high temperatures. However, UV-sterilized sensors showed a ~30% loss in signal. Thereby, autoclavation must be performed at lower temperatures if it should be used as sterilization method. A way to test the biocompatibility and imaging performances of the thin film and pH optode was to detect shielding of the sensor response by cells attached to the surface when the surrounding pH was altered. The surrounding pH in the buffer was changed from pH 6.641 to 7.742 during ratiometric

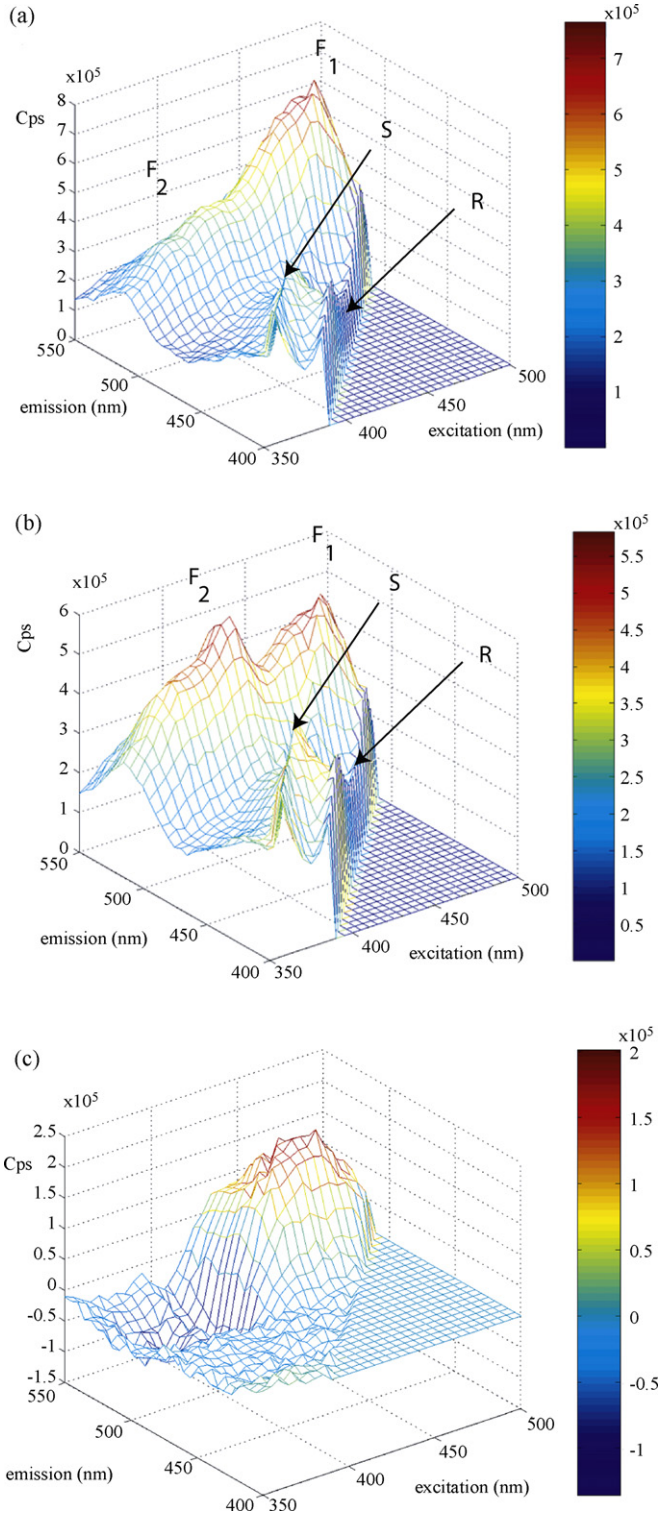

Fig. 3. Matrix scans showing the change fluorescence due to altering pH from 6.0143 (a) to pH 8.0256 (b). F_1 (ex/em 460/510 nm) and F_2 (ex/em 405/510 nm) denote the optimal wavelength pairs used in ratiometric determination of pH. The Reyleigh peaks (R) and the corresponding Stokes–Raman peaks (S) are completely removed after subtraction and are not involved in the pH dependent fluorescence emission. No fluorescence occurs below 500 nm which indicates that the sensor has retained its photoacidic properties.

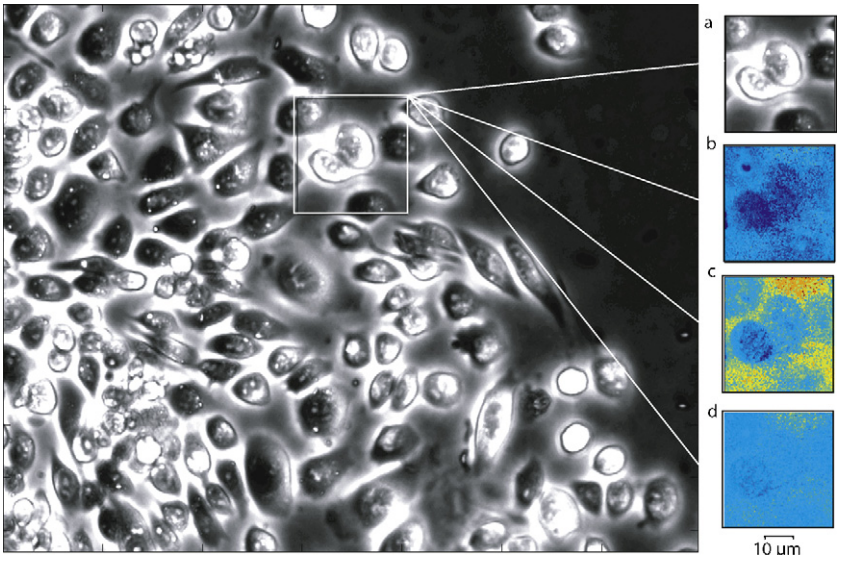

Fig. 4. Bright field image of Chinese ovary cells on top of a sensor coated cover slide (large image), which illustrates the excellent growth conditions and cell attachment associated with the sensor film. Inset images show two closely connected cells in: bright field (a), fluorescence ratio after exposure to pH 6.641 (b) and exposure to pH 7.742 (c). Differences in response ratio (c and b) show clearly the imprint of the cells including cell extensions (d).

imaging and cell imprints of very thin peripheral structures were visualized, illustrating its usefulness as a thin film pH sensor (Fig. 4).

3.2. Sensor performance

Through non-linear curve fitting the pK_a was calculated to be 6.99 [27], which is in agreement with previously published results where pK_a is lowered by 0.53 pH units for each covalent attachment for the covalently bound HPTS compared to in solution (p$K_a \sim 7.3$) [28]. A repeatability experiment flanked by calibrations is shown in Fig. 2. The performance of the sensor was evaluated by implementing four parametric time-dependent sigmoidal calibrations on the responses before and after the repetitions [27]. The precision according to IUPAC using pooled S.D. ($n = 8$) was calculated to be pH ±0.0029 for the optode (±0.0061 without time correlation) compared to ±0.0021 for the electrode. The accuracy however, was much better for the optode using pH 6.641 and 7.742 as the true values initially determined by the electrode. The bias for the optode was −0.0008 (+0.0120 uncorr.) for pH 6.641 and +0.0013 (−0.0245 uncorr.) for pH 7.742 compared to +0.0013 and −0.014 respectively, for the electrode. Thus, the somewhat deprived accuracy and imprecision of the electrode is clearly limiting the performance of the optode as the values from the reference electrode are used as correct pH values for the levels in the optode calibrations. The response time (0–95%) was 100 s between pH 6.641–7.742 and the reverse response (95–0%) was 80 s. We define the operational lifetime as the time it takes for the sensor to reach a resolution (±one S.D.) of 0.01 pH units between 6.641 and 7.742. The operational lifetime was calculated to be 8 h based on linear extrapolation of the loss of levels from the first repetition to repetition 4 (Fig. 2). During the microscope measurements photobleaching becomes much more pronounced especially at high magnification and the operational lifetime is considerably less.

3.3. Photoacidity of the covalently attached HPTS

Several fluorescent compounds are photoacidic, i.e. the fluorophore is more acidic in its electronically excited state than in its ground state [29]. Typically, the pK_a of excited photoacidic compounds is 6–7 pH units lower than in the ground state [30]. In essence, observed photoacidic properties of HPTS are fundamentally associated with solvent relaxation and the acceptance of protons by protic solvents (hydrogen bonding) [31,32]. A previous study showed that HPTS immobilized by ionic interactions with TOA^+ in ethylcellulose severely decreased the photoacidity of the probe [27], likely due to a more hydrophobic and restricted environment as an ionpair with TOA^+ in ethyl cellulose. The matrix scans performed (Fig. 3) on the covalently attached HPTS clearly show that the covalently attached dye has maintained all of its photoacidic properties i.e. there are no change in blue emission after pH alterations around 430–440 nm (Fig. 3c) as the ionically immobilized fluorophore showed [27]. This can probably be explained by the fact that the film used in this study is more hydrophilic and more proton accepting due to the unconnected primary amines in the sensing film. To some extent this feature might also be elucidated from the lack of ionic interactions compared to films based on hydrophobic counter ions. Ionic interactions can possibly reduce the electron donating properties of the triply sulfonated pyrene ring to the hydroxyl group, hence stabilizing the acid form of HPTS, which might be part of the severely reduced photoacidity in such sensors compared to the covalently attached pH sensor presented here.

3.4. Optode film manufacturing considerations

Even though the sensor presented here has a quick response, unrivaled accuracy and provide an excellent platform to grow and study cells on, it is also associated with some technical difficulties that ought to be mentioned here. The over all yield was acceptable (14.5%; $n = 3$) considering the number of steps in the synthesis of amino cellulose acetate. However, the resulting solid product becomes insoluble after storage [23] and needs to be dissolved immediately after synthesis. To avoid insoluble matter to hamper the film forming processes, the solution was heated to 70 °C during sonication for 5 min before coating or mixing with the chlorinated dye. The treatment efficiently removed clusters that build up over time in the DMSO solution in room temperature. Unfortunately, such treatments also changed the viscosity, indicating shortening of the chain length by cleavage. Initially the film forming properties of the amino cellulose acetate solution was excellent but became gradually worse after repeated heating/sonication cycles over time (i.e.

weeks). Possibly just heating the sample to 70 °C without sonication could prevent this phenomenon.

Chlorination using PCl_5 has been criticized for being harsh and associated with many possible side reactions, especially in combination with DMF [33]. We found this reaction route initially very effective and reaction between the dye and cellulose material was visualized by the naked eye and completed within seconds (note: without addition of pyridine). Amino cellulose material could be stained at a restricted site by simply pinching the plastic material with a capillary filled with the reactive dye. However, repeating the complete chlorinating procedure (after a month), i.e. preparing a new batch of chlorinated HPTS in DMF, did not give the same pronounced visual effect. We suspect the chlorination efficiency to be significantly reduced for PCl_5 after first time use since the substance is hygroscopic. HPTS chlorinated in acetone was investigated by electrospray mass spectrometry to test an alternative chlorination pathway of the dye and to confirm the chlorination efficiency of the specific batch of PCl_5. The mass spectra show that HPTS molecule (Fig. S1; supporting information) was most commonly chlorinated at a single sulfonic site followed by two and three chlorinations, indicating that the right conditions for an efficient chlorination are fulfilled in even less efficient SN2 solvents (Fig. S1; supporting information). There was no trace of unchlorinated dye present in the dye solution (see Fig. S1; supporting information). We suggest that the efficient coupling seen initially, using fresh PCl_5 in DMF, was caused by a higher degree of chlorination of the sulfonic sites of the dye molecule. We also found that the addition of a base during the coupling between the dye and cellulose material (typically $10\times n$ mol HPTS-Cl) hampered the response from the sensors. A similar reaction scheme based on PBr_5, DMF and pyridine has been used for covalent immobilization of an oxygen sensor to glass beads [34]. In that sensing scheme the silanol groups are negatively charged and the dye positively charged and thereby benefited by an addition of a base that increase the nucleofilicity of the silanol groups as well as attractive forces between the two reactive species in the solution. The net charge of the primary amine on amino cellulose acetate, however, is most likely neutrally charged under basic conditions in aprotic polar solvents such as DMF i.e. there is no or little electrostatic attraction between the dye and substrate leading to decreased coupling efficiency. Moreover, addition of a base will increase the nucleofilicity of the deprotonated hydroxyl group of the HPTS molecule that could cause self-polymerization of the dye with a subsequent loss of pH dependent fluorescence. In addition, traces of a weak base such as pyridine ($pK_a \sim 5$ in water) might be trapped within the film and concurrently buffer the pH response from HPTS. We therefore conclude that the best sensors are synthesized without additions of pyridine.

4. Conclusions

The developed sensor showed unrivaled pH sensitivity and accuracy in the physiological range and the imaging performance was excellent as imprints of attached cells and small μm sized cell extensions were visualized after pH alterations in the extra-cellular solution. Thereby, the sensor constitutes a promising research tool for spatio-temporal studies of pH responses from neuronal cells or networks during cell growth.

Acknowledgements

The Chinese hamster ovary cells were supplied and seeded by Roger Karlsson and Ingela Lanekoff at University of Gothenburg. We thank Stefan Hulth for making the Microscope available for this study. Financial support was obtained from the Swedish Research Council (VR), the Foundation for Strategic Environmental Research (MISTRA), the Swedish Research Council for Environment, Agricultural Sciences and Spatial Planning (FORMAS).

Appendix A. Supplementary data

Supplementary data associated with this article can be found, in the online version, at doi:10.1016/j.aca.2009.01.045.

References

[1] R.Y. Tsien, M. Poenie, Trends Biochem. Sci. 11 (1986) 450.
[2] N. Stromberg, S. Hulth, Anal. Chim. Acta 550 (2005) 61.
[3] N. Stromberg, S. Hulth, Sens. Actuator B: Chem. 115 (2006) 263.
[4] J.I. Peterson, S.R. Goldstein, R.V. Fitzgerald, D.K. Buckhold, Anal. Chem. 52 (1980) 864.
[5] Z. Zhujun, W.R. Seitz, Anal. Chim. Acta 160 (1984) 47.
[6] S.G. Schulman, S.X. Chen, F.L. Bai, M.J.P. Leiner, L. Weis, O.S. Wolfbeis, Anal. Chim. Acta 304 (1995) 165.
[7] M.F. Choi, J. Photochem. Photobiol. A: Chem. 104 (1997) 207.
[8] C. Munkholm, D.R. Walt, F.P. Milanovich, S.M. Klainer, Anal. Chem. 58 (1986) 1427.
[9] G. Gabor, D.R. Walt, Anal. Chem. 63 (1991) 793.
[10] H. Szmacinski, J.R. Lakowicz, Anal. Chem. 65 (1993) 1668.
[11] R.B. Thompson, J.R. Lakowicz, Anal. Chem. 65 (1993) 853.
[12] M. Scharte, R. Porath, T. Ohms, M. Aeschlimann, J.R. Krenn, H. Ditlbacher, F.R. Aussenegg, A. Liebsch, Appl. Phys. B: Lasers Opt. 73 (2001) 305.
[13] A.J. Marshall, J. Blyth, C.A.B. Davidson, C.R. Lowe, Anal. Chem. 75 (2003) 4423.
[14] I. Sanchez-Barragan, J.M. Costa-Fernandez, A. Sanz-Medel, M. Valledor, F.J. Ferrero, J.C. Campo, Anal. Chim. Acta 562 (2006) 197.
[15] S. Hulth, R.C. Aller, P. Engstrom, E. Selander, Limnol. Oceanogr. 47 (2002) 212.
[16] E. Wang, L. Zhu, L. Ma, H. Patel, Anal. Chim. Acta 357 (1997) 85.
[17] A. Song, S. Parus, R. Kopelman, Anal. Chem. 69 (1997) 863.
[18] Q.Z. Zhu, R.C. Aller, Y.Z. Fan, Environ. Sci. Technol. 39 (2005) 8906.
[19] M. Kuhl, L.F. Rickelt, R. Thar, Appl. Environ. Microbiol. 73 (2007) 6289.
[20] S.M. Borisov, O.S. Wolfbeis, Anal. Chem. 78 (2006) 5094.
[21] S.M. Barnard, D.R. Walt, Nature 353 (1991) 338.
[22] J. Ji, Z. Rosenzweig, Anal. Chim. Acta 397 (1999) 93.
[23] J. Tiller, P. Berlin, D. Klemm, J. Appl. Polym. Sci. 75 (2000) 904.
[24] C.L. McCormick, T.R. Dawsey, J.K. Newman, Carbohydr. Res. 208 (1990) 183.
[25] P. Berlin, D. Klemm, J. Tiller, R. Rieseler, Macromol. Chem. Phys. 201 (2000) 2070.
[26] P. Berlin, D. Klemm, A. Jung, H. Liebegott, R. Rieseler, J. Tiller, Cellulose 10 (2003) 343.
[27] A. Hakonen, S. Hulth, Anal. Chim. Acta 606 (2008) 63.
[28] H. Offenbacher, O.S. Wolfbeis, E. Furlinger, Sens. Actuators 9 (1986) 73.
[29] T. Forster, Naturwissenschaften 36 (1949) 186.
[30] T.H. Tran-Thi, T. Gustavsson, C. Prayer, S. Pommeret, J.T. Hynes, Chem. Phys. Lett. 329 (2000) 421.
[31] T.H. Tran-Thi, C. Prayer, P. Millie, P. Uznanski, J.T. Hynes, J. Phys. Chem. A 106 (2002) 2244.
[32] O.F. Mohammed, J. Dreyer, B.Z. Magnes, E. Pines, E.T.J. Nibbering, Chemphyschem 6 (2005) 625.
[33] G. Blotny, Tetrahedron Lett. 44 (2003) 1499.
[34] M.P. Xavier, D. Garcia-Fresnadillo, M.C. Moreno-Bondi, G. Orellana, Anal. Chem. 70 (1998) 5184.

Paper IV

Talanta 80 (2010) 1964–1969

Contents lists available at ScienceDirect

Talanta

journal homepage: www.elsevier.com/locate/talanta

A high-performance fluorosensor for pH measurements between 6 and 9

Aron Hakonen*, Stefan Hulth

Department of Chemistry, University of Gothenburg, SE-412 96 Göteborg, Sweden

ARTICLE INFO

Article history:
Received 21 August 2009
Received in revised form 16 October 2009
Accepted 23 October 2009
Available online 5 November 2009

Keywords:
pH
Optode
6,8-Dihydroxypyrene-1,3-disulfonic acid
DHPDS
Photoacidity
Fluorescence ratio

ABSTRACT

This study presents a high-performance ratiometric pH optode based on the fluorophore 6,8-dihydroxypyrene-1,3-disulfonic acid (DHPDS). The two pH-sensitive terminal hydroxy groups of DHPDS facilitated dual excitation/dual emission (F_1: $\lambda_{1,ex}$ = 420 nm, $\lambda_{1,em}$ = 462 nm; F_2: $\lambda_{2,ex}$ = 470 nm, $\lambda_{2,em}$ = 498 nm) properties for ratiometric ($R_{F1,F2} = F_1/F_2$) normalization of sensor signal. The sensor demonstrated an exponentially decreasing ratiometric response with increasing pH, with a linear correlation (R^2 = 0.9936) between $^{10}\log(R_{F1,F2})$ and pH within the pH interval 6–9. Precision determined as the IUPAC pooled standard deviation for the pH values 6.00, 7.01 and 9.01, was 0.0057 pH units for the fluorosensor and 0.0054 for a commercially available pH electrode used for comparison. Between the end-points of calibration at pH 7.01, the precision of the sensor was 0.0037 pH units. Effects from changes in ionic strength (I_{tot}, 10–700 mM) were more pronounced for the electrode, with a linear (R^2 = 0.9976) increase in response (δE/δpH) with increasing I_{tot}. The DHPDS-based fluorosensor, however, retained sensitivity ($\delta^{10}\log(R_{F1,F2})/\delta$pH = 0.8024 ± 0.0145), though with an overall increase in ratiometric signal with increasing I_{tot}. The preserved sensitivity despite changes in ionic strength was possibly a consequence from the dual photo-acidic properties of DHPDS. Analytical characteristics of immobilized DHPDS therefore not only facilitated high-performance measurements over a wide pH range, but also opened for straightforward simultaneous measurements of pH and ionic strength.

1. Introduction

The activity of hydrogen ions is a master analytical parameter to understand and predict electron transfer and general dynamics during multiple reactions in natural environments [1]. Consequences and feedbacks from changes in pH may have local, regional and global importance. For example, pH of seawater has received particular attention in current characterizations of the oceanic response to anthropogenic emissions of CO_2, in part due to the recently demonstrated acidification of the world's oceans [2]. Although ion-selective electrodes are commonly used for pH measurements [3,4], optical sensors (optodes) have since 1980 frequently been used for pH measurements [5–9]. Optodes are also suitable for high-resolution imaging of pH distributions in complex environments such as aquatic sediments [5,10,11], and there are exciting possibilities for multi-parameter and multi-analyte sensing [9,12–14].

The dynamic range for quantification using optical sensors is normally set by the dependence between the associated and dissociated form of the indicator, and restrictions inherent to the optical instrumentation used during measurements (e.g. [15,16]). For conjugate pairs of acid–base compounds, one compound is often considered undetectable in the presence of the other when relative color intensity is less than ~one-tenth. These traditional limits also tend to fix the dynamic range of fluorescence based sensors to ±1 pH units surrounding the apparent pK_a (pK'_a) of the acid–base indicator [17]. In response to biological activities such as intense photosynthesis, bioturbation and organic matter mineralization, pH of natural environments frequently varies by several pH units even on short time-scales [3,18,19]. Such large variation (>2 pH units) in pH is likely to hamper the analytical performance of acid–base indicators and optical sensors in general. Further, an often conveyed limitation of optical sensors is the sensitivity to changes in ionic strength (I_{tot}) of the sample matrix [20]. According to the Debye–Hückel theory, optical sensors for pH normally suffer from a decreased pK'_a with increasing I_{tot} [21]. Despite theoretical and model predictions, there are few, if any, investigations specifically designed to experimentally verify and quantitatively compare the relative dependence to changes in I_{tot} between optodes and ion-selective electrodes available for pH measurements. Overall, the analytical performance of optical pH sensors is due to progressive improvements considered comparable to that of pH electrodes (e.g. [22,23]).

8-Hydroxypyrene-1,3,6-trisulfonate (HPTS; Fig. 1) is one of the most widely used fluorescence indicators for pH measurements in near-neutral samples [8,24,25]. HPTS is a fluorophore used not only

* Corresponding author. Tel.: +46 31 772 2878; fax: +46 31 772 2785.
E-mail address: hakonen@chem.gu.se (A. Hakonen).

0039-9140/$ – see front matter © 2009 Elsevier B.V. All rights reserved.
doi:10.1016/j.talanta.2009.10.055

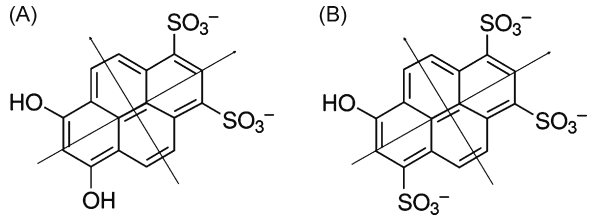

Fig. 1. Chemical structures of (A) 6,8-dihydroxypyrene-1,3-disulfonic acid (DHPDS) and (B) 8-hydroxypyrene-1,3,6-trisulfonate (HPTS) (pH > pK_a of the sulfonate groups, i.e. pH > 1). The arrows represent through atom (excited energy state ^1L_a, arrow through atoms) and through bond (^1L_b) excitation light directions.

to quantify pH in various solutions, but also in more sophisticated applications such as cellular imaging [26] and imaging optodes for both microscopic [23] and macroscopic use [5,11]. General patterns of HPTS fluorescence are essentially governed by the protonation/deprotonation equilibrium of the hydroxyl hydrogen and the photo-acidic properties of HPTS [22]. HPTS is normally considered highly photo-acidic, i.e. the fluorophore is more acidic in the electronically excited state (HPTS*; Fig. 1) than in the ground state [27]. Frequently, pK_a' of excited photo-acidic compounds is 6–7 pH units lower than in the ground state. For example, pK_a' of HPTS in solution is ~7.3 while in excited state it can be as low as 1.0 [28]. Photo-acidic properties therefore govern the dual excitation (~405 and 450 nm) single emission (~520 nm) ratiometric sensing scheme observed for HPTS in solution. Further, HPTS have intrinsic ratiometric properties that provides signal normalization and amplification. The ratiometric approach has been demonstrated to be as effective as lifetime measurements to reduce artifacts [29].

In contrast to the wide range of pH measurements that include HPTS, there are only few studies that have utilized the di-hydroxylated analogue 6,8-dihydroxypyrene-1,3-disulfonate (DHPDS; Fig. 1) [30,31]. DHPDS shares most of the advantageous properties of HPTS, such as high quantum yield, excellent water solubility, ratiometric properties and lack of toxicity. The objective of this study was to reassess the suitability of DHPDS as a fluorophore for pH measurements and to experimentally evaluate fluorescence properties of DHPDS immobilized in a sensing membrane. As the structure of DHPDS includes two hydroxyl groups with overlapping (within 2 pH units) pK_a'-values (7.33 and 8.53; [24]), we hypothesize that, while retaining essential spectroscopic signatures, the analytical characteristics of the two acidic protons provide the basis for a significantly improved sensor dynamic range compared to, for example, HPTS-based sensors.

2. Experimental

2.1. Materials

The sensing film was prepared in a similar manner as was originally described in [10]. A prefabricated transparency film (Hewlett Packard, HP C3835A) consisting of a 100 μm thick polyester foil with a 10 μm cellulose acetate coating was used for the immobilization of DHPDS. In brief, the sensing foil was immersed over night in a high ionic strength (NaCl 1.0 M) solution with 75 μM of the fluorophore 6,8-dihydroxypyrene-1,3-disulfonic acid (DHPDS; >98%, Fluka). The high ionic strength is intended to provide thin double layers, which allows short range fluorophore–foil interactions. These close interactions are the basis for the immobilization mechanism through, e.g. hydrogen bonds, ion-dipole and hydrophobic interactions. The cellulose acetate provides a convenient platform for DHPDS association by these interactions as the ζ-potential is close to zero for ionic strength above 3 mM [32]. Before use, the sensor film was treated in Milli-Q water (deionized water further purified by a Milli-Q system, Millipore Corp., to a resistivity of >18 MΩ cm^{-1}) for 12 h and finally immersed in a sample-like matrix for 12 h. Phosphate buffers ($[H_3PO_4]_{tot}$ = 4 mM) were prepared from appropriate amounts of 40 mM NaH_2PO_4 and Na_2HPO_4 (p.a., Merck) stock solutions in Milli-Q water. Total ionic strength of solutions was adjusted by proper additions of NaCl (p.a., Merck). Buffer solutions for calibration were certified traceable to NIST Standard Reference Material (pH 6.00, 7.01 and 9.01 at 20 °C, Merck).

2.2. Instrumentation

The sensor with immobilized DHPDS was mounted onto a plexiglass support and secured in a plastic cuvette (3 mL), placed in the spectrofluorometer (Fluoromax-3, SPEX Instruments Int., Inc.). To minimize background noise and reflection from incident light, the angle of incidence for the excitation light was set to 30°. Excitation and emission scans were performed at 1.00 nm resolution, 0.25 s time of integration and slit widths corresponding to 2.00 nm bandpass. Matrix scans (Fluoromax-3, SPEX Instruments Int., Inc.) at pH 9.01 and 6.00 were prior to experiments divided to determine the optimum pairs of ratiometric wavelengths for this particular setup. Here, F_1 ($\lambda_{1,ex}$ = 420 nm, $\lambda_{1,em}$ = 462 nm) and F_2 ($\lambda_{2,ex}$ = 470 nm, $\lambda_{2,em}$ = 498 nm) were used for ratiometric ($R_{F1,F2} = F_1/F_2$) detection of fluorescence. The pH electrode (model 6.0232.100, 780 pH meter; Metrohm Ltd.) was calibrated in NIST buffers by a two-point calibration procedure (pH 6.00 and 9.01). Temperature was kept constant (20 ± 1 °C) during all experiments.

2.3. Procedures

Repeatability of the DHPDS-based sensor was analytically evaluated to obtain a quantitative measure of sensor precision within the pH interval 6–9. The repeatability experiment was designed to include four replicates at the end-points of calibration (i.e. two replicates at pH 6.00 and two at pH 9.01) and four at the intermediate pH 7.01 (i.e. n_{tot} = 8). Calibrations were performed before and again repeated after sample measurements (i.e. two-point calibrations were performed at pH 6.00 and 9.01). The ratiometric signal, $R_{F1,F2}$, was linearized ($^{10}\log(R_{F1,F2})$) for visualization purposes and to simplify quantifications. Time-dependent calibration functions were applied on the linearized response function to provide a unique set of calibrations for each individual repetition [22,33]. Replicate measurements were analytically evaluated for repeatability according to IUPAC's definition of pooled standard deviation [34]. The repeatability experiment encompassed 11 consecutive ratiometric measurements, including calibrations and replicate samples. Measurements were performed using NIST traceable standards, 5 min equilibrium time, 0.5 s time of integration.

To evaluate the sensitivity towards changes in ionic strength, the response from the DHPDS-based optical sensor was compared to that of a commercially available pH electrode (model 6.0232.100, 780 pH meter; Metrohm Ltd.). Comparisons were made at pH 6.246 and 8.026 in phosphate buffers ($[H_3PO_4]_{tot}$ = 4 mM) in which the ionic strength was adjusted to 10, 355 and 700 mM with appropriate additions of NaCl (p.a., Merck).

For comparison, the fluorescence response of dissolved DHPDS and HPTS was individually evaluated by titrating 3 μM of each fluorophore in 0.0667 M phosphoric acid with 2 M NaOH. Photobleaching of DHPDS and HPTS was assessed using 3 μM of each fluorophore in NIST buffer (pH 7.00). The experiment was performed in the mode of constant illumination (excitation at 420 and 470 nm for DHPDS, and at 405 and 455 nm for HPTS) for 2 h.

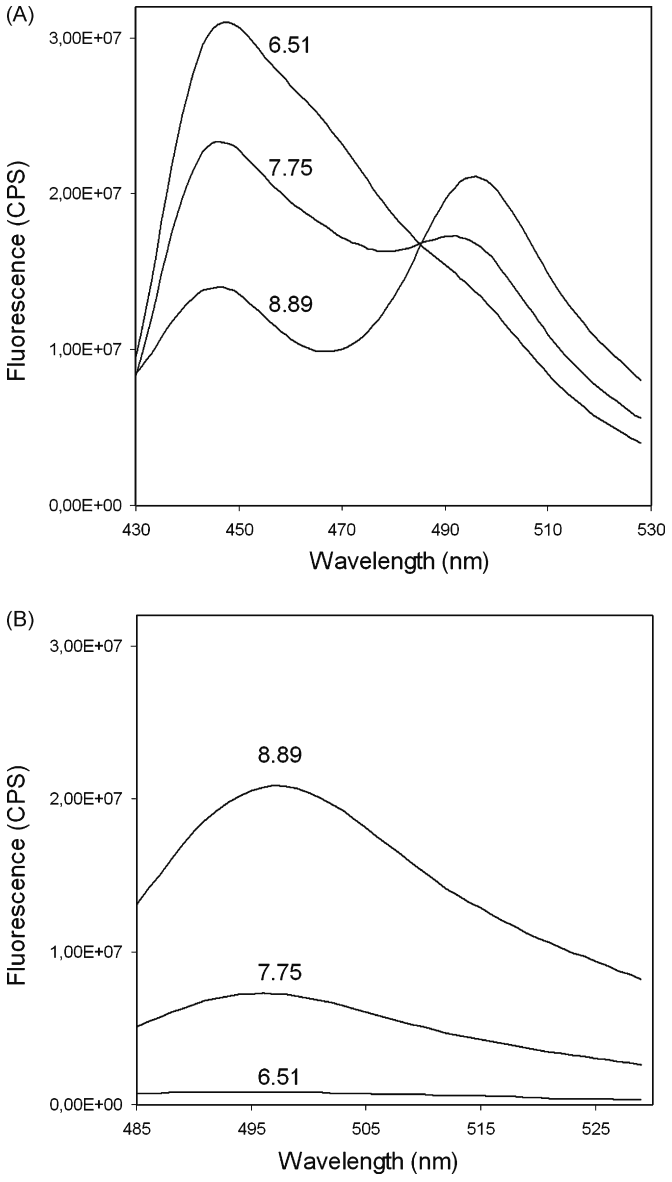

Fig. 2. Emission spectra of DHPDS immobilized in the sensor film at pH 6.51, 7.75 and 8.89 (I_{tot} = 700 mM). Excitation was performed at 420 nm (A) and 470 nm (B). Excitation at 420 nm demonstrated an isosbestic point at ~485 nm.

3. Results and discussion

3.1. General sensor characteristics and sensor response

Fluorescence matrix scans (excitation and emission) were divided to evaluate and optimize pairs of wavelengths for maximum relative response in fluorescence with changing pH. Within the excitation range 340–480 nm and the corresponding emission range 430–550 nm, F_1 ($\lambda_{1,ex}$ = 420 nm, $\lambda_{1,em}$ = 462 nm) and F_2 ($\lambda_{2,ex}$ = 470 nm, $\lambda_{2,em}$ = 498 nm) were associated with the largest relative response. These pairs of excitation and emission wavelengths (F_1 and F_2) were therefore consecutively used for ratiometric ($R_{F1,F2} = F_1/F_2$) normalization of sensor signal (Fig. 2). Procedures of dual excitation and dual emission were used to significantly increase the dynamic range and sensitivity of measurements. Immobilized DHPDS demonstrated double emission maxima at ~450 and ~500 nm (excitation at 420 nm), and a single emission at ~500 nm as a response to the excitation at 470 nm (Fig. 2). The fluorescence observed at 450 nm (excitation

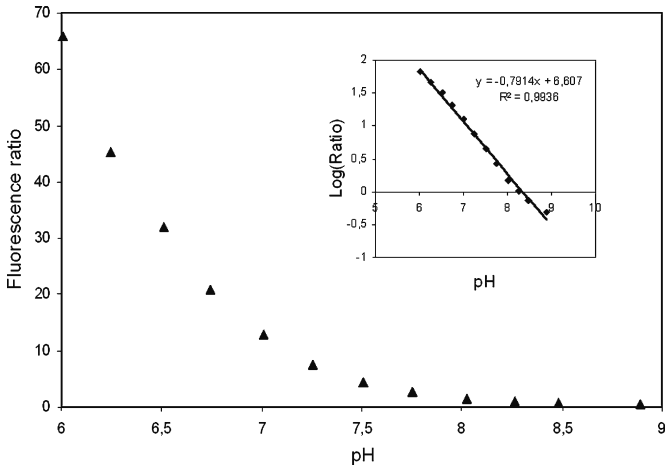

Fig. 3. The ratiometric response ($R_{F1F2} = F_1/F_2$) of immobilized DHPDS as a function of pH. Inserted is the logarithmic response from pH 6 to 9. I_{tot} = 700 mM.

at 420 nm; F_1) decreased, while the fluorescence at 500 nm (excitation 470 nm; F_2) increased with increasing pH. Maximum relative response used for quantification of pH (from the matrix scans) did not exactly match the maximum fluorescence obtained following single-wavelength excitation at 420 nm ($\lambda_{max,em1}$ = 447 nm) and 470 nm ($\lambda_{max,em2}$ = 495 nm; Fig. 2), which is not uncommon during fluorescence detection [35]. The relatively large shift observed for excitation at 420 nm ($\lambda_{1,em}$ = 462 nm rather than 447 nm; Fig. 2) may be caused by a broad overlap of energy levels associated with the fluorescence measured. The ratiometric response ($R_{F1,F2}$; I_{tot} = 700 mM) decreased exponentially from pH ~ 6 ($R_{F1,F2} \approx 65$) to pH ~ 8.9 ($R_{F1,F2} \approx 0.5$) (Fig. 3), with a significant linear correlation between the logarithmic signal ($\delta^{10}\log(R_{F1,F2})$) and pH ($(\delta^{10}\log(R_{F1,F2})/\delta\text{pH}) = -0.7914$; $R^2 = 0.9936$; $n = 12$). Similarly, as was also observed for immobilized DHPDS, the ratiometric response of dissolved DHPDS followed a decreasing exponential function with pH (Fig. 4). The logarithmic ($\delta^{10}\log(R_{F1,F2})$) response of dissolved DHPDS from three independent titrations followed a linear function ($(\delta^{10}\log(R_{F1,F2})/\delta\text{pH}) = -1.01$; $R^2 = 0.9974$; $n = 22$) between pH ~ 5 and pH ~ 10. For comparison, the logarithmic response from a similar titration of HPTS in solution was linear between pH 5 and 8, with a slope ($\delta^{10}\log(R_{F1,F2})/\delta\text{pH}$) of −0.82

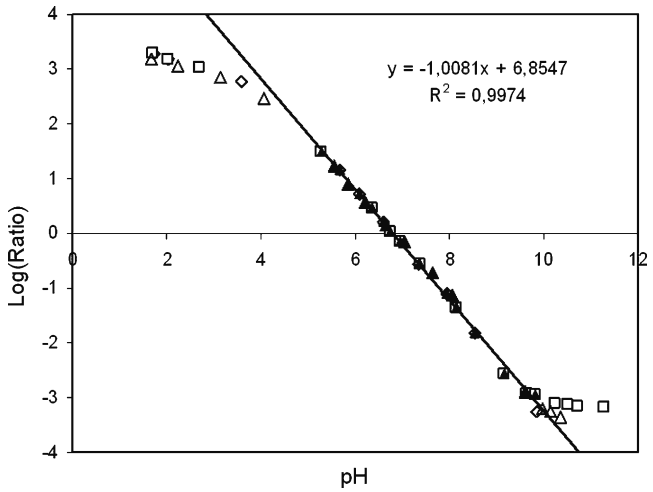

Fig. 4. Logarithmic sensor response ($\delta^{10}\log(R_{F1,F2})$) as a function of pH for 3 μM DHPDS in 0.067 M phosphoric acid titrated with 2 M NaOH (three independent titrations; n_{tot} = 41). Black triangles denote data points used to calculate the linear correlation (n = 22).

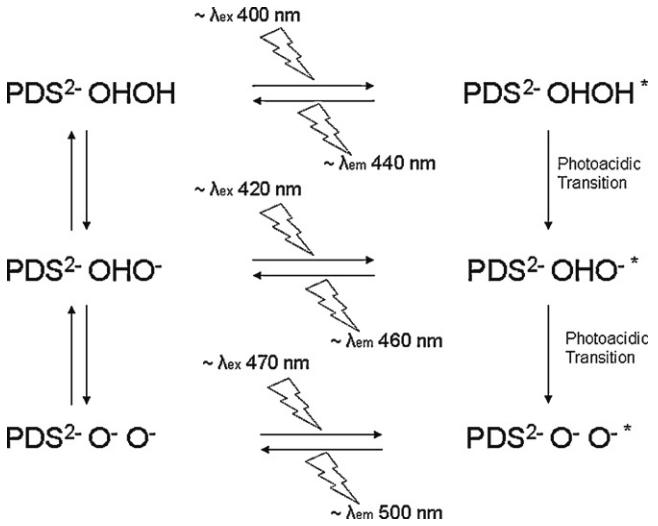

Fig. 5. Suggested proton dynamics for DHPDS. PDS^{2-} denotes the pyrene-disulfonate group to which the hydroxyl groups with the two acidic protons are attached. (*) Indicates electronically excited DHPDS.

($R^2 = 0.9974$; $n = 7$) (not shown). The response of dissolved HPTS and DHPDS not only indicated a significantly larger (close to 2 pH units) dynamic range of DHPDS compared to HPTS. The steeper slope of the response function also suggested an improved sensitivity (>20%) for DHPDS.

Overall, the response of an optical pH sensor is determined by the acid–base equilibria of the immobilized dye, with a classical sigmoidal calibration having an inflection point that corresponds to the pK_a' of the immobilized indicator [10]. The analytical sensitivity is most pronounced close to this pK_a' where the derivative (δ(signal)/δ(pH)) is maximized. An apparent dissociation constant of $10^{-6.4}$ (i.e. $pK_a' = 6.4$) was observed for HPTS immobilized onto cellulose acetate in seawater [10]. As the pH of open seawater is slightly above 8, and even higher in environments of intense primary production (e.g. [19]), the analytical performance of HPTS-based sensors is normally hampered for use in such systems (e.g. [5]). The large dynamic range of DHPDS-based sensors observed in this study, including pH values up to ~9, support the preferential use of DHPDS rather than HPTS for pH measurements in e.g. seawater.

Based on the obtained fluorescence response, a simplified scheme for proton and excited state dynamics of DHPDS is presented (Fig. 5). Fluorescence transitions are not infinitely narrow and there are often significant overlaps between excitation and emission bands. The closely coupled energy levels corresponding to excitations at 400 and 420 nm are particularly likely to be associated. At 500 nm (excitation at 420 nm), the fluorescence of DHPDS in solution was more pronounced (not shown) compared to that observed for DHPDS immobilized onto the sensor film (Fig. 2A). This observation indicated that immobilization of DHPDS onto the sensor support caused a reduced photoacidity by obstructing proton dynamics. The effect following immobilization was, however, not as pronounced as previously demonstrated for HPTS where the complete photoacidity was removed upon immobilized in ethyl-cellulose [22]. Excitation and emission properties for DHPDS demonstrated in this study also support that excited state dynamics of DHPDS may include a double deprotonation (Fig. 5), as 400 nm excitation at pH < 6.5 resulted in a substantial fluorescence at 500 nm (data not shown).

The photobleaching experiment demonstrated that upon constant illumination for 2 h, the emission decreased by 8.5% for DHPDS and 1.5% for HPTS. The corresponding ratiometric signals changed by 0.4% for both DHPDS and HPTS. The combination of ratiometric normalization and time-correlated calibration protocols would thus completely cancel out this potential artifact as well as the plausible leaching of the fluorophore.

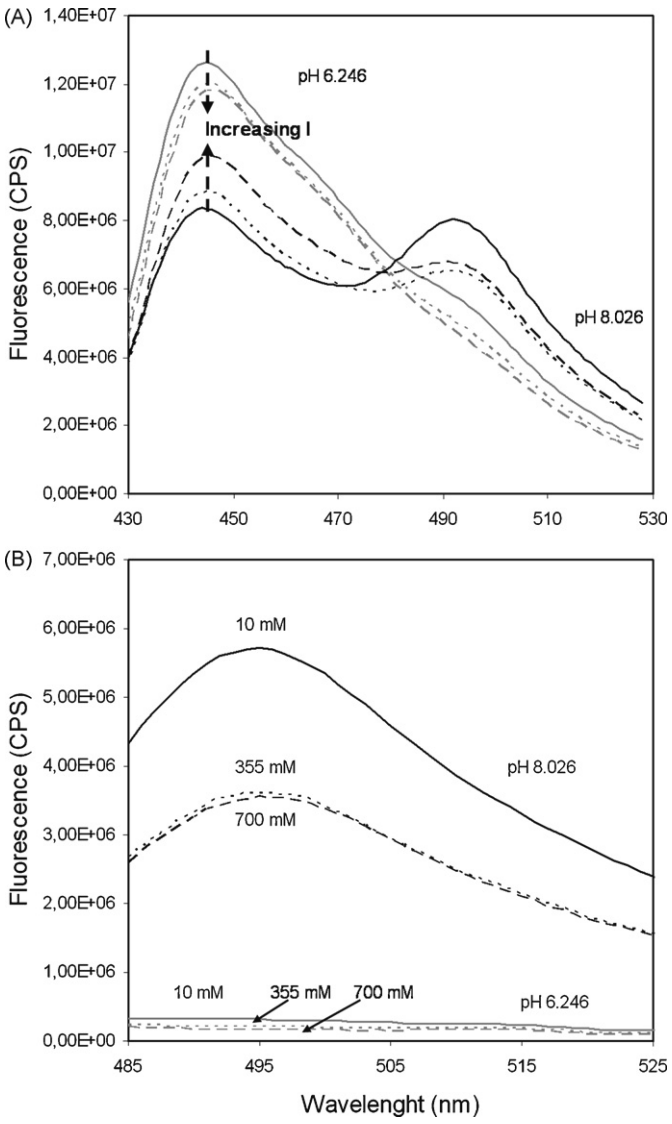

Fig. 6. Emission spectra of immobilized DHPDS at 10 mM (solid), 355 mM (dotted) and 700 mM (dashed) ionic strength. Measurements were performed at pH 8.026 (black) and 6.246 (grey) using excitation at 420 nm (A) or 470 nm (B).

3.2. Effects of ionic strength

Fluorescence spectra for the sensor exposed to pH 6.246 and 8.026 in solutions of 10, 355 and 700 mM total ionic strength (I_{tot}) are shown in Fig. 6. Fluorescence intensity at 450 nm (excitation at 420 nm) was shifted in opposite directions at low and high pH with increasing ionic strength (Fig. 6A). At pH 6.246, the fluorescence decreased, while at pH 8.026 measured fluorescence increased with increasing I_{tot}. In contrast, emission at 500 nm (excitation at 420 nm) decreased progressively with increasing I_{tot} for both pH values. This experimental observation is quite opposite to the Debye–Hückel theory that under conditions of high pH would predict a decrease in pK_a'. As a consequence, fluorescence emission would be significantly reduced with increasing I_{tot} [21]. We suggest that a decreased solvent acceptance of protons, with a subsequent reduction in photoacidity, caused the increase in flu-

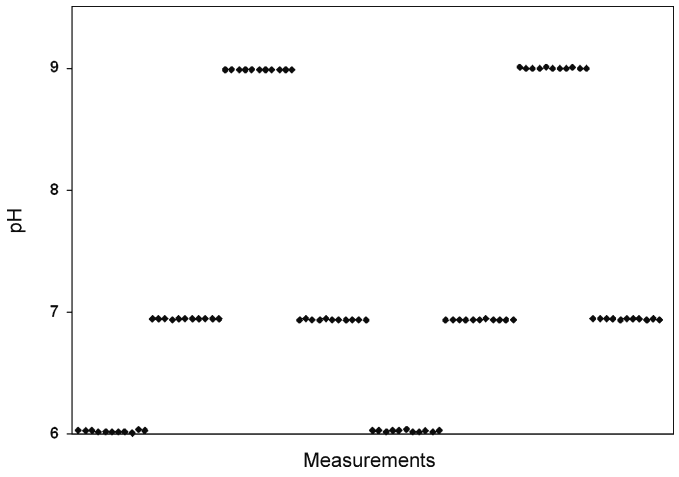

Fig. 7. Repeatability of the DHPDS-based sensor at pH 6.00, 7,01 and 9.01 ($n = 11$). The pooled standard deviation (IUPAC) was 0.0057 ($n = 8$). Time between each data point was 5 s, and the time between sampling occasions was 5 min.

orescence observed at ~450 nm with increasing I_{tot}. A reduced photoacidity may also explain the decrease in F_1 ($\lambda_{1,ex} = 420$ nm, $\lambda_{1,em} = 462$ nm) with increasing I_{tot} observed at pH 6.246. The overlap in energies associated with the excitation at 420 and 400 nm is likely more decoupled as photoacidity decreases, i.e. the reduction of fluorescence observed at 462 nm (excitation at 420 nm; Fig. 6) is generated by the first photo-acidic transition of DHPDS (Fig. 5).

Optodes are normally considered highly sensitive to changes in I_{tot} as the solute activity coefficient of the indicator and the surface potential are partly controlled by changes in I_{tot} (e.g. [20,21]). Further, properties of the surface itself are vital for local fluorescence via acid-base characteristics and changes in the ζ-potential [20]. In this study, samples of variable ionic strength ($I_{tot} = 10$, 355 and 700 mM) demonstrated that the DHPDS-based pH fluorosensor was significantly less sensitive to changes in I_{tot} than the commercially available electrode used for comparison. While the optode seemed to maintain the sensitivity of the ratiometric signal ($\delta^{10}\log(R_{F1,F2})/\delta\text{pH} = 0.8024 \pm 0.0145$) within the pH interval 6.246–8.026, there was a positive linear correlation in electrode response to I_{tot} ($R^2 = 0.9976$; $n = 6$). For comparison, the linear correlation (R^2) between I_{tot} and pH was 0.065 ($n = 6$) for the optode. The quantitative errors related to changes in I_{tot} (10–700 mM) rather than pH correspond to 0.322–0.338 pH units for the optode and 0.528–0.725 for the electrode, respectively. However, as a solution of NaCl was used to moderate ionic strength of samples, effects associated with changes in I_{tot} may at least partly be caused by the linear increase in sodium concentration induced by NaCl additions. Nevertheless, the comparably low sensitivity towards changes in I_{tot} demonstrated for the DHPDS-based pH sensor may open up for simultaneous measurements of pH and ionic strength over wide ranges using DHPDS-based optical sensors. Ideally, fluorescence at the isosbestic point ($\lambda_{ex} = 420$ nm, $\lambda_{em} = 485$ nm, Fig. 2) where sensor response is insensitive to pH, could be used for such dual measurements. Unfortunately, there was only a small response to changes in ion strength at the isosbestic point (Fig. 6).

3.3. Analytical performance

The precision (IUPAC's definition of pooled standard deviation; $n = 8$) of the DHPDS-based optical sensor was within the pH interval 6–9 comparable to that of the electrode used for comparison (Fig. 7). With a linear time-dependent two-point calibration, the precision over three pH values (6.00, 7.01 and 9.01) was 0.0057 pH units for the optical sensor, compared to 0.0054 for the electrode. The accuracy, defined as mean systematic deviation (absolute value) from the NIST pH values, was 0.037 for the optode ($n = 8$) and 0.023 for the electrode ($n = 8$), respectively. Between the end-points of calibration at pH 7.01, the precision of the optode was 0.0037 pH units ($n = 4$). Using a similar experimental set-up, a precision of 0.0029 (IUPAC, $n = 8$) was demonstrated for a HPTS-based ratiometric fluorosensor between pH 6.64 and 7.76 [23]. Optode standardizations were made in relation to a commercially available pH electrode using multi-point ($n = 4$–7) time-dependent sigmoidal calibrations. In the present study, however, NIST buffers were exposed directly to the optode for calibrations and measurements to eliminate limitations inherent to the analytical performance of the electrode. Calibrations were made using time-dependent linear functions linked within a two-point calibration. The comparably large systematic errors (0.037) of the optode response were likely explained by insufficient exchange of sample volume during the analytical procedure, and the dead volume associated with sensor configuration.

Further developments of the DHPDS-based sensing scheme are suggested to include metal enhanced fluorescence (MEF) and plasmonics to further enhance fluorescence characteristics [36]. Properly arranged, the sensor system would benefit from surface plasmon enhancement and lossy surface wave quenching as the fluorophore moves toward the plasmon active nanoparticles [35]. Additionally, constructive scattering effects have the potential to further enhance the signal.

4. Conclusions

DHPDS is a double excitation and double emission (F_1: $\lambda_{1,ex} = 420$ nm, $\lambda_{1,em} = 462$ nm; F_2: $\lambda_{2,ex} = 470$ nm, $\lambda_{2,em} = 498$ nm) ratiometric ($R_{F1,F2} = F_1/F_2$) fluorophore with similar analytical characteristics as HPTS. Due to the dual photo-acidic properties of immobilized DHPDS, the fluorescence dynamic range encompassed pH 6–9, i.e. the range for pH measurements was significantly larger for the DHPDS-based sensor than that previously observed for HPTS-based optical sensors. The precision of the DHPDS sensor was 0.0057 over the investigated pH range. The sensitivity to changes in ionic strength was significantly better for the DHPDS sensor than that of a commercially available pH electrode used for comparison. The DHPDS-based sensor retained sensitivity between 10 and 700 mM ionic strength.

Acknowledgements

Financial support was obtained from the Swedish Research Council (VR), the Foundation for Strategic Environmental Research (MISTRA), the Swedish Research Council for Environment, Agricultural Sciences and Spatial Planning (FORMAS), and the Lovén Centre for marine infrastructure (University of Gothenburg). Thanks to Erik Mattsson for his substantial contribution in the rediscovery of DHPDS.

References

[1] S. Sørensen, Biochemische Zeitschrift 21 (1909) 131–200.
[2] K. Caldeira, M.E. Wickett, Nature 425 (2003) 365.
[3] W.J. Cai, C.E. Reimers, Limnology and Oceanography 38 (1993) 1762–1773.
[4] N.P. Revsbech, B.B. Jorgensen, Advances in Microbial Ecology 9 (1986) 293–352.
[5] A. Hakonen, S. Hulth, S. Dufour, Talanta, 2009, submitted for publication.
[6] J.I. Peterson, S.R. Goldstein, R.V. Fitzgerald, D.K. Buckhold, Analytical Chemistry 52 (1980) 864–869.
[7] L.A. Saari, W.R. Seitz, Analytical Chemistry 54 (1982) 821–823.
[8] Z. Zhujun, W.R. Seitz, Analytica Chimica Acta 160 (1984) 47–55.
[9] D.A. Nivens, M.V. Schiza, S.M. Angel, Talanta 58 (2002) 543–550.
[10] S. Hulth, R.C. Aller, P. Engstrom, E. Selander, Limnology and Oceanography 47 (2002) 212–220.

[11] Q.Z. Zhu, R.C. Aller, Y.Z. Fan, Environmental Science & Technology 39 (2005) 8906–8911.
[12] S.M. Borisov, O.S. Wolfbeis, Analytical Chemistry 78 (2006) 5094–5101.
[13] S.M. Barnard, D.R. Walt, Nature 353 (1991) 338–340.
[14] J. Ji, Z. Rosenzweig, Analytica Chimica Acta 397 (1999) 93–102.
[15] T.D. Clayton, R.H. Byrne, Deep-Sea Research Part I-Oceanographic Research Papers 40 (1993) 2115–2129.
[16] A.G. Dickson, Marine Chemistry 44 (1993) 131–142.
[17] E. Bishop, in: E. Bishop (Ed.), Indicators, Pergamon, 1972, pp. 13–63.
[18] R.L. Marinelli, B.P. Boudreau, Journal of Marine Research 54 (1996) 939–966.
[19] N.P. Revsbech, B.B. Jorgensen, T.H. Blackburn, Y. Cohen, Limnology and Oceanography 28 (1983) 1062–1074.
[20] J. Janata, Analytical Chemistry 59 (1987) 1351–1356.
[21] O.S. Wolfbeis, H. Offenbacher, Sensors and Actuators 9 (1986) 85–91.
[22] A. Hakonen, S. Hulth, Analytica Chimica Acta 606 (2008) 63–71.
[23] N. Stromberg, E. Mattsson, A. Hakonen, Analytica Chimica Acta 636 (2009) 89–94.
[24] O.S. Wolfbeis, E. Furlinger, H. Kroneis, H. Marsoner, Fresenius Zeitschrift Fur Analytische Chemie 314 (1983) 119–124.
[25] O.S. Wolfbeis, Trac-Trends In Analytical Chemistry 4 (1985) 184–188.
[26] C.C. Overly, K.D. Lee, E. Berthiaume, P.J. Hollenbeck, Proceedings of the National Academy of Sciences of the United States of America 92 (1995) 3156–3160.
[27] T. Forster, Naturwissenschaften 36 (1949) 186–187.
[28] J.R. Lakowicz, Principles of Fluorescence Spectroscopy, 2nd ed., Kluwer Academic and Plenum, New York, 1999.
[29] H. Hochreiner, I. Sanchez-Barragan, J.M. Costa-Fernandez, A. Sanz-Medel, Talanta 66 (2005) 611–618.
[30] F.X. Felberbauer, J. Graf, Pflugers Archiv-European Journal of Physiology 419 (1991) 215–217.
[31] X.D. Ge, M. Hanson, H. Shen, Y. Kostov, K.A. Brorson, D.D. Frey, A.R. Moreira, G. Rao, Journal of Biotechnology 122 (2006) 293–306.
[32] I.H. Huisman, G. Tragardh, Colloids and Surfaces A-Physicochemical and Engineering Aspects 157 (1999) 261–268.
[33] N. Stromberg, S. Hulth, Analytica Chimica Acta 550 (2005) 61–68.
[34] IUPAC Compendium of Chemical Terminology, 2nd ed., International Union of Pure and Applied Chemistry, 1997.
[35] A. Hakonen, Analytical Chemistry 81 (2009) 4555–4559.
[36] J.R. Lakowicz, Analytical Biochemistry 337 (2005) 171–194.

Paper V

Anal. Chem. **2009,** *81,* 4555–4559

Plasmon Enhancement and Surface Wave Quenching for Phase Ratiometry in Coextraction-Based Fluorosensors

Aron Hakonen*

University of Gothenburg, Department of Chemistry, Kemivägen 10, SE-412 96 Göteborg, Sweden

In this study, a novel fluorescence ratiometric sensing scheme is presented. Gold nanoparticles (GNPs) were lipophilized with dodecanethiol and incorporated in the ether phase of a coextraction based ammonium sensor. The novel concept of this sensing scheme is that the analyte response involves a movement of the fluorophore toward lipophilized GNPs in an organic phase. Properly arranged, the system benefits from surface plasmon enhancement as well as increased lossy surface wave quenching as the fluorophore moves toward the GNPs. Likely constructive scattering effects are also present due to some build-up of nanoparticle clusters. The sensor configuration significantly reduced the noise level, increased the ratiometric signal, and improved the limit of detection approximately 3 orders of magnitude as compared with the optical sensor without the nanoparticles and ion-selective ammonium electrodes. Qualitative and quantitative detection limits were 1.7 and 5.7 nM, respectively. The sensing scheme is versatile and can be utilized for many other ions.

Metal-enhanced fluorescence and plasmonics have been widely explored for signal enhancement in various fluorescence sensing schemes during the past decade.[1−3] At least three metal−fluorophore interactions can be utilized for improved analytical sensitivity. Surface plasmons (SPs) are oscillating electronic excitations near the metal surface that can be produced by exposing the surface with electromagnetic radiation close to the metals resonance frequency.[1−9] For planar surfaces, fluorophore-to-metal distances of ∼10−100 nm enhances the fluorescence by surface plasmon coupled emission (SPCE).[9] Surface plasmons can generally be well-described by classical electrodynamics and correspond to Mie's solutions of Maxwell's equations.[3,9] A key explanation for enhanced fluorescence by SPs is separation of the decay rates and a consequent decrease in fluorescence lifetime.[3,10] Because fewer excited electrons return to the ground state by nonradiative processes, an increased photostability is normally attained.[3,10] Fluorescence quenching by lossy surface waves (LSWs)[10] constitutes another important short-range interaction for distances closer than ∼100 nm and becomes completely dominating below ∼10 nm.[9] A cubed quenching distance (d^3) dependence by LSWs has been shown.[11] The fundamental physics of LSWs is complex and not fully understood. Commonly, this nonradiative energy dissipation is attributed to ohmic losses within the metal as the surface wave propagates.[3,9] Additional characteristics of fluorophores in close proximity of colloidal metal surfaces includes amplification of the incident field of radiation by scattering.[3,12]

For this study, a coextraction-based ammonium sensor, originally developed by Stromberg and Hulth,[13,14] was modified and tested. The original sensor is based on a two-phase system that consists of an ether/hydrogel emulsion (oil in water). Ammonium ions diffuse into the hydrogel to the ether droplets, where they are bound to nonactin.[13] Nonactin is a cyclic, neutral crown ether that through bindings inside a hydrophilic central cavity forms complexes with several cations.[15] An 18-fold selectivity for ammonium over potassium (major interferent) has been shown for the optode (mixed solution method).[13] The positive nonactin/ammonium complex forms an ion pair with the negatively charged dye molecule Merocyanine 540 (MC540), and coextraction into the ether with sustained charge balance can occur.[16] MC540 is a solvatochromic dye that shows a substantial shift in excitation/emission properties upon change of solvent polarity.[17]

The object of this study was to incorporate lipophilized gold nanoparticles into the ether phase of the ammonium sensor and to evaluate and characterize the effects. It was predicted that there could be benefit from both SPCE and LSWs.

* To whom correspondence should be addressed. E-mail: Hakonen@chem.gu.se.

(1) Lakowicz, J. R. *Anal. Biochem.* **2001**, *298*, 1.
(2) Lakowicz, J. R. *Anal. Biochem.* **2004**, *324*, 153.
(3) Lakowicz, J. R. *Anal. Biochem.* **2005**, *337*, 171–194.
(4) Andrew, P.; Barnes, W. L. *Science* **2004**, *306*, 1002–1005.
(5) Pompa, P. P.; Martiradonna, L.; Della Torre, A.; Della Sala, F.; Manna, L.; De Vittorio, M.; Calabi, F.; Cingolani, R.; Rinaldi, R. *Nat. Nanotechnol.* **2006**, *1*, 126–130.
(6) Ray, K.; Chowdhury, M. H.; Lakowicz, J. R. *Anal. Chem.* **2007**, *79*, 6480–6487.
(7) Wark, A. W.; Lee, H. J.; Qavi, A. J.; Corn, R. M. *Anal. Chem.* **2007**, *79*, 6697–6701.
(8) Scharte, M.; Porath, R.; Ohms, T.; Aeschlimann, M.; Krenn, J. R.; Ditlbacher, H.; Aussenegg, F. R.; Liebsch, A. *Appl. Phys. B* **2001**, *73*, 305–310.
(9) Ford, G. W.; Weber, W. H. *Phys. Rep.* **1984**, *113*, 195–287.
(10) Drexhage, K. H. *Bull. Am. Phys. Soc.* **1969**, *14*, 873–&.
(11) Campion, A.; Gallo, A. R.; Harris, C. B.; Robota, H. J.; Whitmore, P. M. *Chem. Phys. Lett.* **1980**, *73*, 447.
(12) Sokolov, K.; Chumanov, G.; Cotton, T. M. *Anal. Chem.* **1998**, *70*, 3898–3905.
(13) Stromberg, N.; Hulth, S. *Anal. Chim. Acta* **2001**, *443*, 215–225.
(14) Stromberg, N.; Hulth, S. *Sens. Actuators, B* **2003**, *90*, 308–318.
(15) Werner, T. C.; Cummings, J. G.; Seitz, W. R. *Anal. Chem.* **1989**, *61*, 211–215.
(16) Krause, C.; Werner, T.; Huber, C.; Wolfbels, O. S.; Leiner, M. J. P. *Anal. Chem.* **1999**, *71*, 1544–1548.
(17) Lu, H. Y.; Rutan, S. C. *Anal. Chem.* **1996**, *68*, 1381–1386.

10.1021/ac8025866 CCC: $40.75 © 2009 American Chemical Society
Published on Web 04/30/2009

EXPERIMENTAL SECTION

Materials. GNPs came from Sigma-Aldrich, and were of 10 nm particle size (~0.01% $HAuCl_4$, ~0.75 A_{520} units/mL, 8.5−12.0 nm mean particle size (monodisperse)). 1-Dodecanethiol, nonactin, 2-(dodecyloxy)benzonitrile, tetrahydrofurane (THF), dimethyl sulfoxide (DMSO), merocyanine 540 (MC540), ammonium chloride, sodium chloride, and ethanol were all reagent grade and purchased from Sigma-Aldrich. The HN80 Hypan hydrogel came from Hymedix Inc., and Milli-Q water (electric reistivity >18 MΩ cm^{-1}) was obtained from a Millipore water purification system. Stock solutions of dodecanethiol (10 mM in ethanol), MC540 (7 μM in Milli-Q water), ammonium chloride (2 mM in Milli-Q) and sodium chloride (2 mM in Milli-Q) were prepared.

Apparatus. Fluorescence experiments were performed on a Fluoromax 3 instrument from Jobin Yvon (Horiba group). Microscopy images were acquired with a Leica DMI6000B microscope, and filter cube Y3 was used for the fluorescence image.

Preparation of Lipophilized GNPs. The alkanethiol monolayer was prepared in a manner related to previously published methods on flat gold surfaces by, for example, Bain et al.[18] In brief, dodecanethiol (250 μL, 10 mM in ethanol) was mixed with 500 μL of the GNP solution and allowed to form monolayers for 48 h during intense shaking (1800 min^{-1}). To eliminate GNPs with a diminutive thiol monolayer, 75 μL of ether (2-(dodecyloxy)benzonitrile) was added to the mixture to extract GNPs hydrophobic enough to prefer the fatty ether. The solution was vigorously shaken (2400 min^{-1}) for 10 min, after which it was allowed to phase-separate for 48 h. A three-phase system appeared, and the clear, upper, ether phase was removed carefully to be used in the sensors.

Preparation of Sensing Membranes. The sensing membranes were prepared in a manner similar to Stromberg and Hulth.[14] HN80 hydrogel (69 mg) and the ionophore nonactin (2.8 mg) were weighted in a 5 mL glass vial, DMSO (2.1 mL) was added, and the vial was sealed. The sensor blend was stirred and heated to 150 °C for ~30 min. THF (0.9 mL) was slowly added during continuing stirring (but not heating). Ether with and without GNPs was added in various amounts to produce membranes with different quantities of GNPs. To the blank sensor was added 6 μL of ether without GNPs, and to sensor 1 was added 2 μL of ether with and 4 μL without GNPs. To sensors 2 and 3 was added only ether with nanoparticles, 6 and 30 μL, respectively. The sensor cocktails (0.5 mL per sensor) were spread onto a transparency film (Corporate Express, code 608 83 29) and allowed to form emulsions overnight in a semiclosed container with an air humidity of ~60%. Access solvents were rinsed away with Milli-Q water. The sensors were stained by immersing in a 7 μM solution of MC540 for 6 h. Before fluorescence measurements, the sensing membranes were immersed in NaCl (2 mM) solution. Note that the only difference between the blank sensor and the other sensors is the addition of the GNPs.

Fluorescence Experiments. Measurements were performed in a standard plastic cuvette for fluorescence, and the sensing membranes were mounted at a 30° angle of incidence from the excitation source. The equilibrium time for both increases and decreases in ammonium concentration was 15 min. Excitation and emission spectra were collected with slit widths corresponding to 2 nm bandpass, integration times were set to 0.25 s, and steps were 1 nm. Solutions for the spectra were obtained by mixing appropriate amounts of ammonium and sodium chloride stock solutions (for a constant ionic strength of 2 mM). For the low concentration, calibration slit widths corresponding to 2 nm (excitation side) and 5 nm (emission) bandpasses were used, and integration times were set to 1 s to fairly optimize the signal to calculate limits of detection and quantification. Seven replicate measurements on the same sensing membrane were made on each calibration level. No precautions were taken to prevent ammonia from air from equilibrating with the test solutions. Hence, the air equilibrated amount of ammonium is considered to be background, which in reality makes it more difficult to achieve high-quality detection limits.

RESULTS AND DISCUSSION

General Properties. The novel concept of this sensing scheme is that the analyte response involves a movement of the fluorophore toward lipophilized GNPs in an organic phase (Figure 1). Properly arranged, the system benefits from surface plasmon enhancement as well as increased quenching as the fluorophore moves toward the GNPs. Additionally, constructive scattering effects may also be present in the case of nanoparticle clusters. The system was tested with nonactin, the most commonly used ammonium ionophore. Nonactin is a rather nonselective cation ionophore, although improved ammonium ionophores are, to the best of my knowledge, absent. A 10-fold higher selectivity than nonactin for binding NH_4^+ over K^+ has been shown;[19] however, the poor detection limit (10^{-4} M)[19] for that ionophore implies a low affinity for ammonium (and potassium). Other ion-selective ammonium electrodes (ISEs) have demonstrated LODs in the 10^{-6}−10^{-5} M region, which have been shown for both ISEs with nonactin[20] and for more recently developed ionophores.[19,21] For the coextraction-based ammonium optode, a detection limit of 10^{-6} M has previously been shown,[22,23] as compared with 10^{-9} M demonstrated in this study with the incorporated nanoparticles.

The sensing scheme used in this study is general and can be utilized for any ion that has a neutral ionophore. However, it is much easier to change to another cation because only the ionophore and not the dye and nanoparticles (to match the dye) need replacement. The sensing scheme could potentially gain significantly with a more selective and higher affinity ionophore. Higher affinity would likely improve the detection limit, and better selectivity would decrease interferences from other solutes and therefore enhance the probability of sustaining low detection limits in natural samples.

The high-GNP sensor (sensor 3) was used for 10 days with more than 50 solution changes without needing to replenish dye.

(18) Bain, C. D.; Troughton, E. B.; Tao, Y. T.; Evall, J.; Whitesides, G. M.; Nuzzo, R. G. *J. Am. Chem. Soc.* **1989**, *111*, 321–335.

(19) Chin, J.; Oh, J.; Jon, S. Y.; Park, S. H.; Walsdorff, C.; Stranix, B.; Ghoussoub, A.; Lee, S. J.; Chung, H. J.; Park, S. M.; Kim, K. *J. Am. Chem. Soc.* **2002**, *124*, 5374–5379.

(20) Berrocal, M. J.; Badr, I. H. A.; Gao, D. O.; Bachas, L. G. *Anal. Chem.* **2001**, *73*, 5328–5333.

(21) Suzuki, K.; Siswanta, D.; Otsuka, T.; Amano, T.; Ikeda, T.; Hisamoto, H.; Yoshihara, R.; Ohba, S. *Anal. Chem.* **2000**, *72*, 2200–2205.

(22) Stromberg, N.; Hulth, S. *Anal. Chim. Acta* **2005**, *550*, 61–68.

(23) Stromberg, N.; Hulth, S. *Sens. Actuators, B* **2006**, *115*, 263–269.

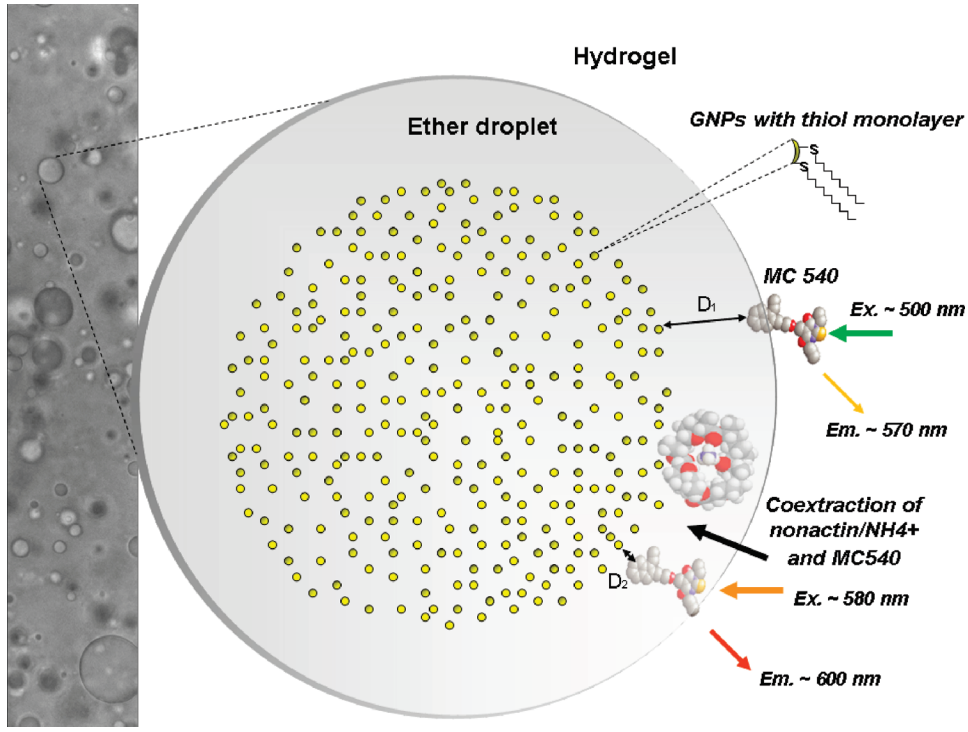

Figure 1. Principal sensor configuration and ratiometric fluorescence detection. Average D_1 distance in the ~10−100 nm range is warranted to provide SPCE on the outside as well as increased LSWs on the inside for the 500 nm excitation (Ex580:Em600 nm is expectantly plasmon-decoupled). The figure is not to scale, and the particle "depleted" zone is in the length scale of a few nanometers up to possibly hundreds of nanometers, depending on particle concentration and surface charges. Droplet size range, ~1−4 μm (BF image 1260×).

Response times of less than 4 min have been shown for the ammonium sensor without GNPs (forward and reverse).[13] A change in response time may not be expected with the nanoparticles added; however, the GNPs or excess thiol could potentially interact with the coextraction procedure, so there is a need to investigate this.

Sensing Mechanism. Figure 1 illustrates the sensor configuration and fluorescent sensing properties. The particle size was chosen to involve SPCE and LSWs for the weaker fluorescence of MC 540 (~Ex500:Em570 nm) and provide insignificant plasmon and quenching effects on the ~Ex580:Em600 nm fluorescence. This is due to a large fluorescence shift as the dye is coextracted (~80 nm excitation red shift). The proximity to the GNP plasmon peak is thereby reduced (Figure 2), and the fluorophores plasmon-coupled emission are decoupled. In the absence of analyte, the GNPs obtain a distinct, on statistical average, closest distance (D_1 in Figure 1) to the dye molecules residing on the surface of the fatty emulsion droplets. As the probe gets coextracted with ammonium, a new closest statistical nanoparticle−fluorophore distance (D_2 in Figure 1) is acquired. Average ΔD distance is therefore statistically ammonium-concentration-dependent. If D_1 is of a certain close but not too close distance, the surface plasmon enhancement is expected for the ~Ex500:Em570 nm fluorescence (D_1 ~ 10−100 nm is valid for planar surfaces).[9] With fluorophore−metal distances below ~100 nm, LSWs rapidly increase,[3,9,11] and as the ammonium levels and the number of coextracted MC540 increases, SPCE rapidly turns into LSWs. Therefore, the original inherent fluorescence sensing schemes decrease for ~Ex500:Em570 nm as the ammonium concentration rises and is reinforced by the GNPs. Another important feature of this new sensing scheme is that the zero level

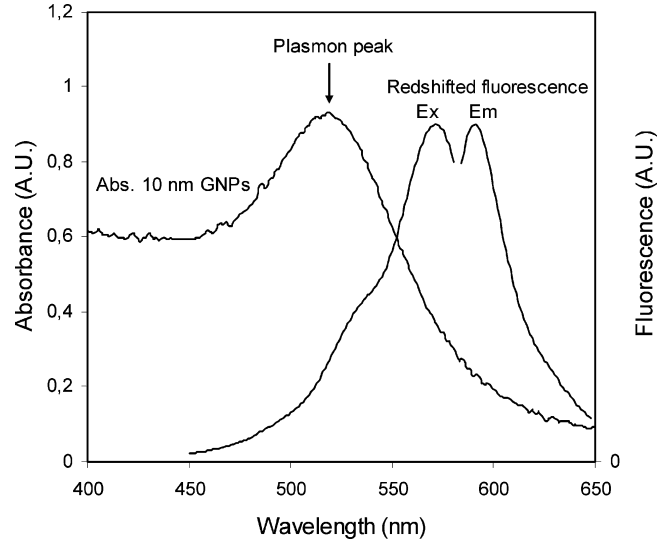

Figure 2. Absorbance spectrum for 10 nm gold nanoparticles and the red-shifted excitation and emission spectra for MC 540 in the ammonium sensor.

noise is severely decreased due to plasmon enhancement of the weaker fluorescence in the absence of the analyte. Thereby, the limit of detection is improved by both increased sensitivity and reduced noise. The actual D_1 and D_2 distances are at present not known and will be the subject of rigorous optimizations to provide even better detection limits. The optimal D_1 distance is certainly less than 100 nm for 10 nm GNPs because the SP field is not likely to reach many times the particle diameter.

Lipophilization of Nanoparticles. The lipophilization of the GNPs and incorporation into the emulsion droplets were con-

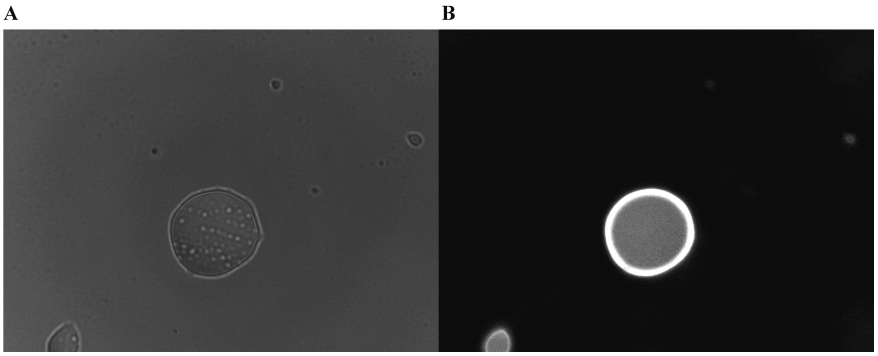

Figure 3. (A) Bright field image of an ether droplet ($d \approx 7$ μm) in aqueous solution as it fills up with lipophilized gold nanoparticles (clusters of nanoparticles are seen as gray spots on the outside of the bubble and as bright spots inside). (B) Fluorescence image of image A; note the low fluorescence contribution from bulk water.

firmed by adding a few microliters of the functionalized GNPs to a droplet of water with 2-(dodecyloxy)benzonitrile (the ether) in it. By focusing a microscope (1260×) on a single emulsion droplet immediately after the addition of lipophilized GNPs, clusters of particles were observed entering the droplet (Figure 3A). In addition, when adding MC540 to the solution, an intense fluorescence emerged from the droplet (Figure 3B), confirming that the addition of the GNPs and thiol had no significant negative effect on the dyes' strong affinity to the emulsion drops.

Sensor Characteristics. The sensors' maximum relative responses to ammonium are quite a bit off λ_{max} (Figure 4), which are not surprising because vibrations and rotations are affected by the change of environment, and it is not sure or even likely that the vibrations and rotations associated with λ_{max} are affected the most. However, initially, the ratiometric pair Ex578:Em588/Ex511:Em566 was utilized for the fluorescence measurements, which is close to previously used wavelengths for the sensor without GNPs.[24] Calibration curves for this ratiometric pair showed a conclusive trend that the response increased with the amount of GNPs (Figure 5A). For example, for a 0−200 μM ammonium concentration increase, the relative signal enhancement between the blank (no GNPs) and the high-GNP (sensor 3) sensors was 490%.

During this study, another ratiometric pair was recognized. In Figure 4, emission spectra at excitation 496 nm (Figure 4A) and 583 nm (Figure 4B) are shown for three different ammonium concentrations for the blank, sensor 1, and sensor 3 (zero, low, and high GNP load). Absolute signals for both wavelengths are enhanced with increased GNPs. The most pronounced difference in relative ratiometric signal is seen in the 0−200 μM range, with an increase of 282% for sensor 3, as compared to 125% for sensor 1 and only a 63% increase for the blank sensor. A bit unexpected, the Ex583:Em600 (the fluorescence that was predicted to not be affected by SPs and LSWs) is primarily enhanced. The signal increases were 148%, 73%, and 40% for sensor 3, sensor 1, and the blank, respectively. This is probably a positive effect from build-up of small clusters of GNPs, which are likely to scatter but not quench light at ~580−600 nm, thereby amplifying the incident field of radiation for the red-shifted fluorescence.[3,12] Therefore, as the fluorophore moves into the ether, the GNP clusters gets closer and, probability for constructive scattering, can be expected to increase quadratically with fluorophore−cluster distance. The

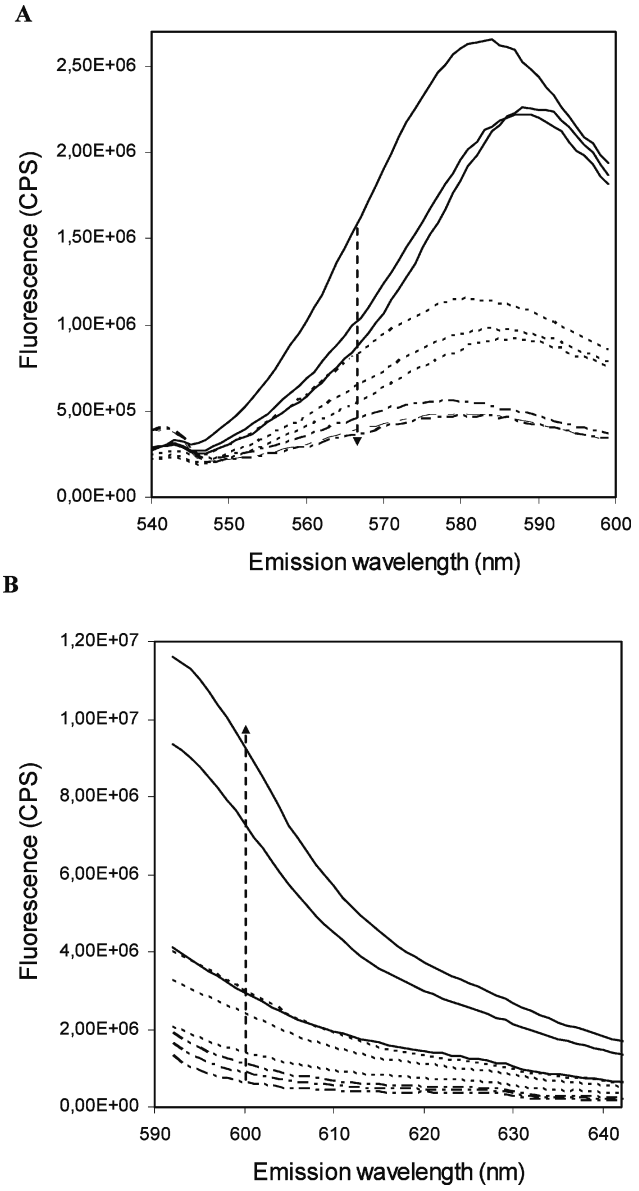

Figure 4. Emission spectra for 0−200−500 μM concentrations (arrows indicate increasing ammonium concentration at maximum relative response): (A) excitation at 496 nm and (B) Excitation at 583 nm. The blank (zero GNPs) sensor showed the lowest signal (dash dot), the sensor with low amount of GNPs was intermediate (sensor 1, dotted lines), and the high-amount sensor demonstrated a superior signal (solid lines).

(24) Stromberg, N. *Environ. Sci. Technol.* **2008**, *42*, 1630–1637.

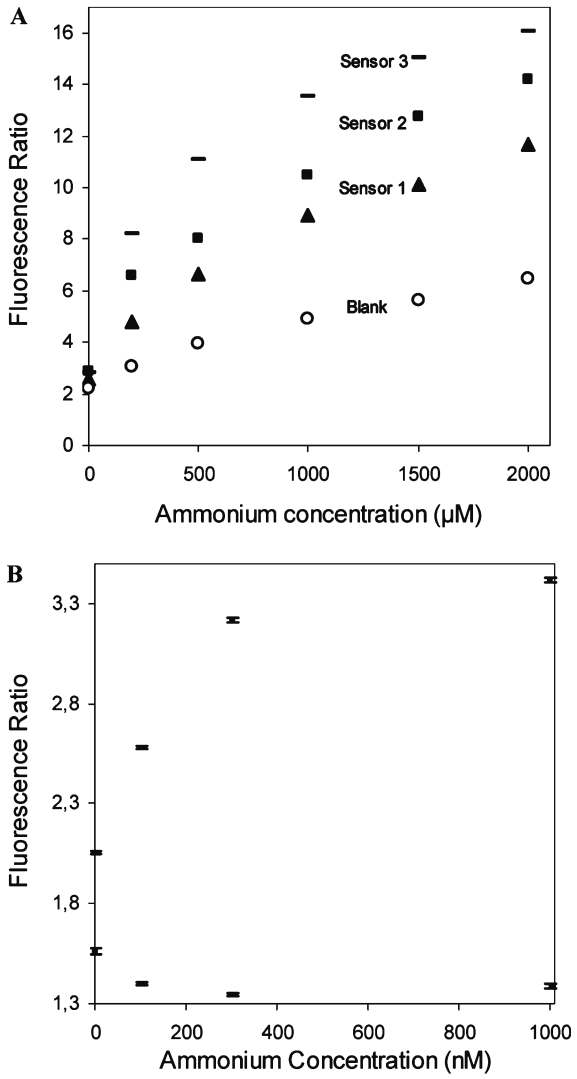

Figure 5. (A) Ratiometric (Ex578:Em588/Ex511:Em566) calibration curves for the three GNP loaded sensors (▲, low; □, intermediate; and −, high amount GNPs) and the blank sensor (○, no GNPs). The fluorescence ratiometric pair was used.(B) Ratiometric (Ex583:Em601/Ex496:Em567) calibration curve for the nanomolar range, with error bars that display six standard deviations. The blank sensor calibration is included (bottom).

scattering enhancement is also exemplified in Figure 4A, where the emission (for Ex 496 nm) actually increases for the longer wavelengths (>585 nm) as the ammonium concentration increases from 200 to 500 μM (for the sensor with high GNP load).

A nanomolar calibration was performed on the best-performing sensor (sensor 3 with high GNP load) and the blank sensor (no GNPs). Ratiometric pair Ex583:Em601/Ex496:Em567 was chosen since the best response in 0−200 μM appeared there. Figure 5B shows the nanomolar calibration, with errorbars that displays ±3 standard deviations (i.e., 6 × S.D.). Limit of detection was calculated to 1.7 nM, from the slope between 0 and 100 nM concentration and the standard deviation of the zero level (i.e., standard approximation $3 \times SD_{zero}$/slope), and limit of quantification was accordingly approximated to 5.7 nM ($10 \times SD_{zero}$/slope). The blank sensor showed a slight reverse response initially, which may be due to photobleaching (Figure 5B). In Table 1, relative responses for the different concentration intervals in the nanomolar calibration are shown, and these show that the dominant signal change can be derived from the Ex496:Em567 fluorescence that normally demonstrates a much weaker response. This strongly suggests that surface plasmon dynamics is, in fact, present in the system, and the transition from fluorescence enhancement to lossy surface waves is likely (for the Ex496:Em567 signal and not the red-shifted fluorescence). However, the optimal conditions for this sensor are likely still to be revealed, which implies that the analytical performance can be far from the true limits. Important parameters to be tested and optimized are amount of GNPs, size of GNPs and thiol carbon chain length.

Table 1. Relative Responses for the Nanomolar Calibration

concn interval (nM)	$F1_{ex:em}$ 496:567 (%)	$F2_{ex:em}$ 583:601 (%)	F2/F1 (%)
0−100	−16.4	4.8	25.4
100−300	−17.3	3.2	24.8
300−1000	−4.3	1.7	6.2
(F_{max}/F_{min})	151	110	166

CONCLUSIONS

Gold nanoparticles were lipophilized with dodecanethiol and incorporated in the ether phase of a coextraction-based ammonium sensor. This new sensor configuration provided reduced noise as well as increased fluorescence ratiometric signals. Surface plasmon enhancement, lossy surface wave quenching, and likely scattering contributed to the signal improvement. Limit of detection was approximately 3 orders of magnitude better than the previous sensing membrane without the nanoparticles. The sensing scheme is general and can be utilized for many other ions.

ACKNOWLEDGMENT

Financial support was obtained from the Swedish Research Council (VR); the Foundation for Strategic Environmental Research (MISTRA); the Swedish Research Council for Environment, Agricultural Sciences and Spatial Planning (FORMAS); and the Swedish Marine Research Centre (GMF). S. Hulth and N. Strömberg provided comments that improved the manuscript.

Received for review December 8, 2008. Accepted April 13, 2009.

AC8025866